

The Pennsylvania State University
The Graduate School
College of Earth and Mineral Sciences

**DEVELOPMENT OF A KNOWLEDGE BASE OF Ti-ALLOYS
FROM FIRST-PRINCIPLES AND COMPUTATIONAL
THERMODYNAMICS**

A Dissertation in
Materials Science and Engineering
by
Cassie Marker

© 2017 Cassie Marker

Submitted in Partial Fulfillment
of the Requirements
for the Degree of

Doctor of Philosophy

August 2017

The dissertation of Cassie Marker was reviewed and approved* by the following:

Zi-Kui Liu

Professor of Materials Science and Engineering

Thesis Advisor, Chair of Committee

Allison Beese

Assistant Professor of Materials Science and Engineering

Kristen Fichthorn

Merrell Fenskey Professor of Chemical Engineering and Professor of Physics

Michael Manley

Senior Researcher, Oak Ridge National Laboratory, Materials Science & Technology Division

Special Member

Susan Sinnott

Department Head and Professor of Materials Science and Engineering

*Signatures are on file in the Graduate School.

Abstract

An aging population with an active lifestyle requires the development of better load-bearing implants, which have high levels of biocompatibility and a low elastic modulus. Titanium alloys, in the body centered cubic phase, are great implant candidates, due to their mechanical properties and biocompatibility. The present work aims at investigating the thermodynamic and elastic properties of bcc Ti-alloys, using the integrated first-principles based on Density Functional Theory (DFT) and the CALculation of PHase Diagrams (CALPHAD) method. The use of integrated first-principles calculations based on DFT and CALPHAD modeling has greatly reduced the need for trial and error metallurgy, which is ineffective and costly. The phase stability of Ti-alloys has been shown to greatly affect their elastic properties. Traditionally, CALPHAD modeling has been used to predict the equilibrium phase formation, but in the case of Ti-alloys, predicting the formation of two metastable phases ω and α'' is of great importance as these phases also drastically effect the elastic properties. To build a knowledge base of Ti-alloys, for biomedical load-bearing implants, the Ti-Mo-Nb-Sn-Ta-Zr system were studied because of the biocompatibility and the bcc stabilizing effects of some of the elements.

With the focus on bcc Ti-rich alloys, a database of thermodynamic descriptions of each phase for the pure elements, binary and Ti-rich ternary alloys was developed in the present work. Previous thermodynamic descriptions for the pure elements were adopted from the widely used SGTE database for global compatibility. The previous binary and ternary models from the literature were evaluated for accuracy and new thermodynamic descriptions were developed when necessary. The models were evaluated using available experimental data, as well as the enthalpy of formation of the bcc phase obtained from first-principles calculations based on DFT. The thermodynamic descriptions were combined into a database ensuring that the sublattice models are compatible with each other.

For subsystems, such as the Sn-Ta system, where no thermodynamic description had been evaluated and minimal experimental data was available, first-principles calculations based on DFT was used. The Sn-Ta system has two intermetallic phases, TaSn_2 and Ta_3Sn , with three solution phases: bcc, body centered tetragonal (bct) and diamond. First-principles calculations were completed on the intermetallic and solution phases. Special quasirandom structures (SQS) were used to obtain information about the solution phases across the entire composition range. The Debye-Grüneisen approach, as well as the quasiharmonic phonon method, were used to obtain the finite-temperature data. Results from first-principles calculations and experiments were used to complete the thermodynamic description. The resulting phase diagram reproduced the first-principles calculations and experimental data accurately.

In order to determine the effect of alloying on the elastic properties, first-principles calculations based on DFT were systematically done on the pure elements, five Ti-X binary systems and Ti-X-Y ternary systems ($X \neq Y = \text{Mo, Nb, Sn, Ta, Zr}$) in the bcc phase. The first-principles calculations predicted the single crystal elastic stiffness constants c_{ij} 's. Correspondingly, the polycrystalline aggregate properties were also estimated from the c_{ij} 's, including bulk modulus B , shear modulus G and Young's modulus E . The calculated results showed good agreement with experimental results. The CALPHAD method was then adapted to assist in the database development of the elastic properties as a function of composition. On average, the database predicted the elastic properties of higher order Ti-alloys within 5 GPa of the experimental results.

Finally, the formation of the metastable phases, ω and α'' was studied in the Ti-Ta and Ti-Nb systems. The formation energy of these phases, calculated from first-principles at 0 °K, shows that these phases must be stabilized by entropy. A new theoretic framework was introduced that allows the prediction of the increase in entropy due to the competition between the metastable and stable phase. Using this approach, the phase fraction of the phases were predicted for the Ti-Nb system. The predicted phase fractions were used to calculate the mixed force constants to obtain the phonon density of states. Results from inelastic neutron scattering experiments were compared to the predicted phase fractions and phonon density of states for accuracy. Then the predicted phase fractions were used to calculate the elastic properties using the rule of mixtures. The predicted elastic properties were compared with available experimental data.

This thesis provides a knowledge base of the thermodynamic and elastic properties of Ti-alloys from computational thermodynamics. The databases created will impact research activities on Ti-alloys and specifically efforts focused on Ti-alloys for biomedical applications.

Table of Contents

List of Figures	x
List of Tables	xix
Acknowledgments	xxiii
Chapter 1	
Introduction	1
1.1 Motivation	1
1.2 Overview	2
1.2.1 Equilibrium Phases	2
1.2.2 Metastable Phases	3
Chapter 2	
Methodology	10
2.1 First-Principles Calculations	10
2.1.1 Density Functional Theory at 0 °K	12
2.1.2 Finite-temperature thermodynamics	13
2.1.3 Elastic stiffness calculations	15
2.1.4 Special quasirandom structures (SQS)	17
2.1.5 High-throughput partition function	17
2.1.6 First-principles calculation error	18
2.2 CALPHAD method	19
2.2.1 Solution phases	19
2.2.2 Stoichiometric compounds	21
2.2.3 Elastic Properties	21
2.3 Experimental	22
2.3.1 Ti-Nb sample preparation	22
2.3.2 Neutron Scattering	22
2.3.2.1 ARCS	22

2.3.2.2 Data Analysis	23
---------------------------------	----

Chapter 3

Ti-Mo-Nb-Sn-Ta-Zr

Thermodynamic Database	25
3.1 Introduction	25
3.2 Computational details	26
3.2.1 Sn binaries and ternaries	27
3.3 Pure element calculation results	27
3.4 Enthalpy of formation of bcc phase from first-principles	28
3.5 Thermodynamic modeling of the ten binary systems	29
3.5.1 Mo-Nb, Mo-Ta, Nb-Ta	29
3.5.2 Mo-Zr, Nb-Zr and Ta-Zr	30
3.5.3 Ti-Mo	31
3.5.4 Ti-Nb	32
3.5.5 Ti-Ta	32
3.5.6 Ti-Zr	33
3.6 Thermodynamic modeling of six Ti-containing ternary systems	34
3.6.1 Ti-Mo-Nb	34
3.6.2 Ti-Mo-Ta	35
3.6.3 Ti-Mo-Zr	35
3.6.4 Ti-Nb-Ta	36
3.6.5 Ti-Nb-Zr	37
3.6.6 Ti-Ta-Zr	37
3.7 Conclusion	38

Chapter 4

First-principles aided thermodynamic modeling of the Sn-Ta system

	64
4.1 Introduction	64
4.2 Literature Review	65
4.3 Modeling and Calculations	66
4.3.1 First-principles details	66
4.3.2 CALPHAD	67
4.4 Results and discussion	67
4.4.1 First-principles	67
4.4.2 CALPHAD	69
4.5 Conclusion	71

Chapter 5	
Effects of alloying elements on the elastic properties of bcc Ti-X alloys	87
5.1 Introduction	87
5.2 Modeling and Calculations	88
5.2.1 Calculation details	88
5.2.2 Modeling details	88
5.3 Results and discussion	89
5.3.1 Evaluation of calculation settings	89
5.3.2 1.1 Calculations of elastic coefficients in Ti-X binary systems	89
5.3.3 Extrapolation to ternary and higher ordered systems	93
5.4 Conclusion	94
Chapter 6	
Effects of alloying elements on the elastic properties of bcc ternary and higher ordered Ti-alloys	113
6.1 Introduction	113
6.2 Modeling and Calculations	114
6.2.1 Calculation details	114
6.2.2 Modeling details	114
6.3 Results and discussion	115
6.3.1 Elastic calculation results	115
6.3.2 Extrapolation to higher ordered systems	121
6.4 Conclusion	122
Chapter 7	
Metastable phase study in the Ti-Ta and Ti-Nb systems	146
7.1 Introduction	146
7.2 Modeling and Calculations	147
7.2.1 Computational details	147
7.2.2 Modeling details	147
7.3 Results and discussion	148
7.3.1 First-principles calculations at 0 K	148
7.3.2 Elastic properties	148
7.3.3 Neutron scattering results	151
7.3.3.1 Phonon density of states at 300 K	151
7.3.3.2 Diffraction patterns at 300 K	152
7.3.4 Partition function approach results	153
7.4 Conclusion	153

Chapter 8	
Conclusions and Future Work	177
8.1 Conclusions	177
8.2 Future Work	181
Appendix A	
Ti-Mo-Nb-Ta-Zr Database	182
Appendix B	
Sn-Ta Database	199
Appendix C	
Calculation and Fitting Details	207
C.1 Calculation Details for Chapter 3, 5, and 6	207
C.2 Fitting Code for Chapter 5 and 6	211
Appendix D	
Ti Elastic Database	212
Appendix E	
Pycalphad script	219
Appendix F	
Ti-Nb Experimental Elastic Data	229
Bibliography	232

List of Figures

1.1	Comparison of first-principles calculations [1, 2] and experimental measurements of the Young's modulus of Ti-Ta alloys [3–5]. From 0.10 to 0.35 x(Ta) the calculations and experimentally determined E do not match up due to the formation of two metastable phases ω and α''	8
1.2	Comparison of the present first-principles calculations and experimental measurements of the Young's modulus of Ti-Nb alloys [6–10]. From 0.10 to 0.30 x(Nb) the calculations and experimentally determined E do not match up due to the formation of two metastable phases ω and α''	9
3.1	Previously modeled thermodynamic descriptions of the Mo-Nb (a) [11], Mo-Ta (b) [11] and Nb-Ta (c) [11] binary systems in comparison with available liquidus and solidus phase boundary experimental data to ensure accuracy as detailed in [11].	48
3.2	Previously modeled thermodynamic descriptions of the Mo-Zr [12] system is plotted with phase boundary, reaction, single phase and two phase experimental data. The previously modeled Nb-Zr [13, 14] system is plotted with solidus, hcp solvus and bcc solvus experimental data. The previously modeled Ta-Zr [15] system is plotted with single-phase, two-phase, phase boundary and solidus experimental data (detailed in the mentioned references).	49
3.3	Previously modeled thermodynamic description of the Ti-Mo system versus available phase boundary and solidus experimental data to ensure accuracy [16, 17] (a), and enthalpy of formation of the bcc phase predicted by the previous thermodynamic modeling (solid line) at 300 °K versus the present first-principles calculations (circles) at 0 °K and compared with the enthalpy of formation of the bcc phase obtained from experiments [18] (b).	50

3.4 Previously modeled thermodynamic description of the Ti-Nb system versus available phase boundary and solidus experimental data to ensure accuracy [19–21][20,48] (a), and enthalpy of formation of the bcc phase predicted by the previous thermodynamic modeling (solid line) at 300 °K versus the present first-principles calculations (circles) at 0 °K compared with the enthalpy of formation of the bcc phase obtained from experiments [18] (b).	51
3.5 Previously modeled thermodynamic description of the Ti-Ta system versus available phase boundary and solidus experimental data to ensure accuracy [16, 22] (a), and enthalpy of formation of the bcc phase predicted by the previous thermodynamic modeling (solid line) at 300 °K versus the present first-principles calculations (circles) at 0 °K (b).	52
3.6 Previously modeled thermodynamic description of the Ti-Zr system versus available phase boundary and solidus experimental data to ensure accuracy [21] (a), and enthalpy of formation of the bcc phase predicted by the previous thermodynamic modeling (solid line) at 300 °K versus the present first-principles calculations (circles) at 0 °K (b).	53
3.7 Binary interpolation of the isothermal section of the Ti-Mo-Nb system plotted at 873 °K (a), and enthalpy of formation of the bcc phase predicted by the binary interpolation of the thermodynamic modeling (solid line) at 300 °K versus the present first-principles calculations (circles) at 0 °K (b).	54
3.8 Binary interpolation of the isothermal section of the Ti-Mo-Ta system plotted at 873 °K (a), and enthalpy of formation of the bcc phase predicted by the previous thermodynamic modeling (solid line) at 300 °K and the ternary assessed thermodynamic modeling (red dotted line) versus the present first-principles calculations (circles) at 0 °K (b).	55
3.9 Ternary assessed isothermal section of the Ti-Mo-Ta system plotted at 873 °K (a), and zoomed in ternary assessed isothermal section at 873 °K with the phase boundary and two-phase region experimental data [23] (b) to ensure accuracy of the ternary assessment.	56
3.10 Binary interpolation of the isothermal section of the Ti-Mo-Zr system plotted at 1273 °K compared with experimental phase boundary data [24,25] (a), and enthalpy of formation of the bcc phase predicted by the previous thermodynamic modeling (solid line) at 300 °K versus the present first-principles calculations (circles) at 0 °K (b).	57

3.11	Binary interpolation of the isothermal section of the Ti-Nb-Ta system plotted at 673 °K compared with experimental phase boundary data [26] (a), and binary interpolation of the isothermal section of the Ti-Nb-Ta system plotted at 823 °K compared with experimental phase boundary data [26] (b).	58
3.12	Enthalpy of formation of the bcc phase predicted by the previous thermodynamic modeling (solid line) at 300 °K and the ternary assessed thermodynamic modeling (red dotted line) versus the present first-principles calculations (circles) at 0 °K.	59
3.13	Ternary assessed isothermal section of the Ti-Nb-Ta system plotted at 673 °K compared with experimental phase boundary data [26] to ensure accuracy of the ternary assessment (a), and ternary assessed isothermal section at 823 °K compared with experimental phase boundary data [26] to ensure accuracy of the ternary assessment (b).	60
3.14	Binary interpolation of the isothermal section of the Ti-Nb-Zr system plotted at 843 °K compared with experimental phase boundary and two-phase region data [27] (a), and enthalpy of formation of the bcc phase predicted by the previous thermodynamic modeling (solid line) at 300 °K versus the present first-principles calculations (circles) at 0 °K (b).	61
3.15	Binary interpolation of the isothermal section of the Ti-Ta-Zr system plotted at 1273 °K compared with experimental phase boundary data [28, 29] (a), and binary interpolation of the isothermal section of the Ti-Ta-Zr system plotted at 1773 °K compared with compared with experimental single phase and two-phase region data [28, 29] (b).	62
3.16	Enthalpy of formation of the bcc phase predicted by the previous thermodynamic modeling (solid line) at 300 °K versus the present first-principles calculations (circles) at 0 °K.	63
4.1	Calculated phonon dispersion curve of bcc-Ta, compared with neutron diffraction experiments (\circ) [30] along with the phonon DOS.	76
4.2	Calculated phonon dispersion curve of bct-Sn on the left and phonon DOS on the right. The open squares (\square) are the LO and TO modes from Raman [31] and the filled squares the theoretical prediction of the LO and TO modes at the M point [31].	77
4.3	Calculated phonon dispersion curve for $TaSn_2$ at 0 °K and the phonon DOS.	78
4.4	Calculated phonon dispersion curve of Ta_3Sn at 0 °K on the left and the phonon DOS on the right.	79

4.5	Comparison of the enthalpy and entropy of bcc-Ta from the Debye model (solid line) and the quasiharmonic phonon calculations (red dotted line) to the SGTE data (blue dashed line) [32].	80
4.6	Comparison of the Gibbs energy of bct-Sn from the Debye model (solid line) and the quasiharmonic phonon calculations (red dotted line) to the SGTE data (blue dashed line) [32].	81
4.7	Heat capacity, enthalpy and entropy of TaSn_2 using the Debye model (solid line) and the quasiharmonic phonon calculation (red dotted line) from first-principles calculations, compared with those from the current CALPHAD modeling (blue dashed line).	82
4.8	Heat capacity, enthalpy and entropy of Ta_3Sn using the Debye model (solid line) and the quasiharmonic phonon calculation (red dotted line) compared with those from the current CALPHAD modeling (blue dashed line).	83
4.9	Enthalpy of formation of the bcc phase of the Sn-Ta system as a function of composition at 298 °K and ambient pressure from the current CALPHAD modeling (solid line) and from the first-principles calculations (dots), showing asymmetric behavior. This was compared with data of the Nb-Sn system from Toffolon et al. [33] (dashed red line) which was modeled using experimental data, showing similar asymmetric behavior.	84
4.10	Calculated Sn-Ta phase diagram using the present thermodynamic description.	85
4.11	Enthalpy of mixing of the liquid phase as a function of composition at 298 °K and ambient pressure in the Sn-Ta system.	86
5.1	Elastic stiffness constants of the bcc Ti-Ta binary system calculated with the GGA and PBE exchange correction functions, respectively.	102
5.2	Elastic stiffness constants for the bcc Ti-Mo binary system calculated with strains, ± 0.01 , ± 0.03 and ± 0.07 , respectively, showing comparable results.	103
5.3	Young's modulus E of the Ti-X binary systems. The present calculations are plotted as the filled circles with the error bars. The dotted purple line is the Voigt upper Young's modulus bound, the gold dot dashed line is the lower Reuss Young's modulus bound and the black line is the Hill Young's modulus average. The experimental values [1–5, 7, 8, 34–36] are also included for comparison.	104
5.4	Young's modulus calculated from the model parameters (see 5.2) and Eq. 2.30 as a function of composition from bcc Ti to bcc X. . .	105

5.5	Calculated \bar{C}_{11} values (circles) plotted with their errors as well as the pure element extrapolation (red dashed line) and the present modeling (black dashed line) for five Ti-X binary systems (X = Mo, Nb, Ta, Sn, Zr). Ti-Mo, Ti-Nb, and Ti-Ta alloys are compared with previous calculations from Ikehata et al. [2].	106
5.6	Calculated \bar{C}_{12} values (circles) plotted with their errors as well as the pure element extrapolation (red dashed line) and the present modeling (black dashed line) for five Ti-X binary systems (X = Mo, Nb, Ta, Sn, Zr). Ti-Mo, Ti-Nb, and Ti-Ta alloys are compared with previous calculations from Ikehata et al. [2].	107
5.7	Calculated \bar{C}_{44} values (circles) plotted with their errors as well as the pure element extrapolation (red dashed line) and the present modeling (black dashed line) for five Ti-X binary systems (X = Mo, Nb, Ta, Sn, Zr). Ti-Mo, Ti-Nb, and Ti-Ta alloys are compared with previous calculations from Ikehata et al. [2].	108
5.8	Calculated \bar{C}_{11} - \bar{C}_{12} values (circles) plotted with the present modeling (solid lines) for five Ti-X binary systems (X = Mo, Nb, Ta, Sn, Zr). The \bar{C}_{11} - \bar{C}_{12} shows the stability of the bcc phase. When the \bar{C}_{11} - \bar{C}_{12} value is negative the bcc phase is not stable in the corresponding compositions range.	109
5.9	Bulk modulus B of the Ti-X binary systems. The present calculations are plotted as the filled circles with the error bars. The dotted purple line is the Voigt upper bulk modulus bound, the gold dot dashed line is the lower Reuss bulk modulus bound and the black line is the Hill bulk modulus average.	110
5.10	Shear modulus G of the Ti-X binary systems. The present calculations are plotted as the filled circles with the error bars. The dotted purple line is the Voigt upper shear modulus bound, the gold dot dashed line is the lower Reuss shear modulus bound and the black line is the Hill shear modulus average.	111
5.11	Young's moduli values of multicomponent bcc Ti alloys measured experimentally plotted against the predicted Young's moduli from the pure elements and binary interaction parameters with the black diagonal line showing the exact correlation between the experimental and calculated values. Error bars in the experiments and the bounds from Reuss and Voigt approximations are plotted as vertical and horizontal lines, respectively. The variance in the first calculations from Eq. 2.18-Eq. 2.20 was averaged and plotted as the grey region to show the variance in the first-principles calculations. More information on the alloys is in Table 5.5 [37–39]	112

6.1	Calculated \bar{C}_{11} values (circles) plotted with their errors as well as the interpolation from the binary interaction parameters (red dashed line) and the ternary fitting (black dashed line) for five of the Ti-X-Y binary systems from a 50-50 mixture of the alloying elements X and Y to Ti ($X \neq Y = Mo, Nb, Ta, Sn, Zr$)	130
6.2	Calculated \bar{C}_{11} values (circles) plotted with their errors as well as the interpolation from the binary interaction parameters (red dashed line) and the ternary fitting (black dashed line) for five of the Ti-X-Y binary systems from a 50-50 mixture of the alloying elements X and Y to Ti ($X \neq Y = Mo, Nb, Ta, Sn, Zr$)	131
6.3	Calculated \bar{C}_{12} values (circles) plotted with their errors as well as the interpolation from the binary interaction parameters (red dashed line) and the ternary fitting (black dashed line) for five of the Ti-X-Y binary systems from a 50-50 mixture of the alloying elements X and Y to Ti ($X \neq Y = Mo, Nb, Ta, Sn, Zr$)	132
6.4	Calculated \bar{C}_{12} values (circles) plotted with their errors as well as the interpolation from the binary interaction parameters (red dashed line) and the ternary fitting (black dashed line) for five of the Ti-X-Y binary systems from a 50-50 mixture of the alloying elements X and Y to Ti ($X \neq Y = Mo, Nb, Ta, Sn, Zr$)	133
6.5	Calculated \bar{C}_{44} values (circles) plotted with their errors as well as the interpolation from the binary interaction parameters (red dashed line) and the ternary fitting (black dashed line) for five of the Ti-X-Y binary systems from a 50-50 mixture of the alloying elements X and Y to Ti ($X \neq Y = Mo, Nb, Ta, Sn, Zr$)	134
6.6	Calculated \bar{C}_{44} values (circles) plotted with their errors as well as the interpolation from the binary interaction parameters (red dashed line) and the ternary fitting (black dashed line) for five of the Ti-X-Y binary systems from a 50-50 mixture of the alloying elements X and Y to Ti ($X \neq Y = Mo, Nb, Ta, Sn, Zr$)	135
6.7	Calculated \bar{C}_{11} - \bar{C}_{12} values (circles) plotted with the present modeling (solid lines) for the Ti-X-Y ternary systems ($X \neq Y = Mo, Nb, Ta, Sn, Zr$). The \bar{C}_{11} - \bar{C}_{12} shows the stability of the bcc phase, when the value is negative the bcc phase is not stable in the corresponding composition ranges	136

6.8	<i>E</i> of five of the Ti-X-Y ternary systems are plotted from a 50-50 mixture of the alloying elements to Ti in the bcc phase. The present calculations are plotted as filled circles with the error bars. The red dotted line is the extrapolation for the pure elements and binary interaction parameters only. The dotted purple line is the Voigt upper <i>E</i> bound, the gold dot dashed line is the lower Reuss <i>E</i> bound and the black line is the Hill <i>E</i> average. Experimental values are include for comparison [38–41].	137
6.9	<i>E</i> of five of the Ti-X-Y ternary systems are plotted from a 50-50 mixture of the alloying elements to Ti in the bcc phase. The present calculations are plotted as filled circles with the error bars. The red dotted line is the extrapolation for the pure elements and binary interaction parameters only. The dotted purple line is the Voigt upper <i>E</i> bound, the gold dot dashed line is the lower Reuss <i>E</i> bound and the black line is the Hill <i>E</i> average. Experimental values are include for comparison [38–41].	138
6.10	The Young's modulus is mapped as a function of composition in GPa for the Ti-Mo-Nb, Ti-Mo-Sn, Ti-Mo-Ta, Ti-Mo-Zr and Ti-Nb-Sn alloy systems using pycalphad [42].	139
6.11	The Young's modulus is mapped as a function of composition in GPa for the Ti-Mo-Nb, Ti-Mo-Sn, Ti-Mo-Ta, Ti-Mo-Zr and Ti-Nb-Sn alloy systems using pycalphad [42].	140
6.12	<i>B</i> calculations of five of the Ti-X-Y ternary systems ($X \neq Y = Mo, Nb, Ta, Sn, Zr$). The present calculations are plotted as the filled circles with error bars as well as the interpolation from the binary interaction parameters (red dashed line). The dotted purple line is the Voigt upper bulk modulus bound, the gold dashed line is the lower Reuss bulk modulus bound and the black line is the Hill bulk modulus average plotted from a 50-50 mixture of the alloying elements X and Y to Ti.	141
6.13	<i>B</i> calculations of five of the Ti-X-Y ternary systems ($X \neq Y = Mo, Nb, Ta, Sn, Zr$). The present calculations are plotted as the filled circles with error bars as well as the interpolation from the binary interaction parameters (red dashed line). The dotted purple line is the Voigt upper bulk modulus bound, the gold dashed line is the lower Reuss bulk modulus bound and the black line is the Hill bulk modulus average plotted from a 50-50 mixture of the alloying elements X and Y to Ti.	142

6.14	<i>G</i> calculations of five of the Ti-X-Y ternary systems (X ≠ Y = Mo, Nb, Ta, Sn, Zr). The present calculations are plotted as the filled circles with error bars as well as the interpolation from the binary interaction parameters (red dashed line). The dotted purple line is the Voigt upper shear modulus bound, the gold dashed line is the lower Reuss shear modulus bound and the black line is the Hill shear modulus average plotted from a 50-50 mixture of the alloying elements X and Y to Ti.	143
6.15	<i>G</i> calculations of five of the Ti-X-Y ternary systems (X ≠ Y = Mo, Nb, Ta, Sn, Zr). The present calculations are plotted as the filled circles with error bars as well as the interpolation from the binary interaction parameters (red dashed line). The dotted purple line is the Voigt upper shear modulus bound, the gold dashed line is the lower Reuss shear modulus bound and the black line is the Hill shear modulus average plotted from a 50-50 mixture of the alloying elements X and Y to Ti.	144
6.16	<i>E</i> of multicomponent bcc Ti alloys predicted from the database are compared with measured experimental results. Error bars plotted are from the variation in experimentally determined Young's moduli values for the specific multi-component alloy. The grey region refers to the error in the first-principles calculations. More information on the alloys is Table 6.4 [37–39].	145
7.1	Relative energy of the bcc, hcp, ω , α'' phases in the Ti-Nb system are plotted from pure Ti to pure Nb.	160
7.2	Relative energy of the bcc, hcp, ω , α'' phases in the Ti-Ta system are plotted from pure Ti to pure Ta.	161
7.3	Martensitic transformation temperature is plotted versus the Ti-Nb composition.	162
7.4	Calculated c_{11} , c_{12} , c_{13} , c_{22} , and c_{23} values (circles) plotted with the linear combination of the pure elements (red dashed line) and the present modeling (black solid line) for five of the elastic stiffness constants of Ti-Nb in the α'' phase.	163
7.5	Calculated c_{33} , c_{44} , c_{55} , and c_{66} values (circles) plotted with the linear combination of the pure elements (red dashed line) and the present modeling (black solid line) for four of the elastic stiffness constants of Ti-Nb in the α'' phase.	164

7.6	Calculated c_{11} , c_{12} , c_{13} , c_{33} , and c_{44} values (circles) plotted with the linear combination of the pure elements (red dashed line) and the present modeling (black solid line) for the elastic stiffness constants of Ti-Nb in the ω phase.	165
7.7	Calculated c_{11} , c_{12} , c_{13} , c_{33} , and c_{44} values (circles) plotted with the linear combination of the pure elements (red dashed line) and the present modeling (black solid line) for the elastic stiffness constants of Ti-Nb in the hcp phase.	166
7.8	Elastic properties of the bcc, hcp, ω , α'' phases in the Ti-Nb system calculated from first-principles based on DFT are plotted as symbols. The CALPHAD fittings are plotted as the dashed lines. The figure is plotted from pure Ti to pure Nb.	167
7.9	Phonon density of states for the Ti-Nb alloy at 20 at. % Nb. The dashed line represents the slow cooled sample while the solid line represents the quenched sample.	168
7.10	Phonon density of states for the Ti-Nb alloy at 18 at. % Nb. The dashed line represents the slow cooled sample while the solid line represents the quenched sample.	169
7.11	Phonon density of states for the Ti-Nb alloy at 12 at. % Nb. The dashed line represents the slow cooled sample while the solid line represents the quenched sample.	170
7.12	Phonon density of states for the Ti-Nb alloy at 10 at. % Nb. The dashed line represents the slow cooled sample while the solid line represents the quenched sample.	171
7.13	Entropy difference between the Ti-Nb alloys with the same alloy composition as a function of temperature.	172
7.14	Diffraction pattern of the Ti-Nb alloy at 20 at. % Nb. The dashed line represents the slow cooled sample while the solid line represents the quenched sample.	173
7.15	Diffraction pattern of the Ti-Nb alloy at 18 at. % Nb. The dashed line represents the slow cooled sample while the solid line represents the quenched sample.	174
7.16	Diffraction pattern of the Ti-Nb alloy at 12 at. % Nb. The dashed line represents the slow cooled sample while the solid line represents the quenched sample.	175
7.17	Diffraction pattern of the Ti-Nb alloy at 10 at. % Nb. The dashed line represents the slow cooled sample while the solid line represents the quenched sample.	176
C.1	211

List of Tables

1.1	Young's moduli of common implant materials compared with the Young's modulus of bone [43].	7
3.1	Equilibrium properties of volume V_0 , energy E_0 , bulk modulus B and the first derivative of bulk modulus with respect to pressure B' from the first-principles calculations for each pure elements in their SER state. The sv and pv refer to the electrons chosen as valance according to the VASP recommendations. The presently calculated results are also compared with available experimental data.	40
3.2	First-principles results at 0 °K for the enthalpy of formation (H_{Form}) of the bcc phase for different mole fraction (x) of alloying element X in the Ti-X binary systems (X = Mo, Nb, Ta, Zr).	41
3.3	First-principles results at 0 °K for the enthalpy of formation (H_{Form}) of the bcc phase for different mole fraction (x) of Ti in the Ti-X-Y ternary systems (X ≠ Y = Mo, Nb, Ta, Zr).	42
3.4	Modelled binary and ternary thermodynamic parameters for the Ti-Mo-Nb-Ta-Zr system. The thermodynamic description of pure elements is not included. The pure element functions, such as GFCCTI, describe the Gibbs energy (G) of the phase (FCC) for the element (TI) were adopted from the SGTE database [32] are listed in the Supplementary TDB (thermodynamic database) file.	43
3.4	Modelled binary and ternary thermodynamic parameters for the Ti-Mo-Nb-Ta-Zr system. The thermodynamic description of pure elements is not included. The pure element functions, such as GFCCTI, describe the Gibbs energy (G) of the phase (FCC) for the element (TI) were adopted from the SGTE database [32] are listed in the Supplementary TDB (thermodynamic database) file.	44

3.4	Modelled binary and ternary thermodynamic parameters for the Ti-Mo-Nb-Ta-Zr system. The thermodynamic description of pure elements is not included. The pure element functions, such as GFCCTI, describe the Gibbs energy (G) of the phase (FCC) for the element (TI) were adopted from the SGTE database [32] are listed in the Supplementary TDB (thermodynamic database) file.	45
3.4	Modelled binary and ternary thermodynamic parameters for the Ti-Mo-Nb-Ta-Zr system. The thermodynamic description of pure elements is not included. The pure element functions, such as GFCCTI, describe the Gibbs energy (G) of the phase (FCC) for the element (TI) were adopted from the SGTE database [32] are listed in the Supplementary TDB (thermodynamic database) file.	46
3.4	Modelled binary and ternary thermodynamic parameters for the Ti-Mo-Nb-Ta-Zr system. The thermodynamic description of pure elements is not included. The pure element functions, such as GFCCTI, describe the Gibbs energy (G) of the phase (FCC) for the element (TI) were adopted from the SGTE database [32] are listed in the Supplementary TDB (thermodynamic database) file.	47
4.1	Lattice parameters from first-principles calculations compared with experimental values.	72
4.2	Equilibrium volume V_0 , bulk modulus B , and the first derivative of bulk modulus with respect to pressure B' , from fitted equilibrium properties from the EOS at 0 °K compared to experimental work and previous DFT studies.	73
4.3	Elastic stiffness constants and elastic properties predicted using the Hill approach and the scaling factors used in the Debye model, calculated from the Poisson ratio, see Eq. 2.12. To ensure the accuracy of the calculated scaling factor, the bulk modulus (B) calculated from the elastic constants was compared to the B_{EOS} calculated from the EOS fitting Eq. 2.6.	74
4.4	Modeled parameters in SI units in the present work for the phases in the Sn-Ta binary system. These parameters were incorporated with the SGTE data for the pure elements [32].	75
5.1	Calculated pure element elastic stiffness constants and the bulk modulus B (in GPa) by X-C functional of PBE are compared with the previous first-principles calculations (FP) by X-C functional PW91 and experiments (Expt). Sv, pv and d refereeing to the s, p, and d states being treated as valance, respectively.	96

5.2	Evaluated interaction parameters L_0 and L_1 using the R-K polynomial Eq. 2.38 for the elastic stiffness constants for the Ti-X binary systems.	97
5.3	First-principles calculations of the elastic stiffness constants, bulk modulus B , shear modulus G , and Young's modulus E in GPa for different atomic percent compositions of the bcc Ti-X binary systems at 0 °K. As well as experimental data for the Young's modulus obtained at 300 °K by the reference stated.	98
5.3	First-principles calculations of the elastic stiffness constants, bulk modulus B , shear modulus G , and Young's modulus E in GPa for different atomic percent compositions of the bcc Ti-X binary systems at 0 °K. As well as experimental data for the Young's modulus obtained at 300 °K by the reference stated.	99
5.4	Predicted Young's modulus (in GPa) of higher order alloys in the bcc phase compared to experimental values found with both the weight percent and atomic percent listed.	100
5.5	Predicted Young's modulus (in GPa) of higher order alloys in the bcc phase compared to experimental values found with both the weight percent and atomic percent listed.	101
6.1	First-principles calculations of the elastic stiffness constants	124
6.1	First-principles calculations of the elastic stiffness constants	125
6.2	First-principles calculations of the bulk modulus B , shear modulus G , and Young's modulus E in GPa for different atomic percent compositions of the bcc Ti-X-Y ternary systems at 0 °K as well as experimental data obtained for the Young's modulus at 300 °K by the references stated.	126
6.2	First-principles calculations of the bulk modulus B , shear modulus G , and Young's modulus E in GPa for different atomic percent compositions of the bcc Ti-X-Y ternary systems at 0 °K as well as experimental data obtained for the Young's modulus at 300 °K by the references stated.	127
6.3	Evaluated interactions parameters (L_2 , Eq. 2.30) for the elastic stiffness constants of the Ti-containing ternary alloys.	128
6.4	Predicted Young's moduli (E) (in GPa) of higher order alloys using the binary and ternary interaction parameters in the bcc phase compared to the predicted Young's moduli (E_{BIN}) using just the binary interaction parameters and the experimental values found with both the weight percent and atomic percent listed.	129

7.1	Results of the first-principles calculations of the elastic stiffness constants in GPa for different atomic percent compositions in the α'' , bcc, hcp, and ω phases in the Ti-Nb system at 0 °K.	155
7.1	Results of the first-principles calculations of the elastic stiffness constants in GPa for different atomic percent compositions in the α'' , bcc, hcp, and ω phases in the Ti-Nb system at 0 °K.	156
7.2	Evaluated interaction parameters L_0 and L_1 , using Eq. 2.38, for the elastic stiffness constants of the hcp, α'' and ω phases in the Ti-Nb systems.	157
7.3	Phase fractions and experimentally determined E (averaged from the data in appendix F [6,8,8,9]) compared with the predicted E using the rule of mixtures and interaction parameters in Table 7.2 for the Ti-Nb system. The * denotes the estimated phase fractions as opposed to the experimentally determined phase fractions with no *.	158
7.4	Phase fractions determined from the diffraction patterns for the Ti-Nb alloys.	159
C.1	The k-points grids used for each calculation done in chapter 3, 5 and 6.	207
C.1	The k-points grids used for each calculation done in chapter 3, 5 and 6.	208
C.1	The k-points grids used for each calculation done in chapter 3, 5 and 6.	209
C.1	The k-points grids used for each calculation done in chapter 3, 5 and 6.	210
F.1	The experimentally determined E values for the Ti-Nb system reviewed and averaged for chapter 7 are listed here [6–9].	229
F.1	The experimentally determined E values for the Ti-Nb system reviewed and averaged for chapter 7 are listed here [6–9].	230
F.1	The experimentally determined E values for the Ti-Nb system reviewed and averaged for chapter 7 are listed here [6–9].	231

Acknowledgments

The completion of graduate school and this dissertation could not have been possibly without the support from many people that I would like to thank now.

First off I would like to thank my PhD advisor Dr. Zi-Kui Liu. I am so grateful to him for his guidance and support throughout my graduate school career. He opened the doors for many wonderful opportunities and I learned more than I thought was imaginable. On top of that he continued to push me and help me try and learn new things. His constant positive attitude and outlook on life has been inspirational to be me and I will continue to benefit from this for the rest of my life.

I want to thank the Penn State Materials Science and Engineering Department. There have been multiple staff, faculty, and external advisory board members who have helped me, mentored me and opened the door to new opportunities. I would like to specifically thank my committee members Dr. Allison Beese, Dr. Kristen Fichthorn, Dr. Michael Manley and Dr. Susan Sinnott for their time, constructive criticism and advice throughout this journey.

I want to thank Dr. Ji-Cheng Zhao, Dr. Michael Manley, and Dr. Yong Du. Each of you gave me the opportunity to learn new things and expand my PhD experience through collaborations, and allowing me to visit your labs.

I want to express my deepest thanks to my family. I am lucky to have multiple family members who support and love me including my parents, siblings, grandparents, aunts, uncles and cousins. There were many ups and downs in my educational pursuit and you were each there for me in multiple different ways and I am very grateful.

I would also like to thank the members of the Phases Research Lab past and present. It was an honor to get to work with so many wonderful people and to connect with previous members. I learned a lot from each of you and formed many lasting friendships amongst the group. Listing all of the members that positively impacted my life would take up too much space but I wanted to thank the members who served as mentors to me and helped me get my footing, Dr. Shun-Li Shang, Dr. Richard Otis, Dr. Greta Lindwall, and Dr. Xuan Liu. Additionally, I would

like to thank the members who collaborated and helped me with my research, Dr. Yong-Jie Hu, Dr. Bi-Cheng Zhou, Austin Ross, Hongyeun Kim, Pinwen Guan, and Brandon Bocklund.

Lastly, I want to thank all of my friends at Penn State, my significant other Tobias Frueh, and all of my CALPHAD friends. The list is too long to even begin to name everyone. Graduate school can be difficult but with you guys I enjoyed it every step of the way. I found a family here with all of you and became part of a group of misfit toys, nomad chemistry and a cohort. You taught me new things, explored new places with me, and served as constant support. I will never be able to express how thankful I am to have you all in my life and how fondly I will look back at all of the things we did during this time. I am truly looking forward to all of our future adventures.

Dedication

For my papa, Dr. Jerry Cash. Thank you for inspiring me to get my PhD, helping me improve my writing and listening to me talk about my research.

Chapter 1

Introduction

1.1 Motivation

Titanium (Ti) and its alloys have been used in biomedical applications for many years because of their biocompatibility and corrosion resistance properties [43]. In recent years, there has been an increasing interest in developing better materials for load-bearing implants, due to the increase in total knee and hip replacements. Krutz et al. predicted that the total number of hip and knee replacements would increase by 174% and 673%, respectively, from 2005 to 2030, leading to 572,000 hip and 3.48 million knee procedures in the United States in 2030 [44]. Two of the driving factors for this situation involve the increasing number of younger individuals requiring replacements and the fact that the average life of these implants is only about 7-12 years [45]. These factors contribute significantly to the necessity for better implant materials. The primary considerations for biomedical implants, such as load-bearing knee and hip implants, are biocompatibility, corrosion resistance, fatigue strength, and Young's modulus (E) [43]. In previous years, the most common implants for these applications have been Ti-6Al-4V, stainless steels, and MoCoCr alloys [40, 46]. However, there have been issues with these materials, such as cytotoxicity that has been observed with alloys containing aluminum and vanadium [47]. Another important impediment concerning the common implant materials is stress shielding, which can lead to implant failure. Stress shielding occurs when the E of the implant is higher than that of bone. Due to the difference in Young's moduli, load applications to the joint result in the implant material absorbing all of the stress and causing the bone surrounding the implant to atrophy, which leads to a loss

in bone density, and can result in implant loosening and failure [43]. Table 1.1 summarizes the comparison of the Young’s moduli of common implant materials (> 100 GPa) to bone (10-40 GPa) [43] and shows the extreme elasticity mismatch between the various materials. Using computational thermodynamics to develop a knowledge base of Ti and its alloys is an extremely useful tool in overcoming these challenges.

This work focused on investigating the thermodynamic and elastic properties of the biocompatible Ti-Mo-Nb-Sn-Ta-Zr system. The thermodynamic and elastic properties were calculated using first-principles calculations based on Density Functional Theory (DFT). The parametrization of the properties was completed using the CALPHAD modeling approach. A new computational methodology to predict the metastable phase formation was presented and verified by neutron scattering experiments. The culmination of this work provides a fundamental understanding of the thermodynamics and elastic properties for the Ti-Mo-Nb-Sn-Ta-Zr system.

1.2 Overview

1.2.1 Equilibrium Phases

The phase stability of Ti alloys has been shown to greatly affect the mechanical properties of these materials, so predicting and understanding this aspect of a Ti alloy will greatly impact its effectiveness as a biomedical implant. Titanium is stable in the α (hexagonal close packed, hcp) phase (space group $P6_3/mmc$) under standard temperature and pressure. However, at temperatures above 1155 °K, Ti is stable in the β (body centered cubic, bcc) phase (space group $Im\bar{3}m$). The bcc phase can also be stabilized by alloying, and such bcc Ti alloys have received much attention because of their low E values. Ti in the hcp phase has a E of 105 GPa while, Ti-6Al-4V which is a two phase mixture of hcp and bcc has an E of 110 and the Ti-35Nb-5Ta-7Zr alloy in the bcc phase has a E of 55 GPa which is more comparable to that of bone (10-40 GPa) [43, 48–51]. Bcc phase alloys having lower Young’s moduli has been seen for many other alloys as well, such as Ti-13Nb-13Zr, Ti-35Nb-5Ta-7Zr-0.4O, Ti-29Nb-Ta-Zr, and Ti-25Nb-Ta-Zr which are all bcc alloys that have a E of between 57 and 71 GPa [37, 43, 52]. With phase stability playing

an important role in the alloy selection for load-bearing implants, it is important to study how to stabilize the bcc phase at low temperature (<1155 °K). Mo, Nb and Ta were all chosen to be studied because they are biocompatible elements and strong β -stabilizers, while Zr is a bio-compatible weak β -stabilizer individually but strong stabilizer when in combination with other elements, such as Mo, Nb, and Ta [43]. In conjunction with their biocompatibility, studies have shown Mo, Nb, Ta and Zr have excellent corrosion resistance and no allergy problems [52]. Recently, Sn has also been studied for use in Ti-alloys, due to its low cost [40] and in small concentrations, Sn does not effect the biocompatibility of the alloy.

When many bcc Ti-alloys have been shown to have a E more closely matching that of bone, in some cases a bcc Ti-alloy can miss the mark and not have a E that comes close to matching bone. Such an example is Ti-16Nb-13Ta-4Mo which has E of 110 GPa [38]. So, while understanding the thermodynamics of the system will help to target the bcc phase, also being able to predict the elastic properties before attempting to develop alloys for biomedical implants will reduce the need for trial and error and narrow the scope of alloys being selected for experimental investigation. Therefore, the present study focused on determining the effects of alloying Ti with Mo, Nb, Sn, Ta and Zr on the thermodynamic and elastic properties. The combined DFT and CALPHAD approach was used to evaluate previous models and new models for the binary and ternary alloys in the Ti-Mo-Nb-Sn-Ta-Zr system to build a completed database describing the thermodynamic and elastic properties of the system.

1.2.2 Metastable Phases

The completed thermodynamic database predicts the formation of the equilibrium phases, hcp and bcc. Based on the predictions, alloys that are in the bcc phase can be targeted and their elastic properties predicted. However, Ti and its alloys can form two metastable phases, α'' and ω . α'' is an orthorhombic martensitic phase (space group Cmcm). The martensitic transformation is displacive [53, 54]. Thermodynamically the martensitic transformation is first-order and initiated by supercooling. An applied stress can also contribute to the driving force for a martensitic transformation. Kinetically the martensitic transformation propagates in an athermal manner. The ω phase is a metastable hexagonal phase (space group

P6/mmm) of Ti that has lattice parameters closely matching that of bcc Ti. The ω phase has been seen to form athermally when Ti is alloyed with β stabilizing elements such as Mo, Nb and Ta. It has been shown that different cooling techniques of alloys at certain compositions in the Ti-Mo, Ti-Nb and Ti-Ta systems cause either the α'' phase or the ω phase to form with a matrix of untransformed bcc phase. Quenching the samples leads to the formation of α'' , while slow cooling the samples leads to the formation of ω phase. The formation of these phases causes variations to the predicted elastic properties as seen in Figure 1.1 and 1.2, where the closed symbols represent the calculated E and the open symbols represent the experimentally determined E from the literature. The calculations and experiments agree well on the Ti-rich and Ta-rich sides but in the region marked by the purple box, the experiments show a higher E than predicted by calculations. This is due to the formation of α'' and ω . While the formation of the metastable phases greatly effects the properties of the Ti-alloys, there is no current way to predict their formation.

In this dissertation, a new theoretical framework was proposed to predict the formation. To introduce the theoretical framework and ensure the accuracy, the phase stability and effect on the elastic properties of the α'' and ω phases were studied for the Ti-Nb and Ti-Ta systems. Initially, the ground state energy and elastic properties of multiple structures in the α'' , ω , bcc and hcp were calculated, across all compositions, for the Ti-Ta and Ti-Nb systems. The new theoretic framework predicts the concentrations and phases fractions where the metastable phases form. The predicted phase fractions were then used to predict the E using the rule of mixtures and mixed force constants are used to obtain the phonon density of states (DOS). The reults from inelastic neutron scattering were then used to determine diffraction patterns and phonon density of states. By looking at the diffraction patterns obtained at 300 °K, the phase fractions were obtained and compared to the predicted phase fractions. The phonon DOS obtained from neutron scattering experiments at 300 °K was compared with the mixed force constant first-principles phonon DOS. In order to study what type of transformation takes place for these metastable phases to form, the temperature dependence of the phonon DOS was analyzed. The predicted E using the rule of mixtures was compared with experimental E from literature.

This completed thesis consists of the following main tasks:

1. The thermodynamics of the Ti-Mo-Nb-Sn-Ta-Zr system was investigated using first-principles calculations based on DFT and the CALPHAD method.
 - (a) Previous binary models were evaluated with the available experimental data as well as calculated enthalpy of formation of the bcc phase
 - (b) The thermodynamic description of the Sn-Ta binary alloy was modeled
 - (c) The thermodynamic descriptions of the Ti-containing ternary alloys were modeled
2. The elastic properties of the Ti-Mo-Nb-Sn-Ta-Zr system in the bcc phase were systematically calculated using first-principles based on DFT. The results were used to obtain interaction parameters, following the CALPHAD method, to predict the elastic properties as a function of composition.
3. The metastable phase formation in Ti alloys was investigated by first-principles calculations and experiments carried out for the Ti-Nb and Ti-Ta systems
 - (a) The ground state energies and elastic properties of the Ti-Nb and Ti-Ta systems in the hcp, bcc, ω and α'' were predicted using first-principles calculations
 - (b) From first-principles calculations:
 - i. The new theoretic framework was used to predict the phase fractions
 - ii. The phase fractions were used in a rule of mixtures to plot the phonon density of states and elastic properties
 - (c) From neutron scattering:
 - i. The phase fractions were determined and compared to the calculated predictions
 - ii. The phonon density of states, at 300 °K, was compared to the mixed force constant predicted phonon density of states

iii. The temperature dependent phonon density of states was used to study the transformation that occurs when these metastable phases form

Table 1.1. Young's moduli of common implant materials compared with the Young's modulus of bone [43].

Alloy	Young's Modulus (GPa)
Bone	10-40
cp-Ti*	105
Ti-6Al-4V	110
Stainless Steel	200
CoCrMo	200-230

*cp-commercially pure titanium

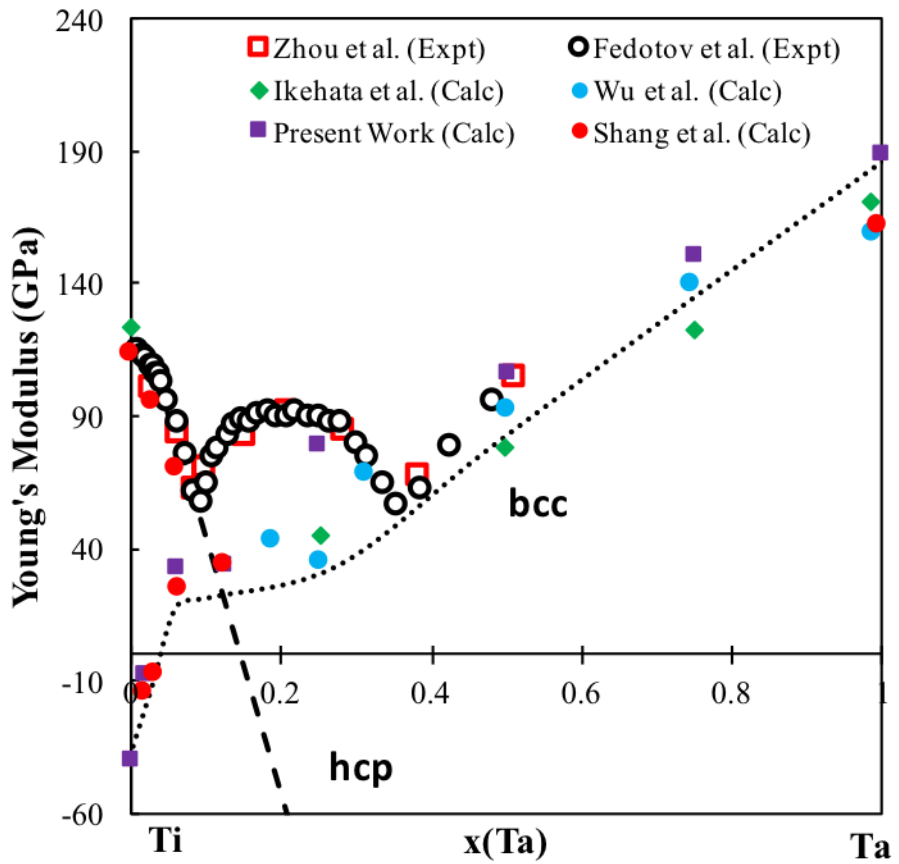


Figure 1.1. Comparison of first-principles calculations [1, 2] and experimental measurements of the Young's modulus of Ti-Ta alloys [3–5]. From 0.10 to 0.35 x(Ta) the calculations and experimentally determined E do not match up due to the formation of two metastable phases ω and α''

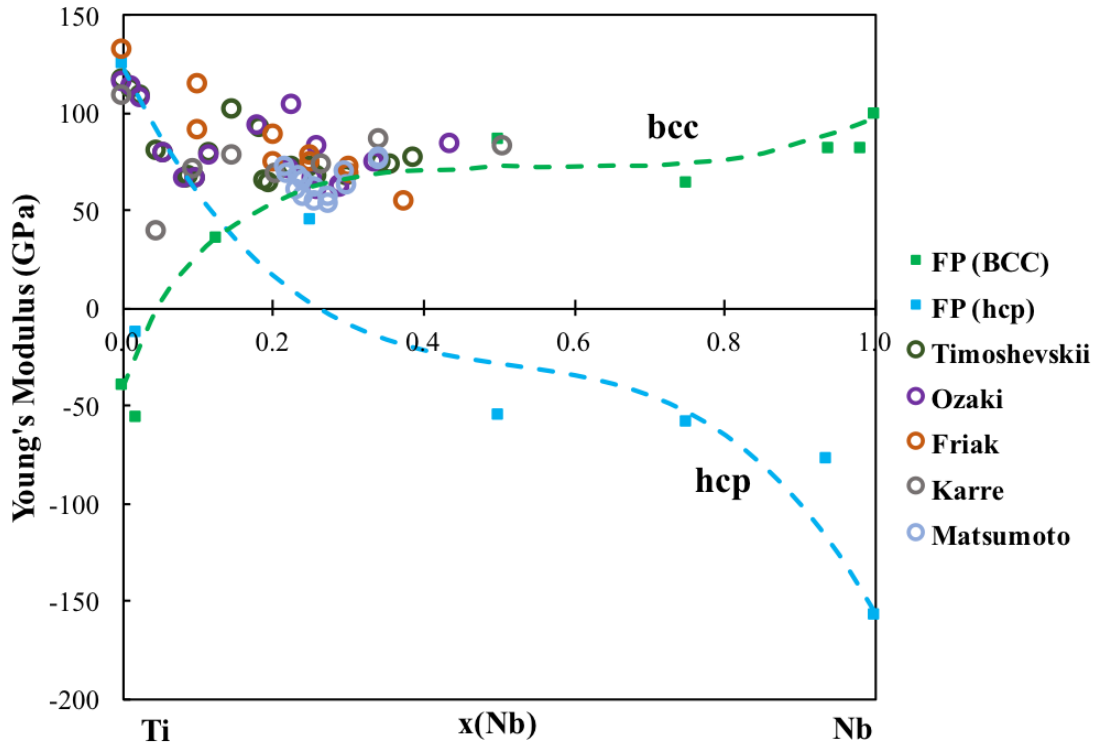


Figure 1.2. Comparison of the present first-principles calculations and experimental measurements of the Young's modulus of Ti-Nb alloys [6–10]. From 0.10 to 0.30 $x(\text{Nb})$ the calculations and experimentally determined E do not match up due to the formation of two metastable phases ω and α''

Chapter 4

First-principles aided thermodynamic modeling of the Sn-Ta system

4.1 Introduction

Currently, the biomaterial implant research of Ti alloys is focused on biocompatible elements that stabilize the body centered cubic (bcc, β) phase of Ti and help to lower its elastic modulus. Tantalum (Ta) is a biocompatible element and is considered to be a strong -stabilizers [51]. Recently, tin (Sn) has also been researched for use in Ti-alloys due to its biocompatibility and low cost [40]. Kuroba et al. [105] studied various Ti-alloys such as Ti-29-Nb-13Ta-2Sn (weight percentage, and similarly hereinafter unless specified otherwise), Ti-29Nb-13Ta-4Mo, and Ti-29Nb-13Ta-6Sn for use as biocompatible implant materials. Kuroba and Hagiwara [106] also studied new Ti-Cu-Ni-Sn-Ta alloys for the artificial materials used in orthopedic surgeries. The Sn-Ta system is thus an important sub-system for this purpose [107]. A complete knowledge base of the thermodynamic description of Sn-Ta can be used to examine the effects of temperature and composition on phase stability for higher order systems and help to tailor experimental alloy selections to viable options. The CALPHAD technique, in combination with first-principles and phonon calculations based on the DFT, has been proven to provide valuable data to model the thermodynamic properties of binary such as Ta-Sn that lack sufficient experimental data [80]. The Sn-Ta system has three solid solution phases and two

intermetallic compounds, i.e. the bcc, body centered tetragonal (bct), and diamond solution phases, and the intermetallic compounds Ta_3Sn with space group $Pm\bar{3}n$ and $TaSn_2$ ($Ta_{1.2}Sn_{1.8}$) with space group $Fddd$ [108].

In the present work, thermodynamic data was predicted using first-principles calculations for the two intermetallics and for the bcc, bct and diamond solution phases. The finite temperature properties of the phases were obtained using the Debye-Grüneisen model [60] and phonon calculations based on the supercell approach [63]. The DFT data was used to model the parameters of the Gibbs energy of each phase using the CALPHAD technique.

4.2 Literature Review

The Sn-Ta binary system was studied by Okamoto [108], Studnitzky and Schmid-Fetzer [109], and Basile [110]. Both of the intermetallic phases, Ta_3Sn and $TaSn_2$, were shown to have a very narrow homogeneity range. Basile [110] observed that $TaSn_2$ is located around $Ta_{1.2}Sn_{1.8}$ which was then designated as Ta_2Sn_3 by Okamoto [108]. It seems that $TaSn_2$ is a more compatible description of the stoichiometric compound based on the descriptions of similar systems (V-Sn, and Nb-Sn) [33, 111, 112], and thus will be used in the present work. Basile [110] determined $TaSn_2$ has a peritectic reaction at 595 °C and used X-ray diffraction (XRD) to elucidate the lattice parameters of $TaSn_2$.

Studnitzky and Schmid-Fetzer [109] used powder samples to study the Ta_3Sn and $TaSn_2$ intermetallic phases and verified the results previously reported by Basile [110]. They cold pressed the pure element powders at 600 MPa and then heated the pellets at 1000 °C for up to 48 hours. The resulting pellet was then cold pressed at 600 MPa again. Under these conditions $TaSn_2$ was observed at 400 °C, but was not present as the temperature increased to 600 °C. In the work by Courtney et al. [113], Ta_3Sn was studied to see how the temperature affects the long-range ordering parameter. In Courtney et al.'s work, Ta_3Sn powder samples were sintered at 600, 700, 950, 1200, and 1450 °C for 2, 4, 7, and 16 days, respectively. Each sample was then studied using x-ray diffraction at room temperature to examine the phases present and the long-range ordering. They concluded that the transition temperature of superconductivity for Ta_3Sn varied by a maximum of 4 °K based on heat treatment and sintering times due to long-range ordering that occurred.

Courtney et al. also measured the lattice parameter of each sample and reported the average value of this cubic phase being 5.285 Å.

4.3 Modeling and Calculations

4.3.1 First-principles details

In the present work, the Vienna ab-initio Simulation Package (VASP) was used to perform the first-principles calculations [61]. The projector augmented-wave (PAW) [62, 90] method was used to describe the electron-ion interactions. Based on the work of comparing X-C functionals (Figure 5.1) the exchange-correlation functional of the generalized gradient approach depicted by Perdew, Burke, and Ernzerhof (PBE) was employed [58]. A sigma value of 0.2 eV and a plane wave energy cutoff of 1.3 times higher than the highest default cutoff was adopted. The Brillouin zone sampling was done with Blöchl corrections [90] using a gamma centered Monkhorst-Pack (MP) scheme [91]. The k-points grid for diamond-Sn, bcc-Ta, TaSn₂, and bcc-Sn were 4x4x4, 6x6x6, 10x10x5, and 6x6x6 respectively. The k-point grids for the bct-Sn, Ta₃Sn and bcc SQS calculations used an automated k-point mesh generator in VASP with the length of the subdivisions specified as 80. The energy convergence criterion of the electronic self-consistency is set as 10⁻⁴ eV/atom and 10⁻⁴ eV/A was set as the stopping criteria for the ionic relaxation loop for all of the calculations.

To calculate the enthalpy of formation of the bcc phase across the entire composition range, the enthalpy of formation of Ta and Sn in the bcc phase were calculated with five different compositions of Ta_{1-x}Sn_x, where x=0.0185 (Ta₅₃Sn, 54 atoms), 0.25, 0.5, 0.75, and 0.9815 (TaSn₅₃, 54 atoms). For x=0.0185 and 0.9815, calculations were performed on a diluted 54 atom cell where all atoms but one was Sn or Ta (Ta₅₃Sn and TaSn₅₃). For x=0.25, 0.5, and 0.75, 16-atom special quasirandom structures (SQS) in the bcc phase developed by Jiang et al. [73] were used to mimic the behavior of random structures. The relaxation of these structures is complicated and discussed in the methodology section. The enthalpy of formation was plotted as a function of composition and then used for the modeling.

4.3.2 CALPHAD

The Gibbs energy functions of the pure elements were adopted from the SGTE (SSUB) database [32]. In the present work, the bcc and liquid phases were modeled in conjunction with the two intermetallics Ta_3Sn and $TaSn_2$. Dilute first-principles calculations of Ta in Sn were done for the diamond and bct phases. However, there is little solubility of Ta in these phases and there is no description of pure Ta in these phases available in SGTE. So, no binary interaction parameters were introduced in the modeling similar to other Sn systems such as Nb-Sn and V-Sn [111, 112]. The interaction parameters of the liquid and bcc solution phases were modeled using Eq. 2.33 and 2.34, while Ta_3Sn and $TaSn_2$ were modeled according to Eq. 2.37.

4.4 Results and discussion

4.4.1 First-principles

To evaluate the accuracy of phonon calculations for the present system, both the dispersion curves and the phonon DOS are plotted for bcc-Ta, bct-Sn, $TaSn_2$, and Ta_3Sn in Figure 4.1, 4.2, 4.3, and 4.4, respectively. The bcc-Ta phonon dispersion curve in Figure 4.1 is compared with values obtained by Taioli et al. [30] using neutron scattering, showing good agreement. The longitudinal modes (LO) and the transverse modes (TO) measured by Raman spectroscopy [31] (open square) along with the previous theoretical predictions at the M point (filled square) for bct-Sn are compared with the calculated phonon dispersion curve in Figure 4.2. The substantial difference for the LO mode may be due to the temperature and pressure differences as pointed out by Olijnyk [31]. No imaginary phonon frequencies are obtained in the phonon DOS plots for bcc-Ta, bct-Sn, $TaSn_2$, Ta_3Sn , indicating that they are all mechanically and dynamically stable at 0 °K.

The calculated lattice parameters at 0 °K from the EOS fitting and with the Debye and phonon models at 298 °K are compared to available experimental and previous DFT results in Table 4.1. The lattice parameters of Ta are compared with the experimental lattice parameters by Predmore and Arsenault [114] at room temperature and the previous 0 °K DFT results by Shang et al. [115] who used the GGA-PW91 exchange correlation functional. The Sn lattice parameters are

compared to experimental work by Allen et al. [116] at 298 °K and calculations by Arróyave et al. [117]. The properties of the TaSn₂ and Ta₃Sn intermetallics are compared to experimental values by Calvert et al. [118] and Courtney et al. [113], respectively. The results show a less than 0.5% difference when compared with other DFT results at 0 °K. There is a less than 2% difference between the DFT 0 °K results and the experiments, which are listed in Table 4.1. The variance is due to the fact that the calculations are at 0 °K and the experiments are at a higher temperature. When comparing the calculated lattice parameters at 298 °K to the experiments, all of the predictions improve to show a less than 1% difference with the exception of Sn, which shows a less than 2% difference.

Table 4.2 shows the equilibrium volume, V_0 , bulk modulus, B , and the derivative of bulk modulus B' obtained by the EOS E-V fitting of the first-principles data at 0 °K. The Sn and Ta calculations are compared with previous first-principles calculations and available experiments. The volume shows a less than 0.5% difference between the previous DFT results and current DFT results for both Sn and Ta [114, 119]. The comparison of the DFT results at 0 °K and the experimental results at 298 °K for volume show a slightly higher variance of less than 5 % due to the difference in temperature [115, 119]. The B comparison of previous 0 °K DFT results and the present 0 °K DFT results show a less than 7 GPa difference and the DFT results at 0 °K vary by less than 11 GPa from the experimental results at 298 °K [114, 115, 119]. The difference between the current calculations and the previous values may be due to many reasons; e.g. the different choices in input parameters used by Peltzer et al. [119] and different exchange correlation functionals. Another reason is due to the temperature difference 0 °K (calculations) versus 298 °K (experiments). Figure 4.5 shows the enthalpy and entropy of Ta from the Debye and phonon approaches in comparison with the data from the SGTE pure element database [32]. Figure 4.6 shows the comparison of the enthalpy and entropy calculated for Sn from the phonon and Debye model to the SGTE pure element database [32]. Both show excellent agreement.

The elastic stiffness constants and polycrystalline elastic properties calculated by the Hill approach and the scaling factors for the Debye model are shown in Table 4.3. To ensure the accuracy of the scaling factor, the elastic stiffness constants and moduli are compared with previous first-principles results [96, 103, 104, 120, 121]. The previous calculation results and present calculation results only vary slightly

for the TaSn_2 structure. The present work calculated the elastic stiffness constants for the Ta_3Sn structure at 2 different atom sizes and compared the results with previous calculations by the Materials Project [96, 103, 104, 120, 121]. The present elastic stiffness results are quite similar. There is a larger variance between the present results and the Materials Project results. This can be attributed to the different input parameters and exchange correlation functional used (PBE in the present work and GGA-PW91 in Materials Project). B calculated from the c_{ij} methodology (designated as B_{cij}) is compared with the B obtained from the EOS fitting (designated as B_{EOS}), showing a difference of less than 3%. Since the B_{EOS} from the EOS fitting is already compared to experiments, the elastic calculations and the scaling factor for the Debye model are thus deemed accurate.

4.4.2 CALPHAD

The PARROT module in the Thermo-Calc software [77] is used to optimize the parameters of the Gibbs energy function of the TaSn_2 and Ta_3Sn intermetallics as well as the binary interaction parameters for the bcc and liquid phases. The Gibbs energy parameters of the intermetallics are first estimated from the thermodynamic properties obtained by the phonon supercell method because the phonon calculations are regarded as more accurate than the Debye model. While the decomposition temperature of the TaSn_2 intermetallic is known to be 868 °K from experiments, the decomposition of the Ta_3Sn intermetallic has not been reported in the literature. It is noted that both the Nb-Sn and V-Sn systems, which are quite similar to the Ta-Sn system, have the X_3Sn phase forming through a peritectic reaction of $\text{bcc} + \text{Liquid} \rightarrow \text{X}_3\text{Sn}$ [33, 111, 112]. Based on the assumption from similar works that Ta_3Sn is also formed through a peritectic reaction, the Ta_3Sn parameters are adjusted and the parameters for the liquid phase are evaluated. The evaluation of the Gibbs parameters along with the results from the Debye model and the phonon quasiharmonic approach for TaSn_2 and Ta_3Sn are plotted in Figure 4.7 and Figure 4.8, respectively. As seen in both figures, the data from the phonon method correlates well with the current CALPHAD modeling. This is to be expected since this data was used to evaluate the parameters. It is noted in Figure 4.7, that the heat capacity and entropy of TaSn_2 from the current CALPHAD modeling is higher than those from the first-principles calculations. This is due to the fact that the

enthalpy and entropy values from DFT were adjusted with the experimental data of the peritectic temperature.

The bct and diamond phases are treated as ideal due to the little solubility. As previously stated, the enthalpies of formation of the bcc phase for five different Sn-Ta compositions are calculated and plotted in Figure 4.9, showing asymmetrical behavior. There is a discrepancy between the first-principles value and the CALPHAD modeling for the lattice stability of bcc-Sn. The first-principles predicts a value of 15.48 kJ/mol-atom and the CALPHAD model gives 4.42 kJ/mol-atom. This difference is expected to be due to the instability of Sn in the bcc phase. Wang et al. [122] concluded and discussed the same discrepancy when comparing first-principles DFT results to SGTE data for Os and Ru. Wang et al. calculated the lattice stability of bcc and fcc (face centered cubic) structure for Os and Ru, both stable in the hexagonal close packed phase at standard temperature and pressure, and concluded a difference of approximately 40 and 60 kJ/mol for Ru and Os, respectively. Wang et al. attributed this difference to the fact that when using first-principles calculations of unstable structures, frequencies of some of the phonon modes would become imaginary and thus the results would be less accurate. On the other hand, the CALPHAD technique can extrapolate lattice stabilities from binary solutions for which an alloying element has stabilized the otherwise unstable structure. These enthalpies of formation calculated from the SQS first-principles calculations are used to evaluate the bcc binary interaction parameters in the present CALPHAD modeling. The enthalpy of formation of the bcc phase is negative at the Ta rich side and becomes positive at the Sn rich side. This is common for X-Sn systems [111, 112], such as the Nb-Sn system [112] shown in Figure 4.9. It should be noted that Toffolon et al. [33, 112] used experimental data on the Sn-rich bcc phase to evaluate the Nb-Sn system's bcc interaction parameters. Due to the asymmetry of enthalpy of formation for the bcc phase, a subregular 1L interaction parameters is introduced.

The interaction parameters obtained in the present work are listed in Table 4.4. Based on these model parameters, the phase diagram is calculated and shown in Figure 4.10. The melting temperature of Ta_3Sn is predicted to be 2884 °K. Both the intermetallics decompose incongruently similar to those in the Nb-Sn and V-Sn systems. As seen in Table 4.4, both intermetallic phases have a negative enthalpy of formation and a negative entropy of formation. This goes along with previous

predictions by Arroyave and Liu [123] where they showed that the enthalpy and entropy of formation have the same sign. The calculated enthalpy of mixing of the liquid phase is plotted in Figure 4.11. The interaction parameter for the liquid phase allows for an accurate representation of the phase stability in Figure 4.10 but may need to be slightly adjusted if experimental data would come available.

4.5 Conclusion

The present work incorporates the thermodynamic data from DFT-based first-principles calculations and the available experimental data in the literature to model the Gibbs energies for the bcc and liquid solution phases and the stoichiometric Ta_3Sn and TaSn_2 phases of the Sn-Ta system. First-principles calculations were used to predict the enthalpy of formation of the bcc phase for the evaluation of interaction parameters in the phase. The decomposition temperature of Ta_3Sn was predicted to be 2884 °K. The completed thermodynamic description is complied into a tdb file. The tdb file and raw data from the first-principles calculations are in appendix b.

Table 4.1. Lattice parameters from first-principles calculations compared with experimental values.

Phase	Space Group	<i>a</i> (Å)	<i>b</i> (Å)	<i>c</i> (Å)	Reference
bcc-Ta	Im $\bar{3}$ m	3.316			This work (0 °K)
		3.328			This work phonon (298 °K)
		3.330			This work Debye (298 °K)
		3.30			Expt. [114]
		3.32			DFT (0 °K) [115]
bct-Sn	I4 ₁ /amd	5.939	3.214		This work (0 °K)
		5.959	3.236		This work phonon (298 °K)
		5.954	3.222		This work Debye (298 °K)
		5.83	3.18		Expt. [116]
		5.93	3.23		DFT (0 °K) [117]
TaSn ₂	Fd ^{ddd}	5.641	9.766	19.200	This work (0 °K)
		5.652	9.786	19.238	This work phonon (298 °K)
		5.652	9.785	19.238	This work Debye (298 °K)
		5.63	9.80	19.18	Expt. [118]
Ta ₃ Sn	Pm $\bar{3}$ n	5.304			This work (0 °K)
		5.319			This work phonon (298 °K)
		5.319			This work Debye (298 °K)
		5.29			Expt. [113]

Table 4.2. Equilibrium volume V_0 , bulk modulus B , and the first derivative of bulk modulus with respect to pressure B' , from fitted equilibrium properties from the EOS at 0 °K compared to experimental work and previous DFT studies.

Phase	V_0 (Å ³ /atom)	B (GPa)	B'	Reference
bcc-Ta	18.241	193.7	3.84	This work
	17.9685	200		Expt. [114]
	18.313	195.3	3.82	DFT [115]
bct-Sn	28.431	47.7	4.61	This work
	27.055	58.0		Expt. [119]
	28.396	54.0		DFT [119]
TaSn ₂	22.631	104.3	4.80	This work
Ta ₃ Sn	18.668	182.4	4.27	This work

Table 4.3. Elastic stiffness constants and elastic properties predicted using the Hill approach and the scaling factors used in the Debye model, calculated from the Poisson ratio, see Eq. 2.12. To ensure the accuracy of the calculated scaling factor, the bulk modulus (B) calculated from the elastic constants was compared to the B_{EOS} calculated from the EOS fitting Eq. 2.6.

	TaSn ₂		Ta ₃ Sn		
	This Work	FP [96, 103, 104, 120]	This Work	This Work	FP [96, 103, 104, 121]
C ₁₁ (GPa)	166	161	297	310	226
C ₁₂ (GPa)	79	78	127	131	155
C ₁₃ (GPa)	62	57			
C ₂₂ (GPa)	189	182			
C ₂₃ (GPa)	68	68			
C ₃₃ (GPa)	187	183			
C ₄₄ (GPa)	37	35	65	68	22
C ₅₅ (GPa)	59	55			
C ₆₆ (GPa)	61	60			
E (GPa)	135		210	202	
G (GPa)	53	51	80	76	27
Poisson Ratio	0.288	0.29	0.32	0.32	0.43
Scaling factor	0.789		0.71	0.71	
B_{cij} (GPa)	107	107	184	190	179
B_{EOS} (GPa)	104		182		

Table 4.4. Modeled parameters in SI units in the present work for the phases in the Sn-Ta binary system. These parameters were incorporated with the SGTE data for the pure elements [32].

Phase (model)	Modeled Paramters
bcc (Sn,Ta)	${}^0L_{Ta,Sn}^b cc = + 70451$
	${}^1L_{Ta,Sn}^b cc = + 112237$
Liquid (Sn,Ta)	${}^0L_{Ta,Sn}^L iq = 17118$
TaSn ₂	$G^{TaSn_2} = {}^0G_{Sn}^{bct} + {}^0G_{Ta}^{bcc} - 29678 - 4.202T$
Ta ₃ Sn	$G^{Ta_3Sn} = {}^0G_{Sn}^{bct} + 3{}^0G_{Ta}^{bcc} - 68844 - 6.000T$

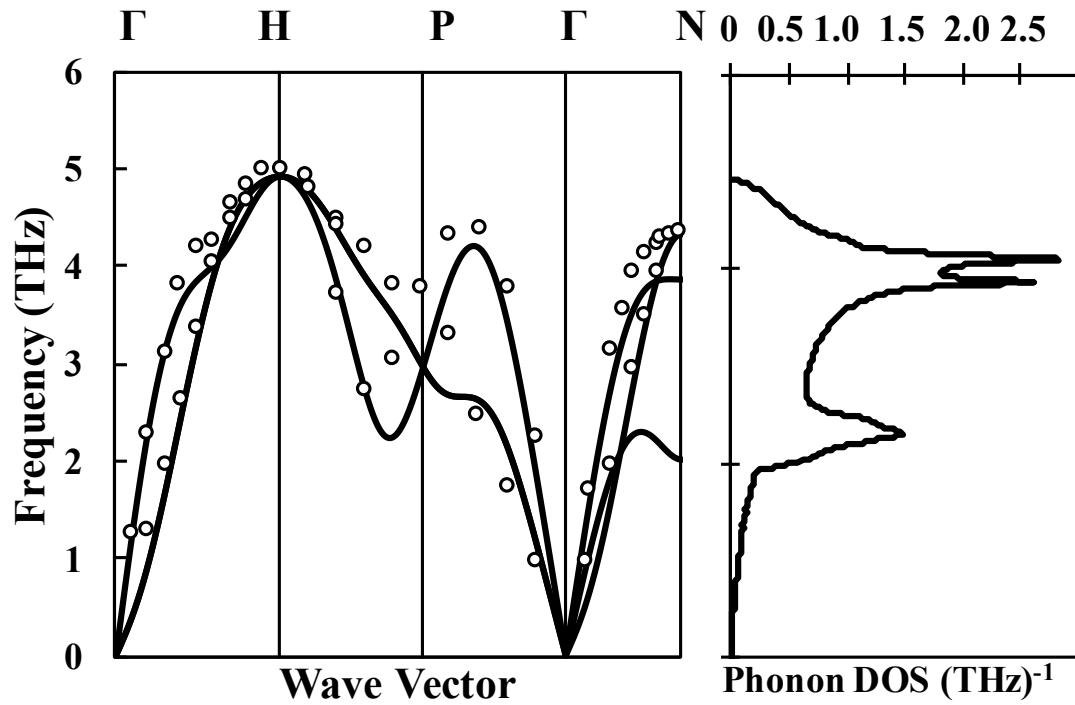


Figure 4.1. Calculated phonon dispersion curve of bcc-Ta, compared with neutron diffraction experiments (\circ) [30] along with the phonon DOS.

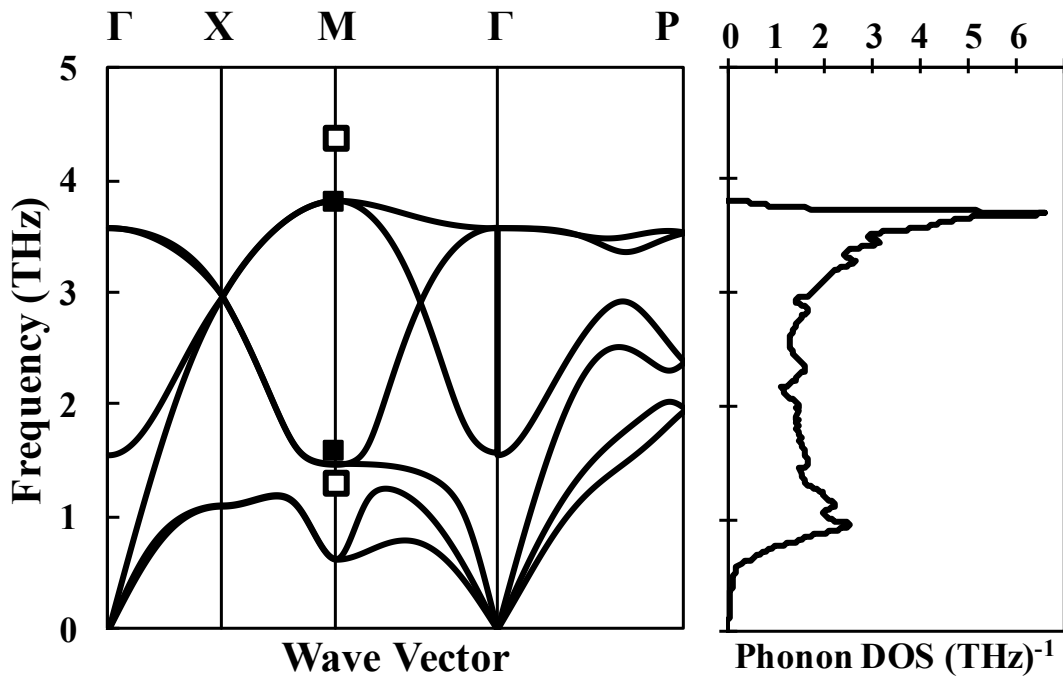


Figure 4.2. Calculated phonon dispersion curve of bct-Sn on the left and phonon DOS on the right. The open squares (\square) are the LO and TO modes from Raman [31] and the filled squares the theoretical prediction of the LO and TO modes at the M point [31].

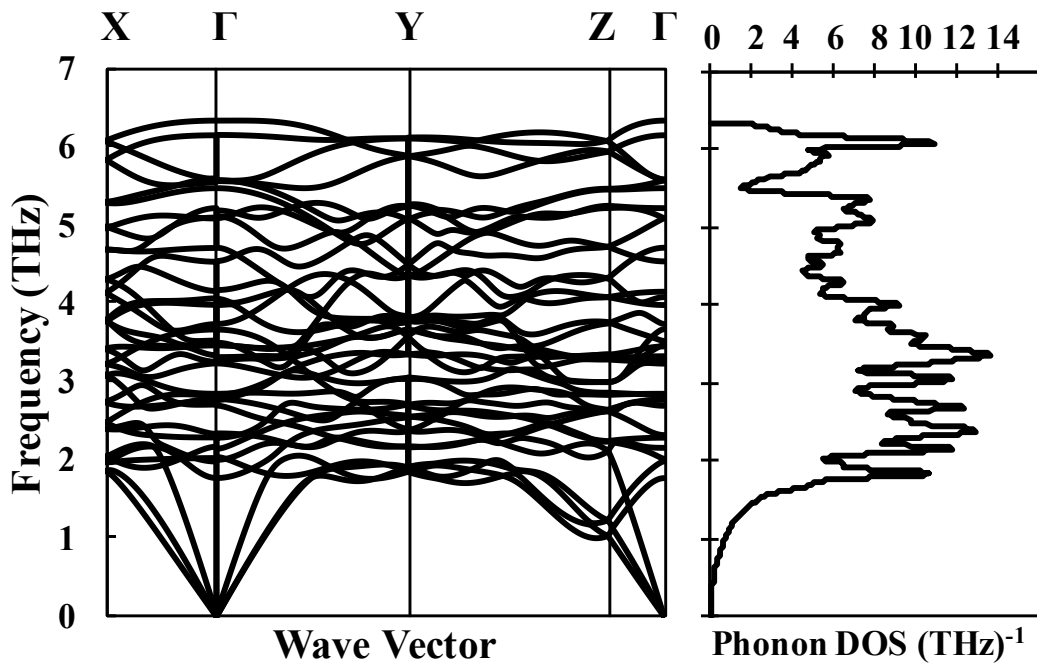


Figure 4.3. Calculated phonon dispersion curve for TaSn_2 at 0 °K and the phonon DOS.

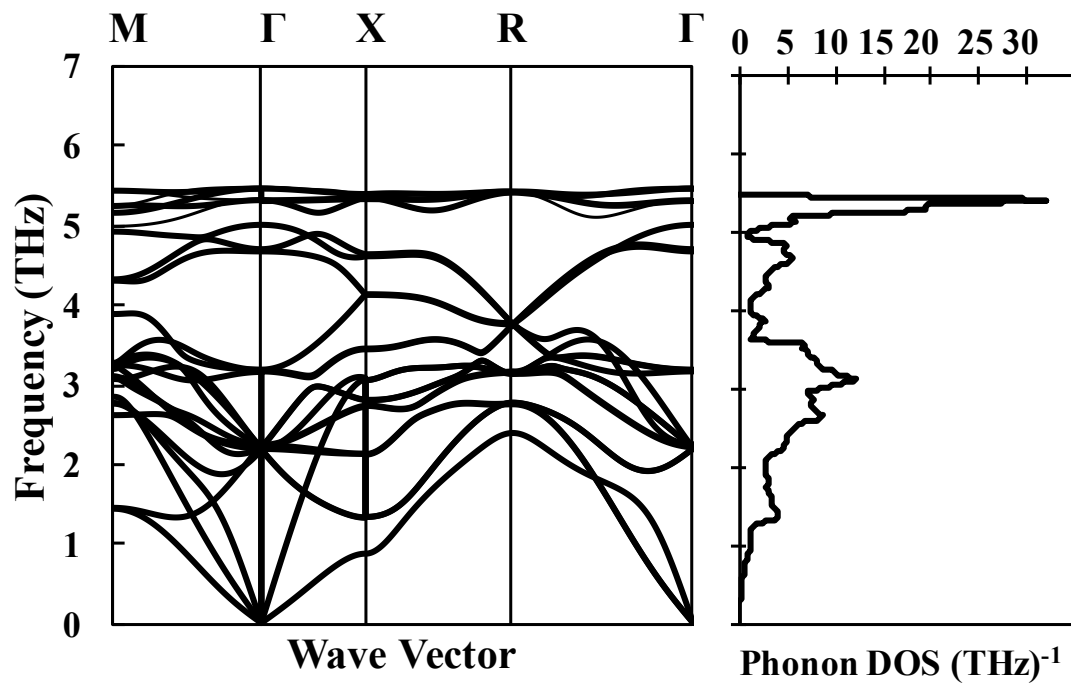


Figure 4.4. Calculated phonon dispersion curve of Ta_3Sn at $0\text{ }^{\circ}\text{K}$ on the left and the phonon DOS on the right.

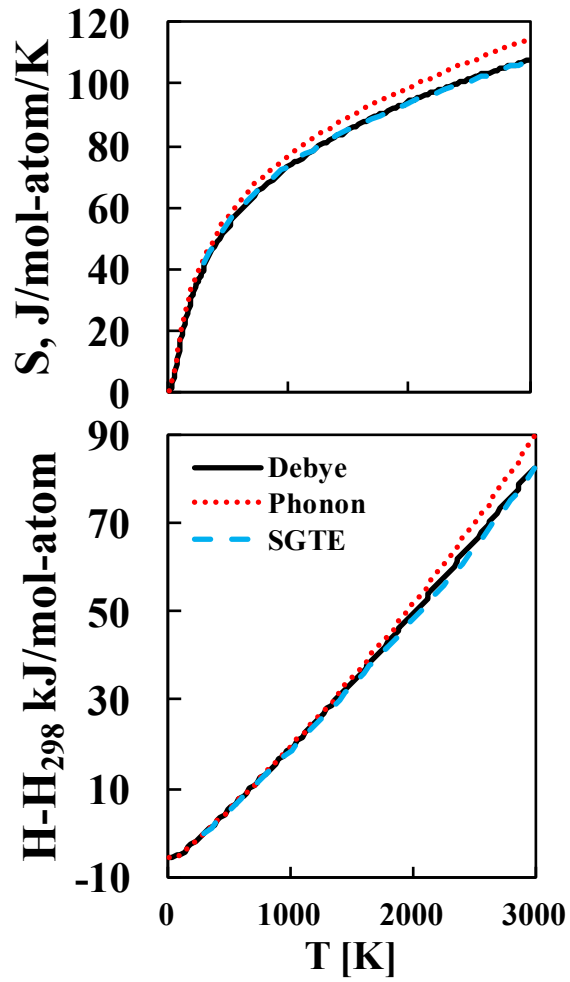


Figure 4.5. Comparison of the enthalpy and entropy of bcc-Ta from the Debye model (solid line) and the quasiharmonic phonon calculations (red dotted line) to the SGTE data (blue dashed line) [32].

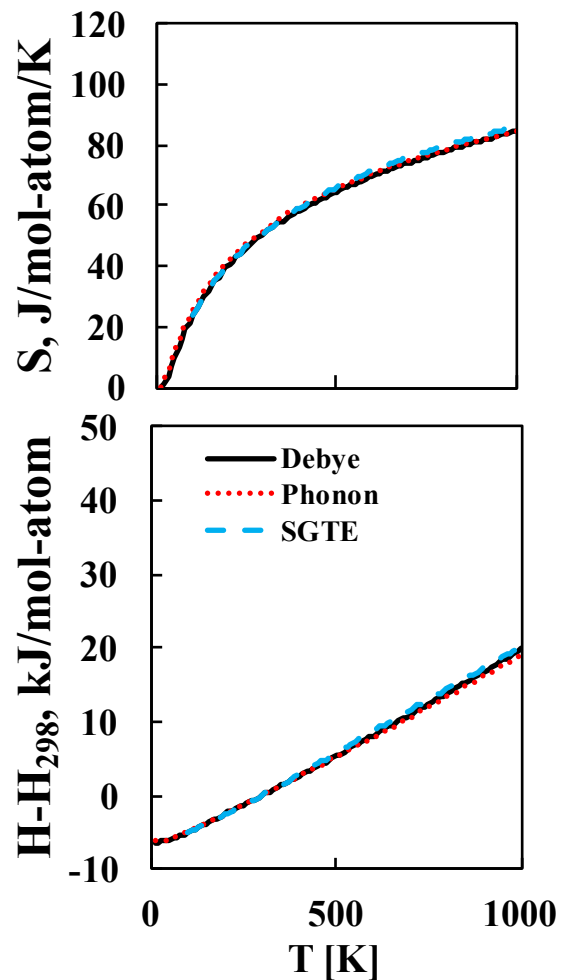


Figure 4.6. Comparison of the Gibbs energy of bct-Sn from the Debye model (solid line) and the quasiharmonic phonon calculations (red dotted line) to the SGTE data (blue dashed line) [32].

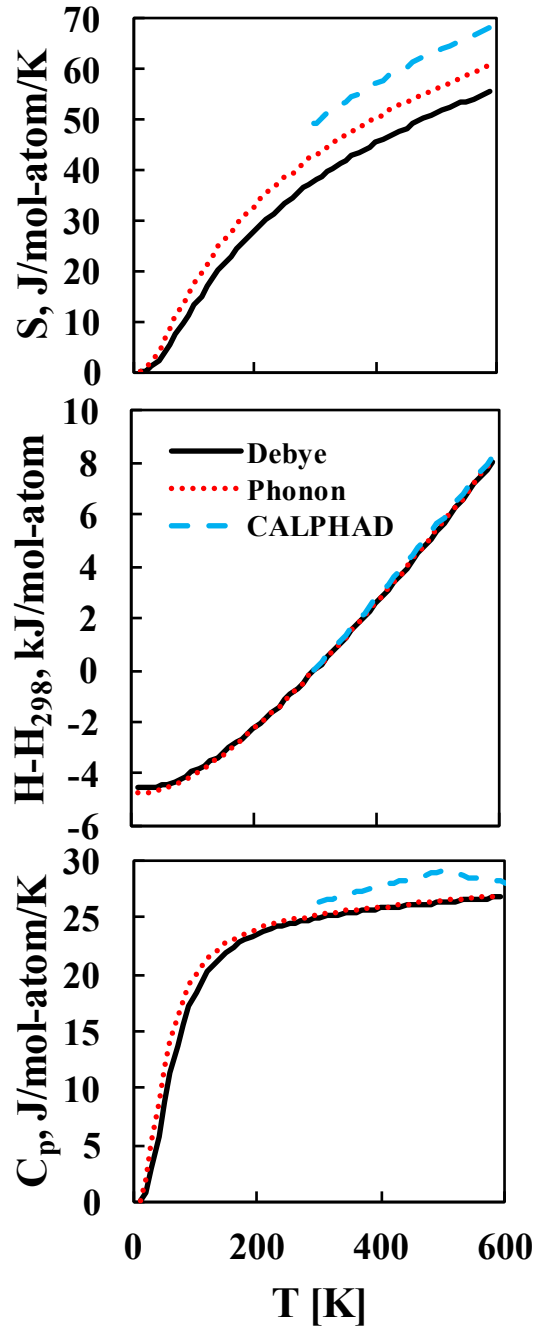


Figure 4.7. Heat capacity, enthalpy and entropy of TaSn_2 using the Debye model (solid line) and the quasiharmonic phonon calculation (red dotted line) from first-principles calculations, compared with those from the current CALPHAD modeling (blue dashed line).

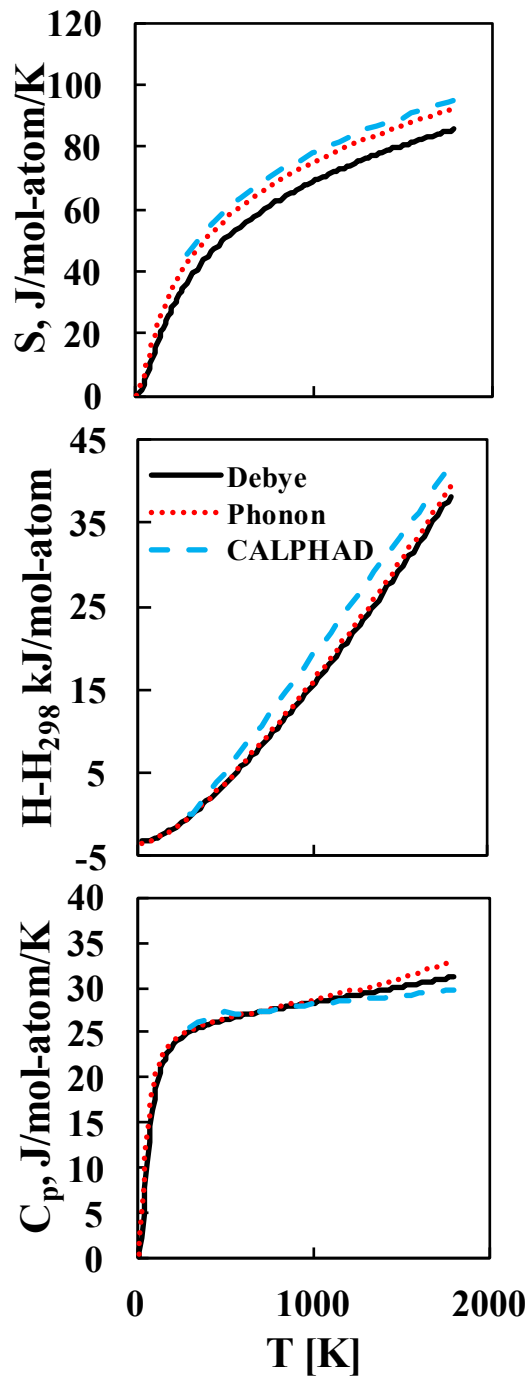


Figure 4.8. Heat capacity, enthalpy and entropy of Ta_3Sn using the Debye model (solid line) and the quasiharmonic phonon calculation (red dotted line) compared with those from the current CALPHAD modeling (blue dashed line).

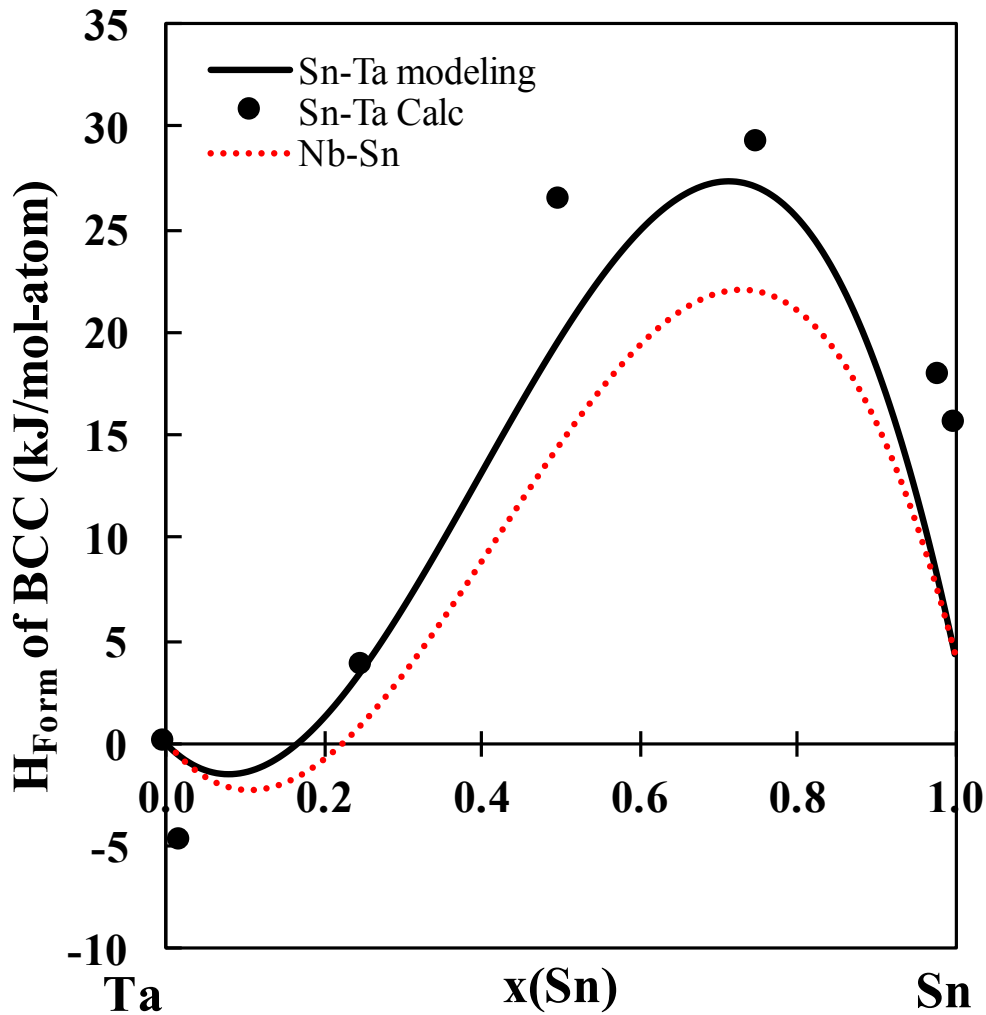


Figure 4.9. Enthalpy of formation of the bcc phase of the Sn-Ta system as a function of composition at 298 °K and ambient pressure from the current CALPHAD modeling (solid line) and from the first-principles calculations (dots), showing asymmetric behavior. This was compared with data of the Nb-Sn system from Toffolon et al. [33] (dashed red line) which was modeled using experimental data, showing similar asymmetric behavior.

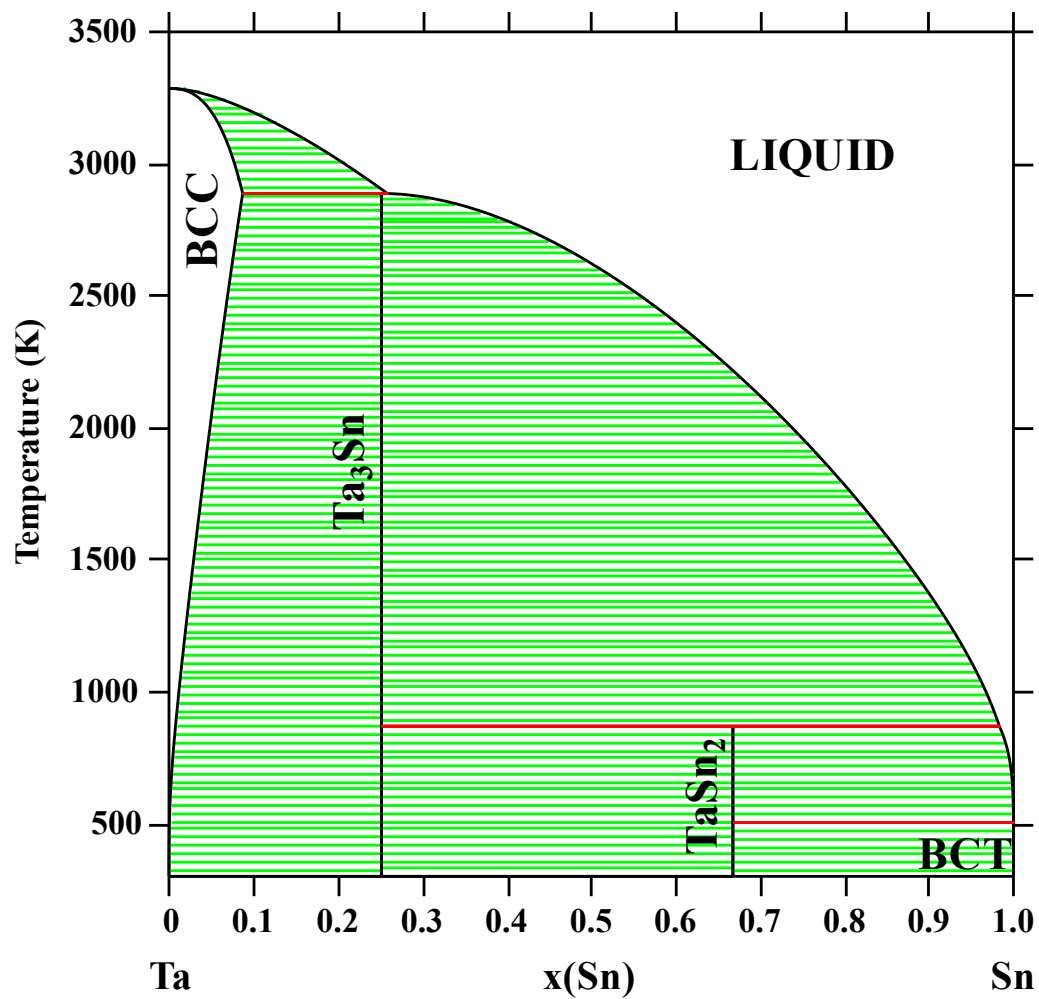


Figure 4.10. Calculated Sn-Ta phase diagram using the present thermodynamic description.

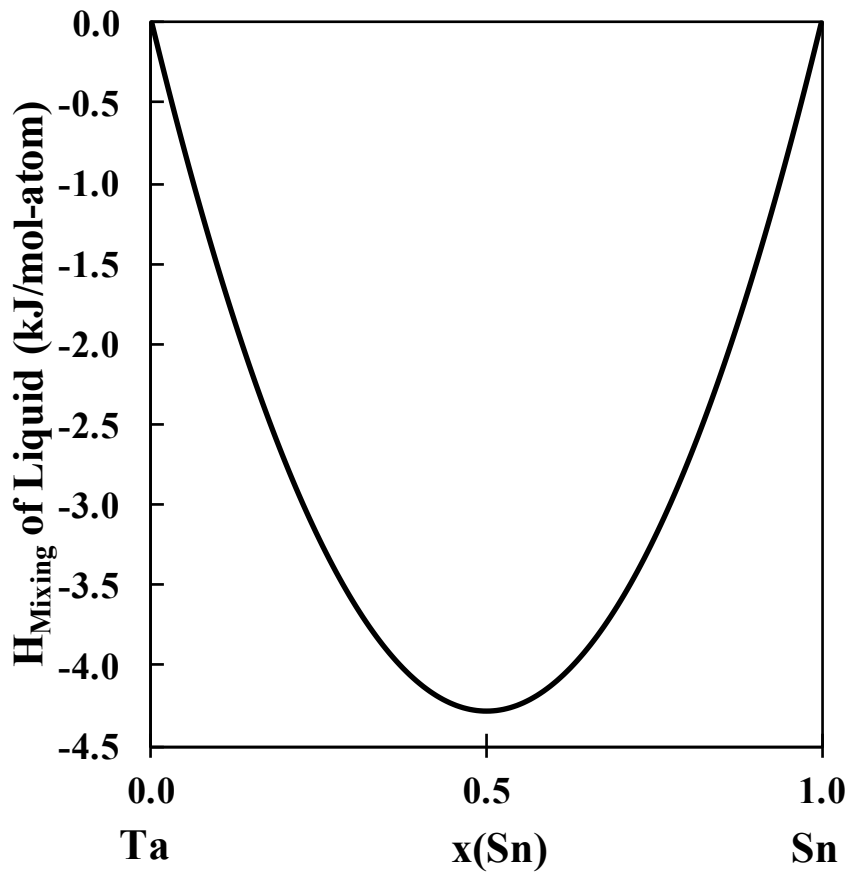


Figure 4.11. Enthalpy of mixing of the liquid phase as a function of composition at 298 °K and ambient pressure in the Sn-Ta system.

Chapter 5 |

Effects of alloying elements on the elastic properties of bcc Ti- X alloys

5.1 Introduction

The present chapter is aimed at studying the effects of alloying elements on the mechanical properties of Ti-alloys as well as completing a database to calculate the elastic properties as a function of composition. This is accomplished by systematically studying the single crystal elastic stiffness constants (c_{ij} 's) and polycrystalline aggregate properties of bcc Ti-X (X = Mo, Nb, Ta, Sn, Zr) alloys. The elastic properties are calculated using first-principles calculations based on density functional theory (DFT). The composition dependence of elastic properties of Ti-X alloys is explored through the dilute solutions and special quasirandom structures (SQS) [73] for concentrated solutions using the methodologies outlined in the methodology chapter. The obtained elastic properties are then fit using the CALPHAD method and extrapolated to higher order Ti-alloys.

5.2 Modeling and Calculations

5.2.1 Calculation details

In the present work the Vienna ab-initio Simulation Package (VASP) [61] was employed to calculate the elastic properties of pure elements and Ti-containing binary systems in the bcc phase. The ion-electron interactions were described using the projector augmented wave (PAW) [62, 90] method. As discussed previously, the use of two X-C functionals were compared in this chapter and based on the results the generalized gradient approach depicted by Perdew, Burke, and Ernzerhof (PBE-GGA) was employed [58]. For consistency, a 310 eV energy cutoff was adopted for all calculations, which is roughly 1.3 times higher than the default value. The energy convergence criterion was 10^{-6} eV/atom, and the Monkhorst-Pack scheme is used for Brillouin zone sampling [61, 91]. The k-points grid for each calculation are listed in Appendix C.

For the Ti-X binary systems, calculations for both dilute and SQS solutions were carried out. Three SQS cells with mole fractions of X atoms at 0.25, 0.5, and 0.75 were employed. Five dilute solutions were calculated for each Ti-X binary alloy using supercell sizes, i.e., Ti_{53}X (54-atom), Ti_{15}X (16-atom), Ti_7X (8-atom), X_{15}Ti (16-atom), and X_{53}Ti (54-atom). The interaction parameters for the elastic stiffness constants were then determined according to the methodology laid out in chapter 2.

5.2.2 Modeling details

The first-principles results were then used to model the elastic stiffness constants. The modeling was completed by calculating the difference between the first-principles calculations and a linear extrapolation between pure elements. The differences were then used to fit to the interaction parameters. Due to the limitations within the PARROT module, a mathematica script was used to fit the interaction parameters. The mathematica script is appended in appendix C. With the focus being Ti-rich alloys, the first-principles results with 70 at. % Ti or higher were weighted heavier (x_6 , according to the authors' practices) than the other points for the fittings. The best fit was found by comparing the fittings obtained with one interaction parameter or with two interaction parameters. The moduli

values were than calculated from the elastic stiffness constants according to the methodology chapter.

5.3 Results and discussion

5.3.1 Evaluation of calculation settings

The X-C functionals of PW91 and PBE were tested in the Ti-Ta binary system. The results are plotted in Figure 5.1, showing the c_{44} values differing by 10 GPa or less and the c_{11} and c_{12} values by less than 5 GPa for high Ta contents and by 26 GPa and 13 GPa with 25 at. % Ta, respectively. Since overall the values vary by an error of less than 0.2 (calculated with Eq. 2.30), and the PBE functional was developed as an improvement of the PW91 functional for metals, the PBE functional was chosen for the present work.

Three magnitudes of strain are tested in the Ti-Mo binary system and plotted in Figure 5.2. The different strain magnitudes do not affect the results significantly. For example, the c_{11} values calculated using ± 0.01 , ± 0.013 , and ± 0.007 strains at $\text{Mo}_{0.94}\text{Ti}_{0.06}$ are 451 GPa, 450 GPa, and 450 GPa, respectively, varying within 1 GPa (< 0.01). The variances in the c_{12} and c_{44} results are similar. Overall, the variances in the c_{11} and c_{12} are less than 0.02 (Eq. 2.30). The largest variance is in the $\text{Ti}_{0.50}\text{Mo}_{0.50}$ where the c_{44} values are 42 GPa, 42 GPa, and 65 GPa calculated with ± 0.01 , ± 0.013 , and ± 0.007 strains, respectively. Overall, the strain magnitude does not affect the calculated results significantly, and thus the ± 0.01 strain magnitude is used for all the calculations.

5.3.2 1.1 Calculations of elastic coefficients in Ti-X binary systems

The elastic stiffness coefficients and bulk moduli (B) are calculated for the pure elements in the bcc structure and reported in Table 5.1. The results in the present work are all obtained at 0 °K without considering the effect of zero-point vibrational energy as discussed in the section of methodology. The results for Mo, Nb and Ta, which are stable in the bcc structure at low temperatures, are compared with experimental data at temperatures shown in Table 5.1 [99, 124]. The error (Eq.

2.30) between the present results and previous results for Mo, Nb and Ta are 0.0261, 0.075, and 0.0425, respectively [68, 99, 124]. This discrepancy is due to the temperature difference between the experiments and calculations. The calculations are at 0 °K while the experimental values were measured at higher temperatures.

Ti and Zr are stable in the hcp structure at low temperatures, and Sn is stable in the body centered tetragonal and diamond structures at low temperatures. Due to the instability of Ti, Sn and Zr in the bcc structure at low temperatures, their elastic stiffness coefficients are compared to previous first-principles calculations at 0 °K [115] that used the PW91 functional, and the errors are 0.024, 0.528 and 0.051, respectively. The differences are related to the instability of the bcc structure, the different exchange correlation functionals and the different input parameters chosen. Due to the bcc instability, multiple relaxation schemes are compared in the present work to find the lowest energy structure retaining the bcc symmetry, making the results the most accurate representation of the bcc pure elements.

Figure 5.3 summarizes the present Young's modulus results for each Ti-X binary system (circles). The solid lines are estimated using the Voigt-Reuss-Hill approach with the elastic coefficients calculated from Eq. 2.38. The model parameters are shown in Table 5.2. The average from the Hill approach is plotted as a solid black line while those from the Voigt (high bound) and Reuss (low bound) approaches are plotted as dotted and dashed lines, respectively. For stable structures the Voigt and Reuss approaches do not vary drastically but when the structures are unstable they show the high and low bounds of the modulus calculations, respectively, with the average from the Hill approach being the value that the database will predict. The results calculated for the Ti-Mo, Ti-Nb, and Ti-Ta systems are compared with previous calculated results from Ikehata et al. [2], and the differences are due to the different input parameters and structures used at each composition. Ikehata et al. used the s orbital electrons as the valance electrons for Ti and used the B2 structure for their $\text{Ti}_{0.5}\text{X}_{0.5}$ compositions with Ti at the body centered site and X at the corner sites. For the $\text{Ti}_{0.25}\text{X}_{0.75}$ and $\text{Ti}_{0.75}\text{X}_{0.25}$ structures they used the DO_3 structure with space group $Fm\bar{3}m$, and not the bcc space group of $Im\bar{3}m$. The present work uses the p electrons as valance electrons for Ti based on updated recommendations by VASP and 16-atom SQS from Jiang et al. [73]. The SQS mimic the random substitution of elements with less error and represent the atomic structures of solution phases better than ordered structures. The results

for the Ti-Mo, Ti-Nb and Ti-Ta systems are compared to available experimental results [3–5, 7, 34–36] in Table 5.3.

Figure 5.3a compares the present results for the Ti-Mo alloy system with experimental data from Zhang et al. [34], Collings et al. [35] and Sung et al. [36]. It can be seen that the Young's modulus increases from pure Ti to pure Mo. The results from Sung et al. [36] differ by about 60 GPa from the present work. However, during the XRD and TEM investigations by Sung et al., one of the metastable phases, α'' and ω , was observed in the samples in addition to the bcc phase. The ω phase is a hexagonal phase (space group P6/mmm) with lattice parameters closely matching those of the bcc phase, and the α'' phase is a martensitic orthorhombic phase (space group Cmcm). The formation of the α'' and ω phases causes variations in the elastic properties from those of the single bcc phase. Zhang et al. [34] and Collings et al. [35] did not observe the formation of either metastable phase. The Young's modulus determined by Zhang et al. and Collings et al. agree with the present Voigt-Reuss bounds but have an error of 0.39 (Eq. 2.30) from the Hill average Young's modulus.

The present Young's modulus of the Ti-Nb system are compared with data from Ozaki et al. [7] and Collings et al. [35] in Figure 5.3b, showing an increase in Young's modulus with an increase in the Nb concentration. The analyses of the samples from the work by Ozaki et al. and Collings et al. depict that all alloys contained the single bcc phase. The Young's modulus from the present first-principles calculations show an error of 0.09 (Eq. 2.30) compared to the Young's modulus determined by Ozaki et al. and Collings et al.

Figure 5.3d shows the calculated Young's modulus for the Ti-Ta system in comparison with the experimental values determined by Fedotov et al. [5] and Zhou et al. [3, 4]. The Young's modulus in the Ti-Ta alloy system increases from pure Ti to pure Ta, and the calculated Young's moduli have an error of 0.19 (Eq. 2.30) compared to the experimental Young's moduli [3–5].

The error between the experimentally determined Young's moduli and the calculated Young's moduli is expected due to the temperature difference (calculations at 0 °K and experiments at 298 °K). The experimentally determined Young's moduli agree well within the Voigt and Reuss bounds, and the present calculations provide good prediction of the elastic properties of the Ti-Mo, Ti-Nb and Ti-Ta alloys as a function of composition.

The calculated Young's moduli for the Ti-Sn (Figure 5.3c) and Ti-Zr (Figure 5.3e) systems cannot be compared to experimental data because the bcc phase is not stable in these systems at low temperatures. For the Ti-Sn alloy system the Young's modulus increases from 0 to 35 at. % Sn and then decreases from 35 to 100 at. % Sn. The Young's modulus data of the Ti-Zr alloy system increases from 0 to 40 at. % Zr, and then decreases from 40 to 100 at. % Zr. Figure 5.4 plots the Young's modulus as a function of composition from pure Ti in the bcc structure to the alloying element ($X = \text{Mo, Nb, Sn, Ta, Zr}$) and compares the effects of each alloying element on the Young's modulus.

Figure 5.5 to Figure 5.7 compare the calculated elastic stiffness coefficients, \bar{C}_{11} , \bar{C}_{12} , \bar{C}_{44} (circles) with the currently modeled elastic stiffness coefficients (solid line) and linear combination from the pure elements for Ti-Mo, Ti-Nb, Ti-Sn, Ti-Ta, and Ti-Zr binary alloys. The previous results from Ikehata et al. [2] are plotted for comparison for the Ti-Mo, Ti-Nb, and Ti-Ta alloys. It can be seen that Mo, Nb, and Ta affect the elastic stiffness coefficients in a similar fashion. As shown in Figure 5.5a, 5.5b and 5.5d the \bar{C}_{11} increases from Ti to X ($X = \text{Mo, Nb, Ta}$). 5.7a, 5.7b and 5.7d show that the \bar{C}_{44} values first decrease and then increase with the addition of the alloying element X ($X = \text{Mo, Nb and Ta}$). The calculated \bar{C}_{12} increases by the addition of Mo or Ta (Figure 5.6a and Figure 5.6d, respectively), and the \bar{C}_{12} first decreases and then increases by the addition of Nb (Figure 5.6b). A similar trend is shown in the \bar{C}_{11} and \bar{C}_{12} data for the Ti-Sn system (Figure 5.5 and Figure 5.6c). The \bar{C}_{11} and \bar{C}_{12} values first increase and then decrease from pure Ti to pure Sn. As seen in Figure 5.7c, \bar{C}_{44} first increases, then decreases, and then increases again from pure Ti to pure Sn. In the Ti-Zr system, the \bar{C}_{11} and \bar{C}_{44} values first increase and then decrease with increasing Zr concentration (Figure 5.5e and Figure 5.7e). For the Ti-Zr system, the calculated \bar{C}_{12} values first decrease and then increase, as shown in Figure 5.6e. The calculated values are listed in Table 5.3.

As discussed in the methodology (chapter 2), the instability of the bcc phase can be determined by Born's criteria (Eq. 2.21-2.23). Figure 5.8 shows the $\bar{C}_{11} - \bar{C}_{12}$ values from first-principles calculations and the present modeling, indicating the stability and instability regions of the bcc phase in different Ti-alloys. When the $\bar{C}_{11} - \bar{C}_{12}$ is positive the bcc phase is mechanically stable and when the $\bar{C}_{11} - \bar{C}_{12}$ is negative the bcc phase is mechanically unstable. The bcc phase is mechanically

unstable at Mo, Nb, Sn, Ta, and Zr concentrations of less than 5.5, 11.5, 51.5, 9.5 and 4.0 at. %, respectively. Alloying with only 4.0 at. % Zr stabilizes the bcc phase, which is the lowest alloying concentration of any of the alloying elements even though it is known as a weak β -stabilizer. 5.5, 9.5 and 11.5 at. % of Mo, Ta and Nb, respectively, are needed to alloy with Ti in order to stabilize the bcc phase. Mo, Nb, and Ta are similar elements that are all stable in the bcc phase and known to be β -stabilizers. 51.5 at. % of Sn is needed to stabilize the bcc phase when alloyed with Ti. Sn is not stable in the bcc phase and is not a β -stabilizer. Based on the E mapping in Figure 5.4, the compositions that fall into the target E range for the biomedical application (10-40 GPa) are targeted. However, the bcc phase of the targeted alloy compositions needs to be stable, which is determined by Figure 5.8. Using these results, the composition range for each Ti-X alloy that has the target E and the bcc phase stable are listed in Table 5.4. The Ti-Mo, Ti-Nb, Ti-Ta and Ti-Zr alloys show small compositions ranges where both the criteria are met while Ti-Sn has no composition range that stabilizes the bcc phase and has the target E . From these results, alloying with more than one element is probably required to reach the properties desired.

Figure 5.9 and Figure 5.10 show the shear (G) and bulk moduli (B) of the Ti-X (X = Mo, Nb, Sn, Ta, Zr) systems, with the present results (circles), the Hill average (solid black line), and Voigt (purple dashed line) and Reuss (yellow dashed line) bounds plotted. Similar trends in the B and G data are seen for the Ti-Mo, Ti-Nb and Ti-Ta systems. The B and G increase with increasing Mo, Nb and Ta concentration, as shown in Figure 5.9 and Figure 5.10, respectively. The bulk and shear moduli values increase and then decrease from pure Ti to pure Sn in the Ti-Sn system (Figure 9c and Figure 10c). In the Ti-Zr system, the B decreases from pure Ti to pure Zr (Figure 5.9e) and the G first increases and then decreases from pure Ti to pure Zr (Figure 5.10e). The calculated values are listed in Table 5.3.

5.3.3 Extrapolation to ternary and higher ordered systems

The interaction parameters in Table 5.2 can be used to predict the elastic stiffness coefficients of higher order Ti-alloys by summing the interaction parameters of each binary alloy contained in the multi-component alloy from Eq. 2.38. The

predicted elastic stiffness coefficients of the multi-component alloys can be used to calculate the Young's modulus as a function of composition, as shown in Figure 5.4. The average from the Hill approach is plotted as a solid line while the Voigt and Reuss bounds are plotted as dotted and dashed lines, respectively. The accuracy of prediction of the elastic properties of higher ordered Ti alloys are evaluated by comparing the predicted results with previous experimental results [37–40] as shown in Figure 5.11 and Table 5.5. The black diagonal line represents a perfect correlation between the predicted and experimental Young's moduli. The grey region indicates the error (3 GPa) in the first-principles calculations, which is the average variance in \bar{C}_{11} , \bar{C}_{12} and \bar{C}_{44} from Eq. 2.18-2.20.

It can be seen that the difference between experimental Young's moduli at the same composition from Niinomi et al. [40], Geetha et al. [38], Tane et al. [37] and Mohammad et al. [39] varies from 2 GPa to 46 GPa with different heat treatments and measuring techniques. The scattering in the Young's moduli among experimental measurements is denoted by the vertical error bars in Figure 5.11. The horizontal error bars show the Young's moduli ranges from the Reuss and Voigt bonds with the average from the Hill approach marked by the circle. The experimental Young's moduli deviate from the present predictions by 0.69 to 14 GPa. This difference can be contributed to the temperature difference between the first-principles data and the experimental results and uncertainties in calculations and experiments. Considering the fact that the experimental results from the literature at the same composition vary drastically, the present first-principles calculations give a good representation of the elastic properties of higher order Ti-alloys. Introducing the binary interaction parameters of non-Ti containing alloys in the system and the ternary interaction parameters can further improve the database predictions.

5.4 Conclusion

The elastic properties of five bcc Ti-X (X = Mo, Nb, Sn, Ta, Zr) systems, including the elastic stiffness coefficients, bulk modulus, shear modulus, and Young's modulus, were systematically studied using first-principles calculations at different compositions. The CALPAHD methodology was used to evaluate interaction parameters of the elastic properties as a function of composition. The present calculations showed

that 5.5, 11.5, 51.5, 9.5, and 4.0 at. % of Mo, Nb, Sn, Ta and Zr, respectively, are required to stabilize the bcc structure according to the Born criteria. The trends observed were summarized for each Ti-X (X= Mo, Nb, Sn, Ta, Zr) binary system. Alloying with Mo, Nb, and Ta resulted in similar trends, which is probably because Mo, Nb, and Ta are strong bcc stabilizers and stable in the bcc structure at room temperature. The interaction parameters determined in the current work were used to predict the elastic properties of higher order alloys. The accuracy of database predictions of the Young's modulus was evaluated by comparing the calculated and experimental Young's moduli. Overall, the database provided good predictions of the elastic properties of Ti-alloys in the bcc phase as a function of composition.

Table 5.1. Calculated pure element elastic stiffness constants and the bulk modulus B (in GPa) by X-C functional of PBE are compared with the previous first-principles calculations (FP) by X-C functional PW91 and experiments (Expt). Sv, pv and d refereeing to the s, p, and d states being treated as valance, respectively.

Pure Elements		\bar{C}_{11}	\bar{C}_{11}	\bar{C}_{11}	B
Ti_sv	This work 0 °K	93	115	41	108
	Calc 0 °K [115]	96	116	40	107
Mo_pv	This work 0 °K	475	164	108	268
	Expt 73 °K [68]	473	156	111	
	Expt 300 °K [124]	473	160	109	261
Nb_sv	This work 0 °K	245	144	27	178
	Expt 4 °K [68]	253	133	31	
	Expt 300 °K [99]	247	135	29	172
Sn_d	This work 0 °K	50	52	29	51
	Calc 0 °K [115]	30	60	18	48
Ta_pv	This work 0 °K	278	164	81	202
	Expt 0 °K [68]	266	158	87	
	Expt 300 °K [99]	267	161	83	196
Zr_sv	This work 0 °K	86	91	32	89
	Calc 0 °K [115]	82	94	30	90

Table 5.2. Evaluated interaction parameters L_0 and L_1 using the R-K polynomial Eq. 2.38 for the elastic stiffness constants for the Ti-X binary systems.

Alloy	Interaction Parameter	Ti-Mo	Ti-Nb	Ti-Sn	Ti-Ta	Ti-Zr
\bar{C}_{11}	L_0	-22.16	40.46	119.46	83.65	246.97
	L_1	0	0	0	-67.76	-135.95
\bar{C}_{12}	L_0	-36.40	-32.39	15.90	38.05	-110.53
	L_1	0	0	-146.80	0	78.00
\bar{C}_{44}	L_0	-142.9	-41.54	59.79	-51.96	70.06
	L_1	0	-41.95	-94.38	0	0

Table 5.3: First-principles calculations of the elastic stiffness constants, bulk modulus B , shear modulus G , and Young's modulus E in GPa for different atomic percent compositions of the bcc Ti-X binary systems at 0 °K. As well as experimental data for the Young's modulus obtained at 300 °K by the reference stated.

Reference	$\text{Ti}_{1-b}\text{X}_b$	\bar{C}_{11}	\bar{C}_{12}	\bar{C}_{44}	B	G	E
This work	Ti	93	115	41	108	-12.91	-40.34
This work	$\text{Ti}_{0.94}\text{Mo}_{0.06}$	124	111	38	115	20	54
This work	$\text{Ti}_{0.87}\text{Mo}_{0.13}$	146	113	29	124	23	65
This work	$\text{Ti}_{0.75}\text{Mo}_{0.25}$	178 ± 3	123 ± 15	32 ± 11	141 ± 15	30 ± 15	84 ± 15
This work	$\text{Ti}_{0.50}\text{Mo}_{0.50}$	268 ± 9	136 ± 19	42 ± 9	180 ± 19	51 ± 19	138 ± 19
This work	$\text{Ti}_{0.25}\text{Mo}_{0.75}$	385 ± 9	146 ± 6	66 ± 6	226 ± 9	84 ± 9	224 ± 9
This work	$\text{Ti}_{0.06}\text{Mo}_{0.94}$	451	158	96	256	114	397
This work	$\text{Ti}_{0.02}\text{Mo}_{0.98}$	464	163	100	263	118	308
This work	Mo	475	164	108	268	125	325
Expt 300 K [34]	$\text{Ti}_{0.92}\text{Mo}_{0.08}$						83
Expt 300 K [34]	$\text{Ti}_{0.88}\text{Mo}_{0.12}$						90
Expt 300 K [35]	$\text{Ti}_{0.92}\text{Mo}_{0.08}$						84
Expt 300 K [35]	$\text{Ti}_{0.89}\text{Mo}_{0.11}$						89
Expt 300 K [35]	$\text{Ti}_{0.82}\text{Mo}_{0.18}$						101
This work	$\text{Ti}_{0.98}\text{Nb}_{0.02}$	93	115	35	108	-18	-56
This work	$\text{Ti}_{0.87}\text{Nb}_{0.13}$	116	116	37	116	11	31
This work	$\text{Ti}_{0.75}\text{Nb}_{0.25}$	140 ± 11	116 ± 13	34 ± 10	124 ± 13	22 ± 13	63 ± 13
This work	$\text{Ti}_{0.50}\text{Nb}_{0.50}$	181 ± 9	121 ± 2	31 ± 10	141 ± 9	31 ± 10	86 ± 10
This work	$\text{Ti}_{0.25}\text{Nb}_{0.75}$	208 ± 3	130 ± 4	15 ± 10	156 ± 4	22 ± 10	64 ± 10
This work	$\text{Ti}_{0.06}\text{Nb}_{0.94}$	242	134	18	170	28	81
This work	$\text{Ti}_{0.02}\text{Nb}_{0.98}$	242	134	18	170	28	81
This work	Nb	245	144	27	178	35	98
Expt 300 K [7]	$\text{Ti}_{0.71}\text{Nb}_{0.29}$						67
Expt 300 K [7]	$\text{Ti}_{0.66}\text{Nb}_{0.34}$						74
Expt 300 K [7]	$\text{Ti}_{0.56}\text{Nb}_{0.44}$						84
Expt 300 K [35]	$\text{Ti}_{0.74}\text{Nb}_{0.26}$						64
Expt 300 K [35]	$\text{Ti}_{0.70}\text{Nb}_{0.30}$						65
Expt 300 K [35]	$\text{Ti}_{0.66}\text{Nb}_{0.34}$						73

Table 5.3: First-principles calculations of the elastic stiffness constants, bulk modulus B , shear modulus G , and Young's modulus E in GPa for different atomic percent compositions of the bcc Ti-X binary systems at 0 °K. As well as experimental data for the Young's modulus obtained at 300 °K by the reference stated.

Reference	$\text{Ti}_{1-b}\text{X}_b$	\bar{C}_{11}	\bar{C}_{12}	\bar{C}_{44}	B	G	E
Expt 300 K [35]	$\text{Ti}_{0.56}\text{Nb}_{0.44}$						83
This work	$\text{Ti}_{0.94}\text{Sn}_{0.06}$	100	122	46	115	-10	-30
This work	$\text{Ti}_{0.75}\text{Sn}_{0.25}$	105 ± 5	114 ± 2	60 ± 4	111 ± 5	11 ± 5	31 ± 5
This work	$\text{Ti}_{0.50}\text{Sn}_{0.50}$	88 ± 9	93 ± 9	46 ± 4	91 ± 9	10 ± 9	29 ± 9
This work	$\text{Ti}_{0.25}\text{Sn}_{0.75}$	92 ± 9	55 ± 7	35 ± 8	67 ± 9	27 ± 9	72 ± 9
This work	Sn	50	52	29	51	7	21
This work	$\text{Ti}_{0.98}\text{Ta}_{0.02}$	100	115	39	110	-3	-9
This work	$\text{Ti}_{0.94}\text{Ta}_{0.06}$	116	113	30	114	11	32
This work	$\text{Ti}_{0.87}\text{Ta}_{0.13}$	120	121	39	121	11	32
This work	$\text{Ti}_{0.75}\text{Ta}_{0.25}$	167 ± 1	140 ± 3	45	149 ± 3	28 ± 3	78 ± 3
This work	$\text{Ti}_{0.50}\text{Ta}_{0.50}$	208 ± 1	159	51 ± 3	175 ± 1	38 ± 3	106 ± 3
This work	$\text{Ti}_{0.25}\text{Ta}_{0.75}$	239 ± 7	143 ± 5	62 ± 3	175 ± 7	56 ± 7	152 ± 7
This work	$\text{Ti}_{0.06}\text{Ta}_{0.94}$	257	158	72	191	62	168
This work	$\text{Ti}_{0.02}\text{Ta}_{0.98}$	264	163	72	197	62	169
This work	Ta	278	164	81	202	70	189
Expt 300 K [5]	$\text{Ti}_{0.62}\text{Ta}_{0.38}$						62
Expt 300 K [5]	$\text{Ti}_{0.58}\text{Ta}_{0.42}$						79
Expt 300 K [5]	$\text{Ti}_{0.52}\text{Ta}_{0.48}$						95
Expt 300 K [3]	$\text{Ti}_{0.62}\text{Ta}_{0.38}$						67
Expt 300 K [3]	$\text{Ti}_{0.49}\text{Ta}_{0.51}$						105
This work	$\text{Ti}_{0.98}\text{Zr}_{0.02}$	112	106	43	108	17	48
This work	$\text{Ti}_{0.75}\text{Zr}_{0.25}$	148 ± 14	82 ± 7	54 ± 7	104 ± 14	44 ± 14	116 ± 14
This work	$\text{Ti}_{0.50}\text{Zr}_{0.50}$	152 ± 17	76 ± 12	48 ± 12	101 ± 17	44 ± 17	115 ± 17
This work	$\text{Ti}_{0.25}\text{Zr}_{0.75}$	126 ± 12	82 ± 3	45 ± 3	97 ± 12	34 ± 12	91 ± 12
This work	$\text{Ti}_{0.06}\text{Zr}_{0.94}$	89	90	34	90	9	27
This work	Zr	86	91	32	89	6	16

Table 5.4. Predicted Young's modulus (in GPa) of higher order alloys in the bcc phase compared to experimental values found with both the weight percent and atomic percent listed.

Alloy	at Target E	bcc stabilized	Target Compositions
Ti-Mo	Pure Ti to 0.10 mol Mo	> 0.055 mol Mo	0.055 to 0.10 mol Mo
Ti-Nb	Pure Ti to 0.20 mol Nb	> 0.115 mol Nb	0.115 to 0.20 mol Nb
Ti-Sn	Pure Ti to 0.40 mol Sn	> 0.515 mol Sn	N/A
Ti-Ta	Pure Ti to 0.15 mol Ta	> 0.095 mol Ta	0.095 to 0.15 mol Ta
Ti-Zr	Pure Ti to 0.05 mol Zr	> 0.040 mol Zr	0.040 to 0.05 mol Zr

Table 5.5. Predicted Young's modulus (in GPa) of higher order alloys in the bcc phase compared to experimental values found with both the weight percent and atomic percent listed.

Alloy Name (%wt)	at %	Calc E	Expt E
Ti-35Nb-7Zr-5Ta [38]	Ti-24Nb-5Zr-2Ta	81	80
Ti-29Nb-13Ta-4.6Zr [38]	Ti-20Nb-5Ta-3Zr	76	75
Ti-29Nb-13Ta-6Sn [38]	Ti-21Nb-5Ta-3Sn	68	74
Ti-29Nb-13Ta-4.6Sn [38]	Ti-20Nb-5Ta-3Sn	67	66
Ti-29Nb-13Ta-4.5Zr [38]	Ti-20Nb-5Ta-3Zr	76	65
Ti-29Nb-13Ta-4.6Zr [37]	Ti-21Nb-5Ta-3Zr	76	64
Ti-30Nb-10Ta-5Zr [37]	Ti-23Nb-4Ta-3Zr	77	64
Ti-35Nb-10Ta-5Zr [37]	Ti-25Nb-4Ta-4Zr	80	65
Ti-24Nb-4Zr-7.9Sn [39]	Ti-15Nb-3Zr-4Sn	65	54
Ti ₃₅ Nb ₂ Ta ₃ Zr [39]	Ti-23Nb-1Ta-2Zr	69	61
Ti-29Nb-11Ta-5Zr [39]	Ti-20Nb-6Ta-2Zr	74	60
Ti-10Zr-5Ta-5Nb [39]	Ti-6Zr-1Ta-3Nb	64	52
Ti-29Nb-13Ta-2Sn [39]	Ti-20Nb-5Ta-1Sn	66	62

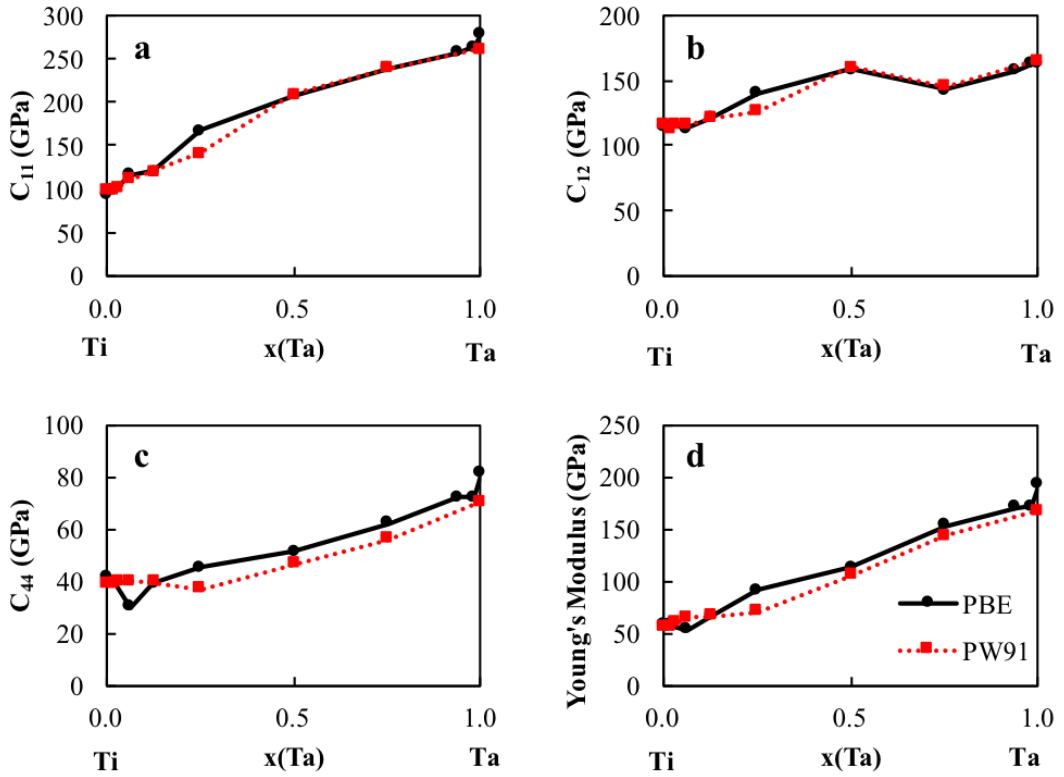


Figure 5.1. Elastic stiffness constants of the bcc Ti-Ta binary system calculated with the GGA and PBE exchange correction functions, respectively.

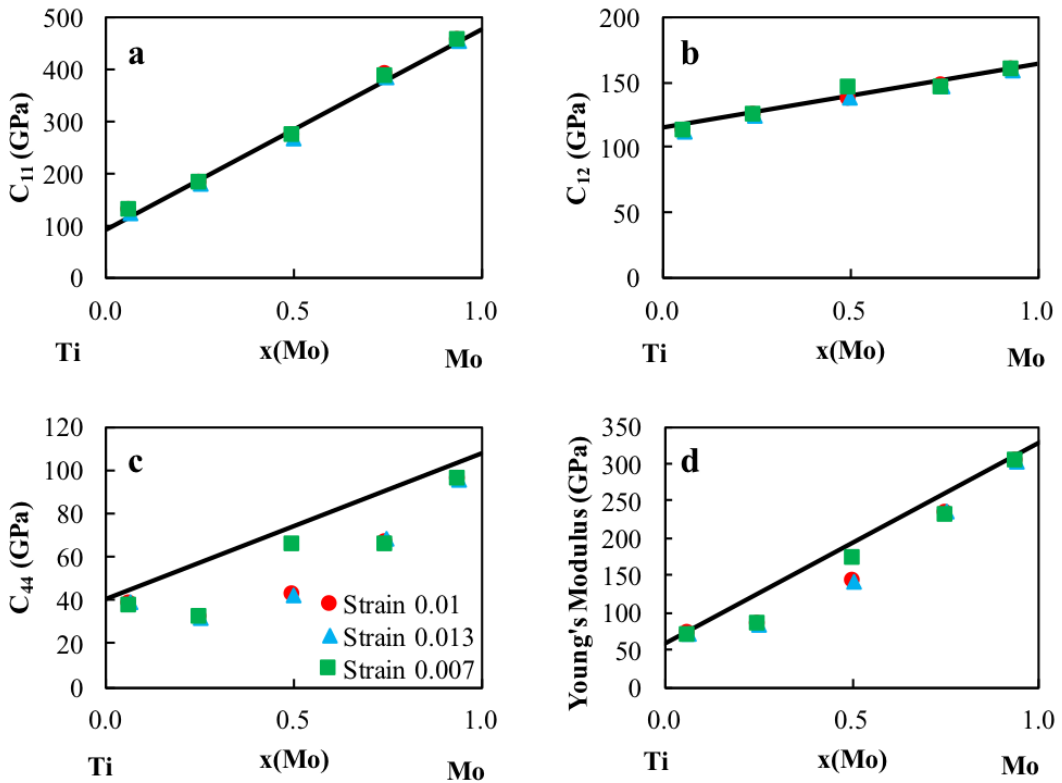


Figure 5.2. Elastic stiffness constants for the bcc Ti-Mo binary system calculated with strains, ± 0.01 , ± 0.03 and ± 0.07 , respectively, showing comparable results.

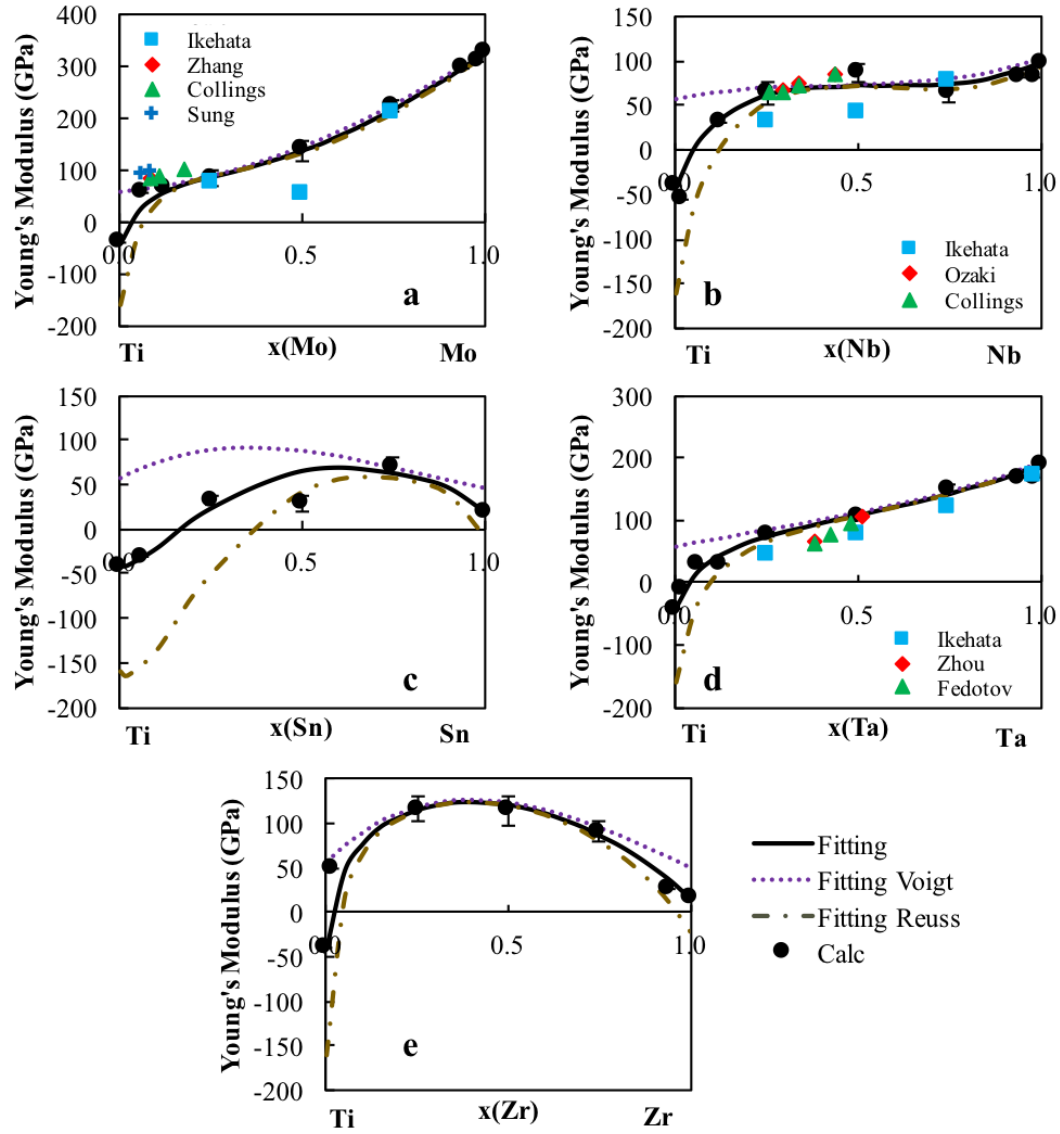


Figure 5.3. Young's modulus E of the Ti-X binary systems. The present calculations are plotted as the filled circles with the error bars. The dotted purple line is the Voigt upper Young's modulus bound, the gold dot dashed line is the lower Reuss Young's modulus bound and the black line is the Hill Young's modulus average. The experimental values [1–5, 7, 8, 34–36] are also included for comparison.

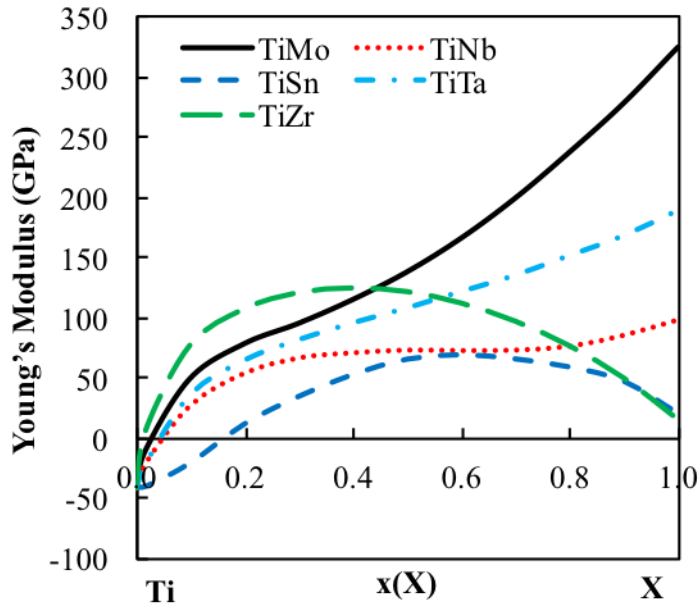


Figure 5.4. Young's modulus calculated from the model parameters (see 5.2) and Eq. 2.30 as a function of composition from bcc Ti to bcc X.

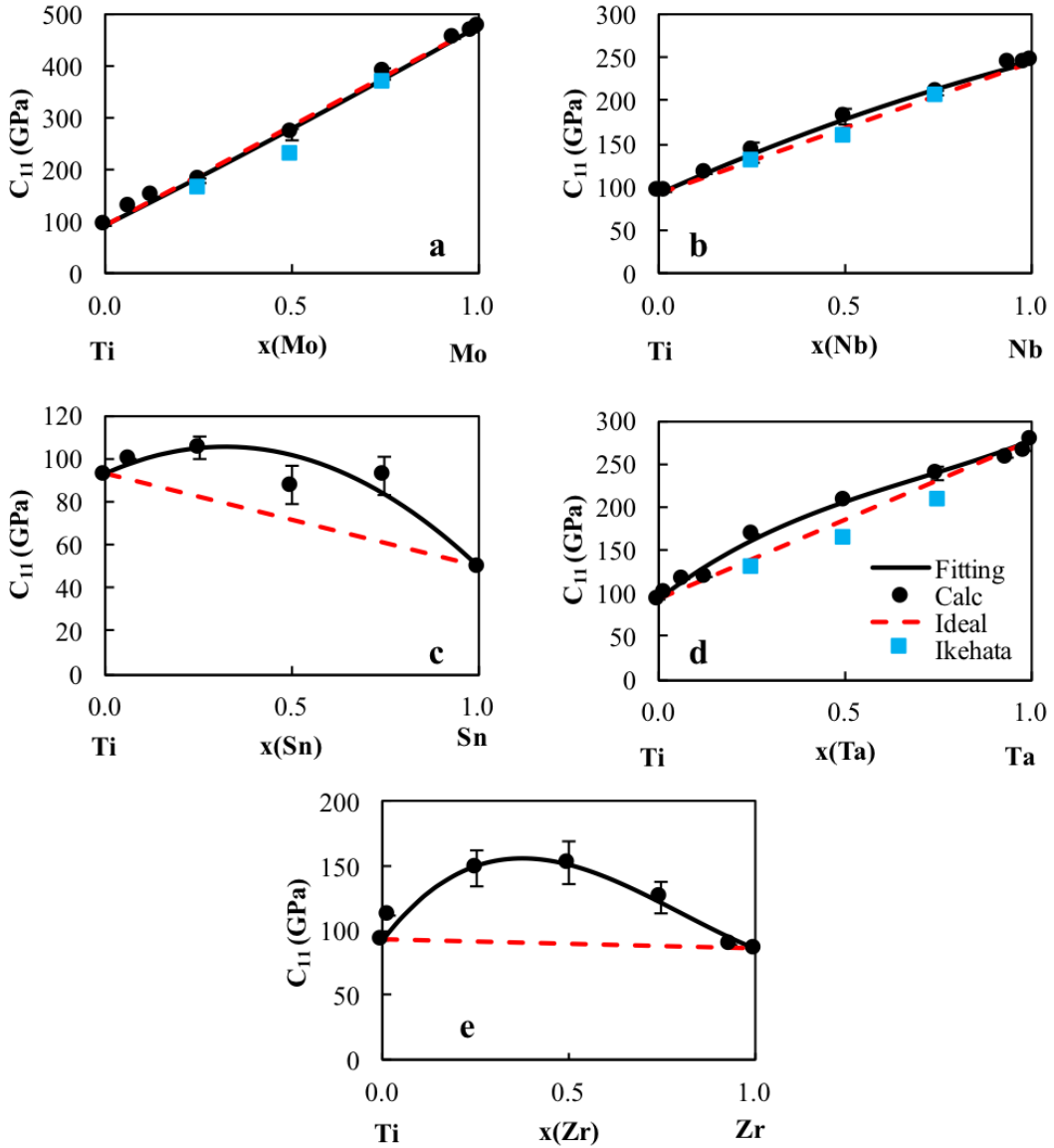


Figure 5.5. Calculated \bar{C}_{11} values (circles) plotted with their errors as well as the pure element extrapolation (red dashed line) and the present modeling (black dashed line) for five Ti-X binary systems ($X = \text{Mo}, \text{Nb}, \text{Ta}, \text{Sn}, \text{Zr}$). Ti-Mo, Ti-Nb, and Ti-Ta alloys are compared with previous calculations from Ikehata et al. [2].

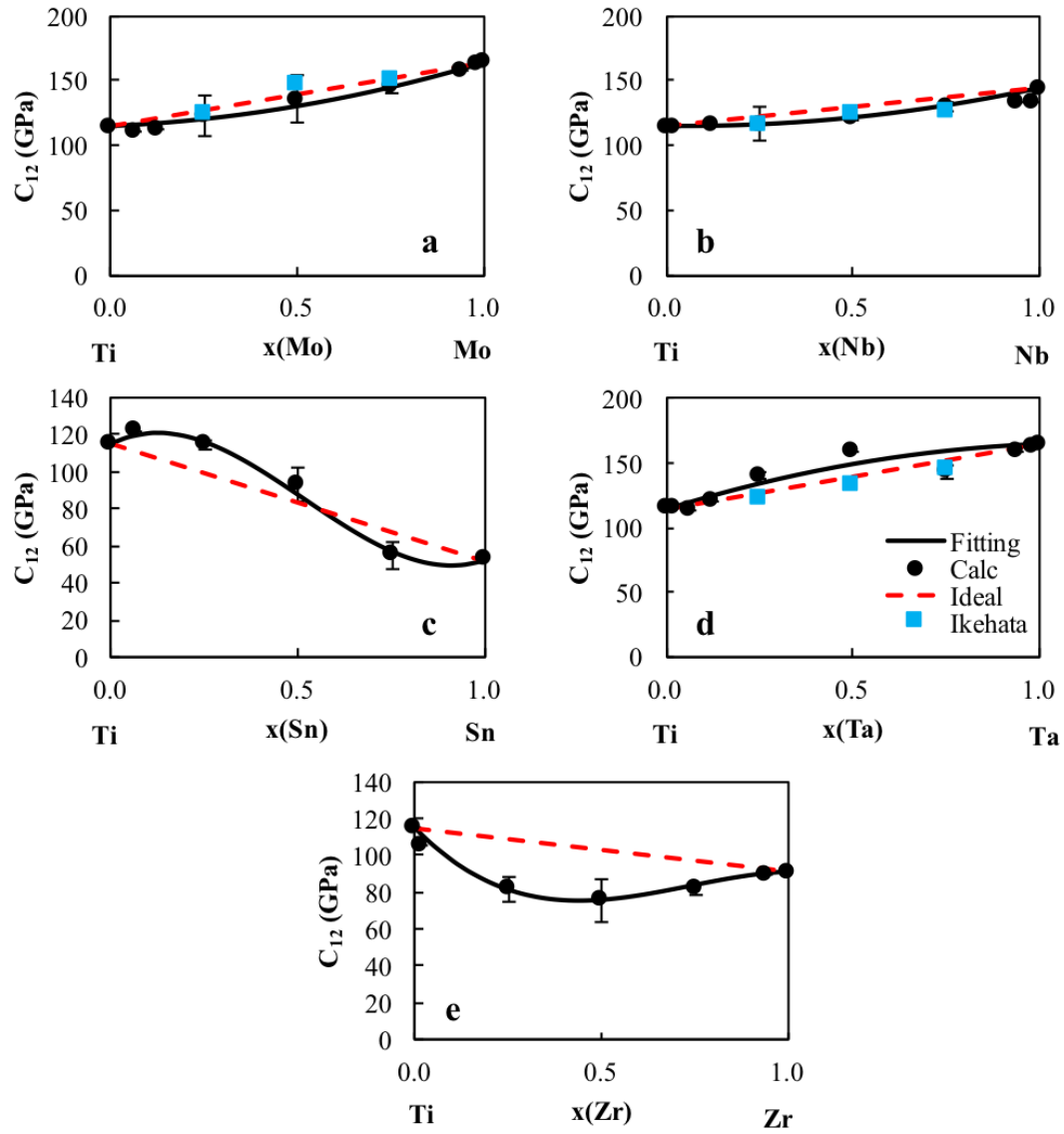


Figure 5.6. Calculated \bar{C}_{12} values (circles) plotted with their errors as well as the pure element extrapolation (red dashed line) and the present modeling (black dashed line) for five Ti-X binary systems ($X = \text{Mo}, \text{Nb}, \text{Ta}, \text{Sn}, \text{Zr}$). Ti-Mo, Ti-Nb, and Ti-Ta alloys are compared with previous calculations from Ikehata et al. [2].

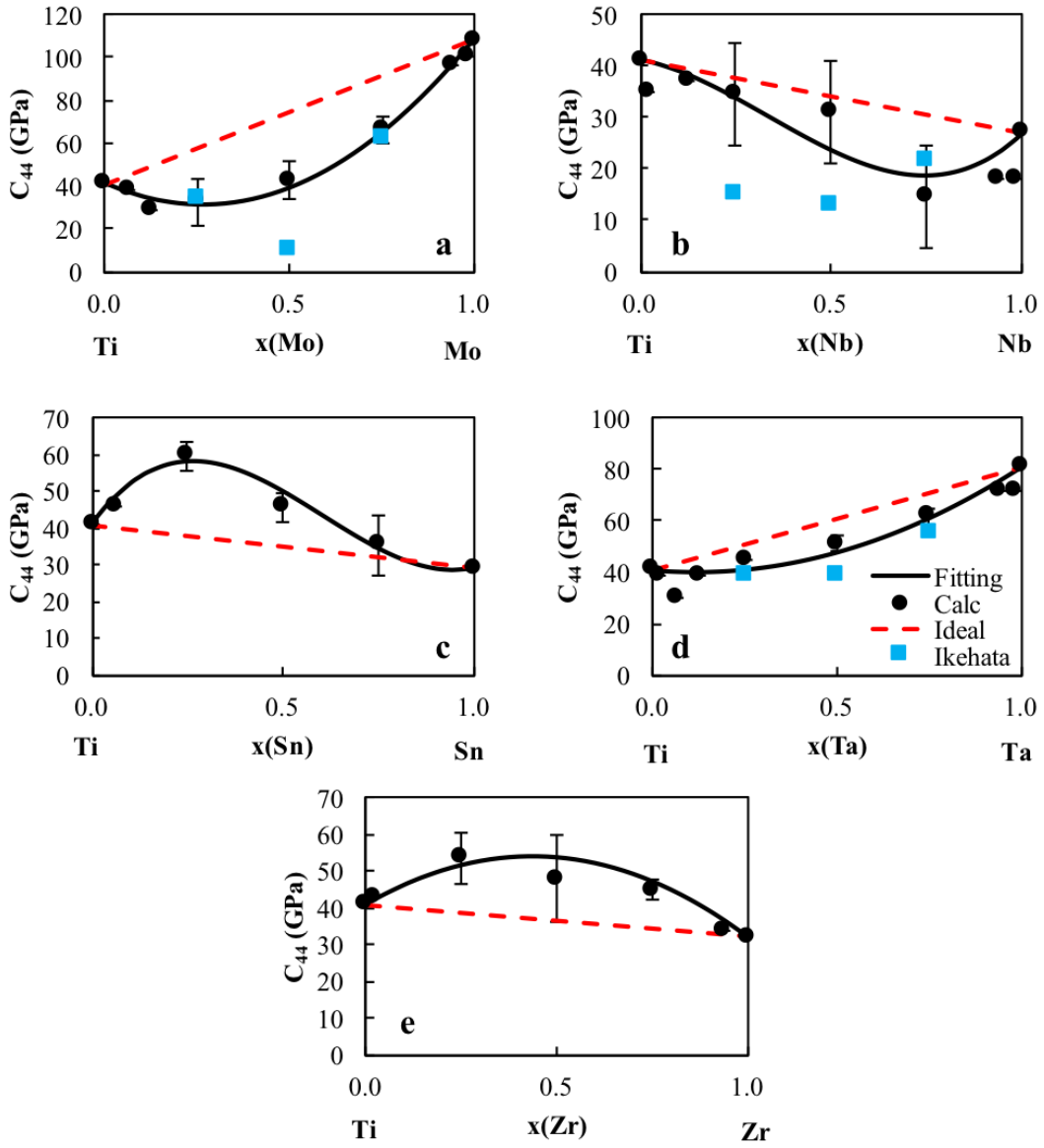


Figure 5.7. Calculated \bar{C}_{44} values (circles) plotted with their errors as well as the pure element extrapolation (red dashed line) and the present modeling (black dashed line) for five Ti-X binary systems ($X = \text{Mo}, \text{Nb}, \text{Ta}, \text{Sn}, \text{Zr}$). Ti-Mo, Ti-Nb, and Ti-Ta alloys are compared with previous calculations from Ikehata et al. [2].

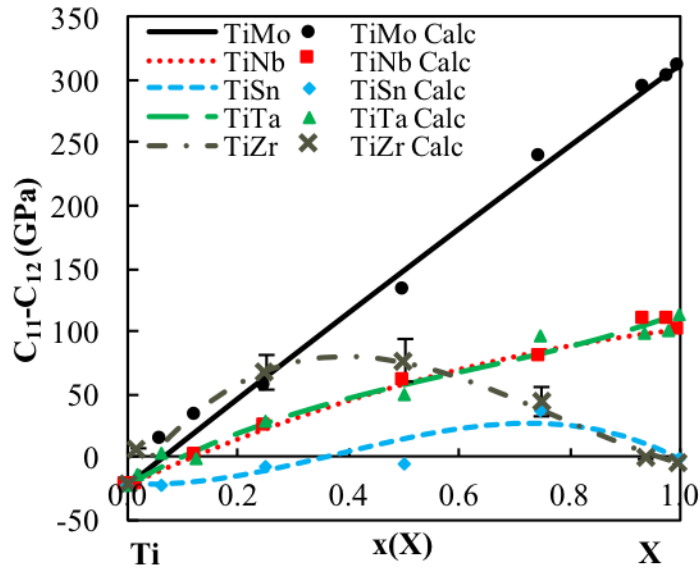


Figure 5.8. Calculated $\bar{C}_{11} - \bar{C}_{12}$ values (circles) plotted with the present modeling (solid lines) for five Ti-X binary systems ($X = \text{Mo, Nb, Ta, Sn, Zr}$). The $\bar{C}_{11} - \bar{C}_{12}$ shows the stability of the bcc phase. When the $\bar{C}_{11} - \bar{C}_{12}$ value is negative the bcc phase is not stable in the corresponding compositions range.

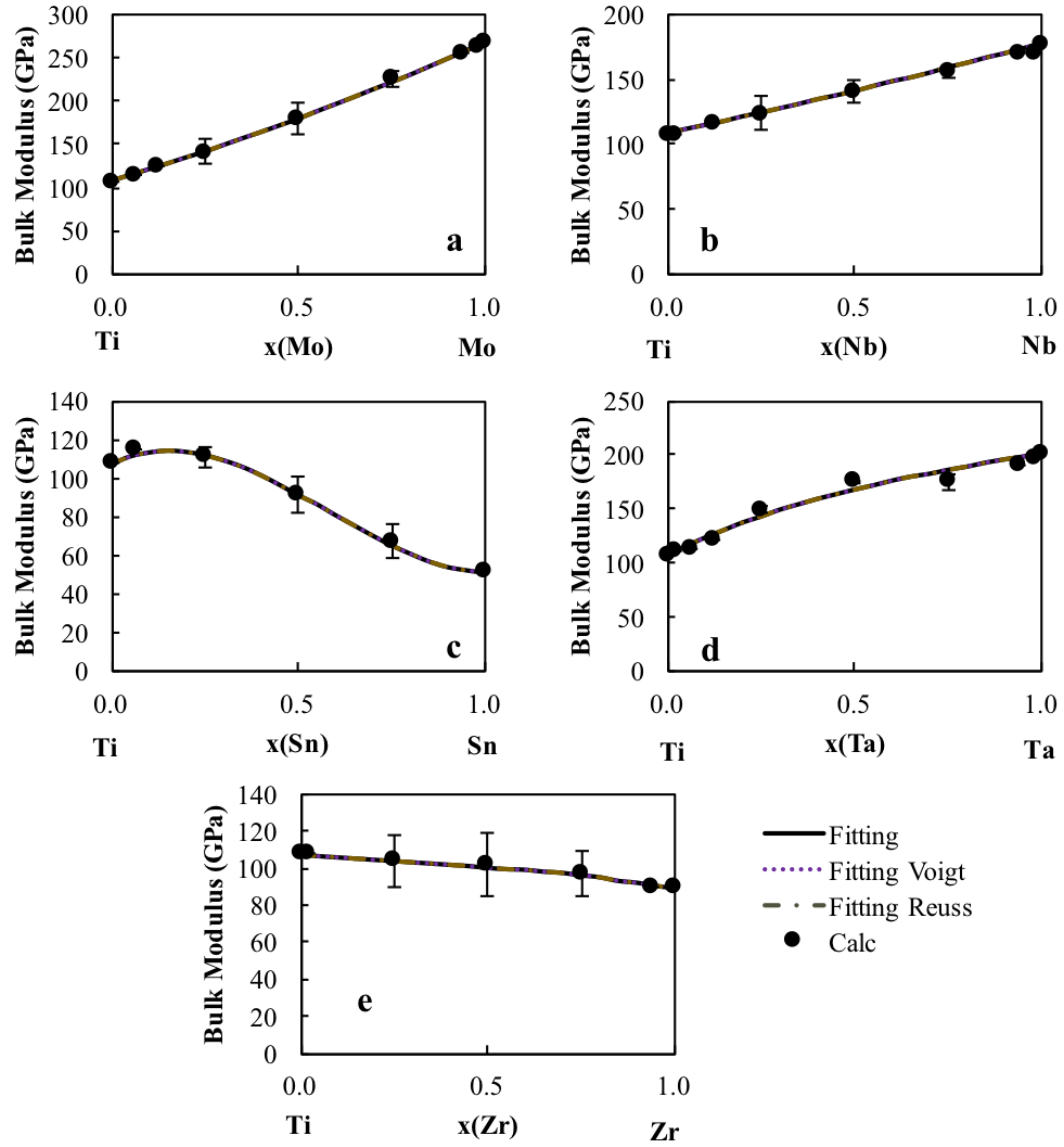


Figure 5.9. Bulk modulus B of the Ti-X binary systems. The present calculations are plotted as the filled circles with the error bars. The dotted purple line is the Voigt upper bulk modulus bound, the gold dot dashed line is the lower Reuss bulk modulus bound and the black line is the Hill bulk modulus average.

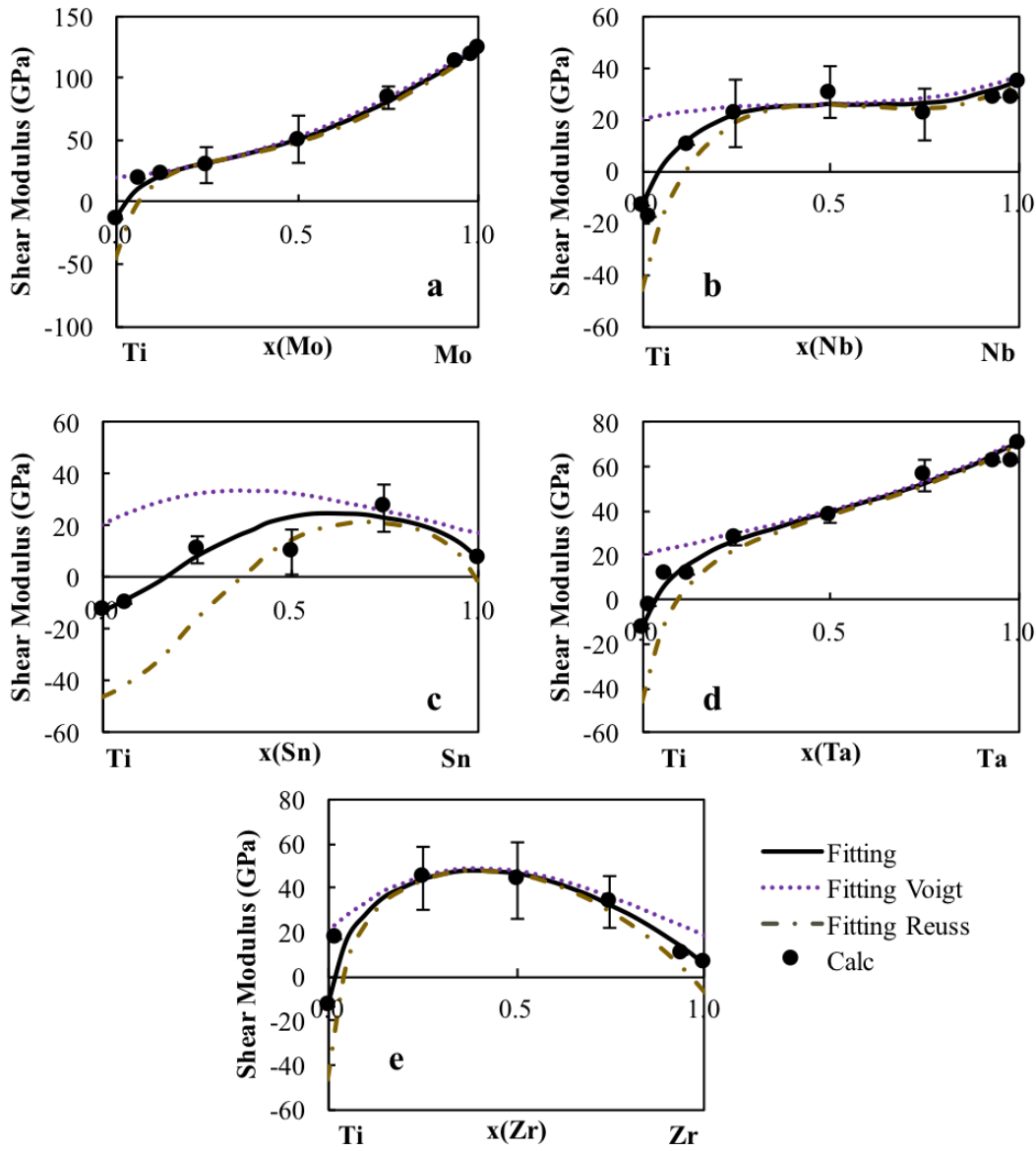


Figure 5.10. Shear modulus G of the Ti-X binary systems. The present calculations are plotted as the filled circles with the error bars. The dotted purple line is the Voigt upper shear modulus bound, the gold dot dashed line is the lower Reuss shear modulus bound and the black line is the Hill shear modulus average.

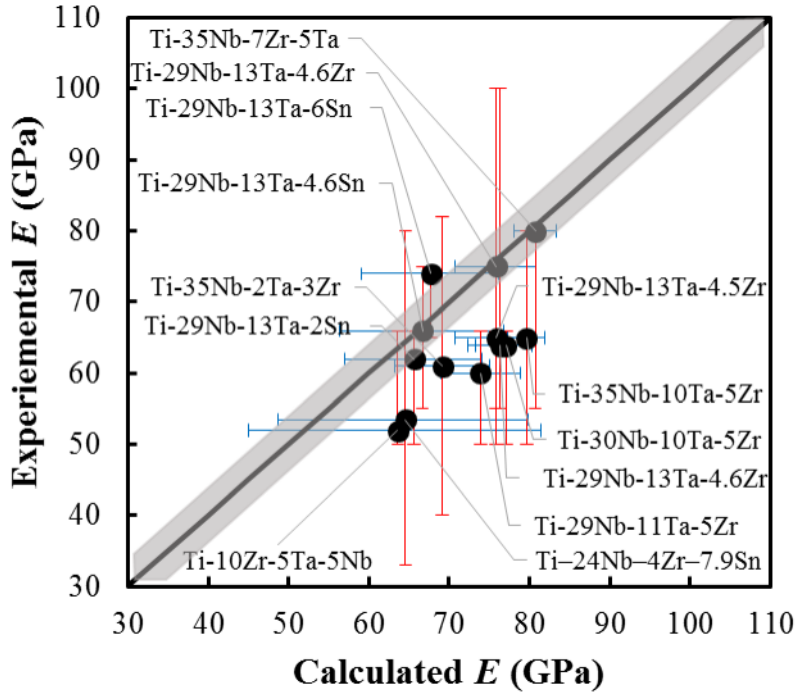


Figure 5.11. Young's moduli values of multicomponent bcc Ti alloys measured experimentally plotted against the predicted Young's moduli from the pure elements and binary interaction parameters with the black diagonal line showing the exact correlation between the experimental and calculated values. Error bars in the experiments and the bounds from Reuss and Voigt approximations are plotted as vertical and horizontal lines, respectively. The variance in the first calculations from Eq. 2.18-Eq. 2.20 was averaged and plotted as the grey region to show the variance in the first-principles calculations. More information on the alloys is in Table 5.5 [37–39]

Appendix A | Ti-Mo-Nb-Ta-Zr Database

```
$*****  
$ The definition of the pure elements, vacancy and species  
$-----  
TEMPERATURE_LIMIT 0 6000.00 !  
ELEMENT /- ELECTRON_GAS 0.0000E+00 0.0000E+00 0.0000E+00!  
ELEMENT MO BCC_A2 95.94 4589.0 28.56 !  
ELEMENT NB BCC_A2 92.9064 5220.0 36.27 !  
ELEMENT TA BCC_A2 180.9479 5681.872 41.4718 !  
ELEMENT TI HCP_A3 4.7880E+01 4.8100E+03 3.0648E+01!  
ELEMENT ZR HCP_A3 9.1224E+01 5.5663E+03 3.9181E+01!  
ELEMENT VA VACUUM 0.0 0.0 0.0 !
```

```
$*****
```

```
$ The Gibbs energies of the elements  
$ in the stable and metastable forms from SGTE  
$-----  
$-----
```

```
* TI *
```

```
$-----  
$-----
```

```
FUNCTION GBCCTI
```

```
2.98150E+02 -1272.064+134.71418*T-25.5768*T*LN(T)
```

$-6.63845 \times 10^{-4} T^2 - 2.78803 \times 10^{-7} T^3 + 7208 T^*(-1); 1.15500 \times 10^3 Y$
 $+6667.385 + 105.366379 T - 22.3771 T \ln(T) + .00121707 T^2 - 8.4534 \times 10^{-7} T^3$
 $-2002750 T^*(-1); 1.94100 \times 10^3 Y$
 $+26483.26 - 182.426471 T + 19.0900905 T \ln(T) - .02200832 T^2$
 $+1.228863 \times 10^{-6} T^3 + 1400501 T^*(-1); 4.00000 \times 10^3 N$ REF:20 !

FUNCTION GHSERTI

$2.98150 \times 10^2 - 8059.921 + 133.615208 T - 23.9933 T \ln(T)$
 $-.004777975 T^2 + 1.06716 \times 10^{-7} T^3 + 72636 T^*(-1); 9.00000 \times 10^2 Y$
 $-7811.815 + 132.988068 T - 23.9887 T \ln(T) - .0042033 T^2 - 9.0876 \times 10^{-8} T^3$
 $+42680 T^*(-1); 1.15500 \times 10^3 Y$
 $+908.837 + 66.976538 T - 14.9466 T \ln(T) - .0081465 T^2 + 2.02715 \times 10^{-7} T^3$
 $-1477660 T^*(-1); 1.94100 \times 10^3 Y$
 $-124526.786 + 638.806871 T - 87.2182461 T \ln(T) + .008204849 T^2$
 $-3.04747 \times 10^{-7} T^3 + 36699805 T^*(-1); 4.00000 \times 10^3 N$ REF:20 !

FUNCTION GFCCTI

$2.98150 \times 10^2 + 6000.1 T + GHSERTI; 6.00000 \times 10^3 N$ REF:20 !

FUNCTION GLIQTI

$2.98150 \times 10^2 + 12194.415 - 6.980938 T + GHSERTI; 1.30000 \times 10^3 Y$
 $+368610.36 - 2620.99904 T + 357.005867 T \ln(T) - .155262855 T^2$
 $+1.2254402 \times 10^{-5} T^3 - 65556856 T^*(-1) + GHSERTI; 1.94100 \times 10^3 Y$
 $+104639.72 - 340.070171 T + 40.9282461 T \ln(T) - .008204849 T^2$
 $+3.04747 \times 10^{-7} T^3 - 36699805 T^*(-1) + GHSERTI; 6.00000 \times 10^3 N$ REF:20 !

\$

\$

* MO *

\$

\$

FUNCTION GHSERMO

$298.15 - 7746.302 + 131.9197 T - 23.56414 T \ln(T)$
 $-.003443396 T^2 + 5.662834 \times 10^{-7} T^3 + 65812.39 T^*(-1)$
 $-1.309265 \times 10^{-10} T^4; 2896.00 Y$
 $-30556.41 + 283.559746 T - 42.63829 T \ln(T)$
 $-4.849315 \times 10^{-9} T^3 + 33 T^*(-9); 4000.00 N$ REF:20 !

FUNCTION GLIQMO
298.15 41831.347-14.694912*T+4.24519E-22*T**7
+GHSERMO; 2896.00 Y
34095.373-11.890046*T+4.849315E33*T**(-9)+GHSERMO;
4000.00 N REF:20 !

FUNCTION GFCCMO
298.15 15200+0.63*T+GHSERMO; 4000.00 N REF:20 !

FUNCTION GHCPMO
298.15 11550+GHSERMO; 4000.00 N REF:20 !

\$_____

\$_____

* NB *

\$_____

\$_____

FUNCTION GHSERNB
2.98140E+02 -8519.353+142.045475*T
-26.4711*T*LN(T)+2.03475E-04*T**2-3.5012E-07*T**3
+93399*T**(-1); 2.75000E+03 Y
-37669.3+271.720843*T-41.77*T*LN(T)+1.528238E+32*T**(-9);
6.00000E+03 N REF:20 !

FUNCTION GHEXTNB
2.98150E+02 -8519.35+142.048*T
-26.4711*T*LN(T)+2.03475E-04*T**2-3.50119E-07*T**3
+93398.8*T**(-1); 6.00000E+03 N REF:23 !

FUNCTION GLIQNBN
298.15 29781.555-10.816417*T
-3.06098E-23*T**7+GHSERNB; 2750.00 Y
+30169.901-10.964695*T-1.52824E32*T**(-9)+GHSERNB;
6000.00 N REF:20 !

FUNCTION GFCCNB
298.15 +13500+1.7*T+GHSERNB; 6000.00 N REF:20 !

FUNCTION GHCPNB
298.15 +10000+2.4*T+GHSERNB; 6000.00 N REF:20 !

\$
\$
* TA *

\$
\$

FUNCTION GHSERTA

2.98150E+02 -7285.889+119.139858*T
-23.7592624*T*LN(T)-.002623033*T**2+1.70109E-07*T**3
-3293*T**(-1); 1.30000E+03 Y
-22389.955+243.88676*T-41.137088*T*LN(T)+.006167572*T**2
-6.55136E-07*T**3+2429586*T**(-1); 2.50000E+03 Y
+229382.886-722.59722*T+78.5244752*T*LN(T)-.017983376*T**2
+1.95033E-07*T**3-93813648*T**(-1); 3.25800E+03 Y
-963392.734+2773.7774*T-337.227976*T*LN(T)+.039791303*T**2
-9.74251E-07*T**3+5.09949511E+08*T**(-1); 6.00000E+03 N REF:20 !

FUNCTION GFCCTA

2.98150E+02 +16000+1.7*T+GHSERTA; 6.00000E+03 N REF:20 !

FUNCTION GHCPTA

2.98150E+02 +12000+2.4*T+GHSERTA; 6.00000E+03 N REF:20 !

FUNCTION GLIQTA

2.98150E+02 +29160.975-7.578729*T+GHSERTA; 1.00000E+03 Y
+51170.228-181.121652*T+23.7872147*T*LN(T)-.009707033*T**2
+4.4449E-07*T**3-3520045*T**(-1)+GHSERTA; 1.30000E+03 Y
+66274.294-305.868555*T+41.1650403*T*LN(T)-.018497638*T**2
+1.269735E-06*T**3-5952924*T**(-1)+GHSERTA; 2.50000E+03 Y
-185498.547+660.615425*T-78.4965229*T*LN(T)+.00565331*T**2
+4.19566E-07*T**3+90290310*T**(-1)+GHSERTA; 3.29000E+03 Y
+1036069.47-2727.38037*T+320.319132*T*LN(T)-.043117795*T**2
+1.055148E-06*T**3-5.54714342E+08*T**(-1)+GHSERTA;
6.00000E+03 N REF:20 !

FUNCTION TATIB2

2.98150E+02 2500; 6.00000E+03 N REF:25 !

\$

\$
* ZR *
\$
\$
FUNCTION GLIQZR
2.98140E+02 +18147.69-9.080812*T
+1.6275E-22*T**7+GHSERZR; 2.12800E+03 Y
+17804.661-8.911574*T+1.342895E+31*T**(-9)+GHSERZR;
6.00000E+03 N REF:20 !
FUNCTION GBCCZR
2.98140E+02 -525.539+124.9457*T
-25.607406*T*LN(T)-3.40084E-04*T**2-9.729E-09*T**3
+25233*T**(-1)-7.6143E-11*T**4; 2.12800E+03 Y
-30705.955+264.284163*T-42.144*T*LN(T)+1.276058E+32*T**(-9);
6.00000E+03 N REF:20 !
FUNCTION GHSERZR
1.30000E+02 -7827.595+125.64905*T
-24.1618*T*LN(T)-.00437791*T**2+34971*T**(-1); 2.12800E+03 Y
-26085.921+262.724183*T-42.144*T*LN(T)-1.342895E+31*T**(-9);
6.00000E+03 N REF:20 !
\$
FUNCTION UN_ASS 298.15 0; 300 N !
\$

TYPE_DEFINITION % SEQ * !
TYPE_DEFINITION G SEQ * !
DEFINE_SYSTEM_DEFAULT SPECIE 5 !
DEFAULT_COMMAND DEF_SYS_ELEMENT VA !
\$

\$

PHASE LIQUID % 1 1.0 !

CONSTITUENT LIQUID :MO,TA,NB,TI,ZR: !

PARAMETER G(LIQUID, TI;0)
298.15 GLIQTI; 6000.00 N REF:20 !
PARAMETER G(LIQUID, MO;0)
298.15 GLIQMO; 6000.00 N REF:20 !
PARAMETER G(LIQUID, NB;0)
298.15 GLIQNB; 6000.00 N REF:20
PARAMETER G(LIQUID, TA;0)
298.15 GLIQT A; 6000.00 N REF:20 !
PARAMETER G(LIQUID, ZR;0)
298.15 +GLIQZR; 6000.00 N REF:20 !
PARAMETER G(LIQUID, MO, TI;0)
298.15 -9000.0+2*T; 6000.00 N REF:25 !
PARAMETER G(LIQUID, NB, TI;0)
298.15 +7406.1; 6000.00 N REF:23 !
PARAMETER G(LIQUID, TA, TI;0)
298.15 +1000; 6000.00 N REF:25 !
PARAMETER G(LIQUID, TA, TI;1)
298.15 -7000; 6000.00 N REF:25 !
PARAMETER G(LIQUID, TI, ZR;0)
298.15 -967.66; 6000.00 N REF:22 !
PARAMETER G(LIQUID, MO, NB;0) *
298.15 15253.7; 6000.00 N REF:21 !
PARAMETER G(LIQUID, MO, NB;1)
298.15 10594.2; 6000.00 N REF:21 !
PARAMETER G(LIQUID, MO, TA;0)
298.15 13978.9; 6000.00 N REF:21 !
PARAMETER G(LIQUID, MO, TA;1)
298.15 577.5; 6000.00 N REF:21 !
PARAMETER G(LIQUID, MO, ZR;0)
298.15 -24055.120+8.146158*T; 6000.00 N REF:26 !
PARAMETER G(LIQUID, MO, ZR;1)

298.15 -5132.1665+4.8041224*T; 6000.00 N REF:26 !

PARAMETER G(LIQUID,NB,TA;0)

298.15 0; 6000.00 N REF:21 !

PARAMETER G(LIQUID,NB,ZR;0)

298.15 10311; 6000.00 N REF:28 !

PARAMETER G(LIQUID,NB,ZR;1)

298.15 6709; 6000.00 N REF:28 !

PARAMETER G(LIQUID,TA,ZR;0)

298.15 13832.1; 6000.00 N REF:27 !

PARAMETER G(LIQUID,TA,ZR;1)

298.15 -7150; 6000.00 N REF:27 !

\$

PHASE BCC_A2 % 2 1 3 !

CONSTITUENT BCC_A2 :MO,TA,NB,TI,ZR:VA: !

PARAMETER G(BCC_A2,TI:VA;0)

298.15 +GBCCTI; 6000.0 N REF:20 !

PARAMETER G(BCC_A2,MO:VA;0)

298.15 +GHSERMO; 6000.00 N REF:20 !

PARAMETER G(BCC_A2,NB:VA;0)

298.15 +GHSERNB; 6000.00 N REF:20 !

PARAMETER G(BCC_A2,TA:VA;0)

298.15 +GHSERTA; 6000.00 N REF:20 !

PARAMETER G(BCC_A2,ZR:VA;0)

298.15 +GBCCZR; 6000.00 N REF:20 !

PARAMETER G(BCC_A2,MO,TI:VA;0)

298.15 2000.0; 6000.00 N REF:25 !

PARAMETER G(BCC_A2,MO,TI:VA;1)

298.15 -2000.0; 6000.00 N REF:25 !

PARAMETER G(BCC_A2,NB,TI:VA;0)

298.15 +13045.3; 6000.00 N REF:23 !

PARAMETER G(BCC_A2,TA,TI:VA;0)

298.15 12000; 6000.00 N REF:25 !

PARAMETER G(BCC_A2,TA,TI:VA;1)
298.15 -2500; 6000.00 N REF:25 !

PARAMETER G(BCC_A2,TI,ZR:VA;0)
298.15 -4346.16+5.48903*T; 6000.00 N REF:22 !

PARAMETER G(BCC_A2,MO,NB:VA;0)
298.15 -68202.6+29.85596*T; 6000.00 N REF:21 !

PARAMETER G(BCC_A2,MO,NB:VA;1)
298.15 8201.3; 6000.00 N REF:21 !

PARAMETER G(BCC_A2,MO,TA:VA;0)
298.15 -75129.2+30*T; 6000.00 N REF:21 !

PARAMETER G(BCC_A2,MO,TA:VA;1)
298.15 6039.24; 6000.00 N REF:21 !

PARAMETER G(BCC_A2,MO,ZR:VA;0)
298.15 +17935.985+3.102*T; 6000.00 N REF:26 !

PARAMETER G(BCC_A2,MO,ZR:VA;1)
298.15 -990.9911+4.299*T; 6000.00 N REF:26 !

PARAMETER G(BCC_A2,NB,TA:VA;0)
298.15 1298.02870; 6000.00 N REF:21 !

PARAMETER G(BCC_A2,NB,ZR:VA;0)
298.15 +15911+3.35*T; 6000.00 N REF:28 !

PARAMETER G(BCC_A2,NB,ZR:VA;1)
298.15 +3919-1.091*T; 6000.00 N REF:28 !

PARAMETER G(BCC_A2,ZR,TA:VA;0)
298.15 29499.6+2.6723*T; 6000.00 N REF:27 !

PARAMETER G(BCC_A2,ZR,TA:VA;1)
298.15 -4396.2+4.4302*T; 6000.00 N REF:27 !

PARAMETER G(BCC_A2,ZR,TA:VA;2)
298.15 -6353.3+4.9066*T; 6000.00 N REF:27 !

PARAMETER G(BCC_A2,MO,TA,TI:VA;0) 298.15 0; 6000.00 N !

PARAMETER G(BCC_A2,MO,TA,TI:VA;1) 298.15 0; 6000.00 N !

PARAMETER G(BCC_A2,MO,TA,TI:VA;2)
298.15 -1.5473118E+05; 6000.00 N !

PARAMETER G(BCC_A2,NB,TA,TI:VA;0)

2.98150E+02 -1.3660332E+05; 6.00000E+03 N !
PARAMETER G(BCC_A2,NB,TA,TI:VA;1)
2.98150E+02 -1.3660269E+05; 6.00000E+03 N !
PARAMETER G(BCC_A2,NB,TA,TI:VA;2)
2.98150E+02 0; 6.00000E+03 N !
\$
PHASE HCP_A3 % 2 1 .5 !
CONSTITUENT HCP_A3 :NB,TI%,ZR,TA,MO : VA% : !

PARAMETER G(HCP_A3,TA:VA;0)
298.15 +GHSERTI; 4000.00 N REF:20 !
PARAMETER G(HCP_A3,MO:VA;0)
298.15 +GHCPMO; 5000.00 N REF:20 !
PARAMETER G(HCP_A3,NB:VA;0)
298.15 +GHCPNB; 6000.00 N REF:20 !
PARAMETER G(HCP_A3,TA:VA;0)
298.15 +GHCPTA; 6000.00 N REF:20 !
PARAMETER G(HCP_A3,ZR:VA;0)
298.15 +GHSERZR; 6000.00 N REF:20 !
PARAMETER G(HCP_A3,MO,TI:VA;0)
298.15 22760-6*T; 6000.00 N REF:25 !
PARAMETER G(HCP_A3,NB,TI:VA;0)
298.15 +11742.4; 6000.00 N REF:23 !
PARAMETER G(HCP_A3,TA,TI:VA;0)
298.15 8500; 6000.00 N REF:25 !
PARAMETER G(HCP_A3,TI,ZR:VA;0)
298.15 +5133.02; 6000.00 N REF:22 !
PARAMETER G(HCP_A3,MO,ZR:VA;0)
298.15 +26753.79+4.556*T; 6000.00 N REF:26 !
PARAMETER G(HCP_A3,NB,ZR:VA;0)
298.15 24411; 6000.00 N REF:28 !
PARAMETER G(HCP_A3,ZR,TA:VA;0)
298.15 +30051.7; 6000.00 N REF:27 !

\$
TYPE_DEFINITION * GES A_P_D FCC_A1 MAGNETIC -3.0 2.80000E-01 !
PHASE FCC_A1 %* 2 1 1 !
CONSTITUENT FCC_A1 :MO,TA,ZR,NB : VA% : !

PARAMETER G(FCC_A1,TA:VA;0)
298.15 +GFCCTI; 4000.00 N REF:20 !
PARAMETER G(FCC_A1,MO:VA;0)
298.15 +GFCCMO; 5000.00 N REF:20 !
PARAMETER G(FCC_A1,NB:VA;0)
298.15 +GFCCNB; 6000.00 N REF:20 !
PARAMETER G(FCC_A1,TA:VA;0)
298.15 +GFCCTA; 6000.00 N REF:20 !
PARAMETER G(FCC_A1,MO,TA:VA;0)
298.15 16500.0; 6000.00 N REF:25 !
PARAMETER G(FCC_A1,TA,TI:VA;0)
298.15 8500; 6000.00 N REF:25 !

\$
PHASE AL3M_D022 % 2 3 1 !
CONSTITUENT AL3M_D022 :TI,MO : TA,TI,MO : !

PARAMETER G(AL3M_D022,TA:TI;0)
298.15 +4*GFCCTI; 6000.00 N REF:25 !
PARAMETER G(AL3M_D022,MO:MO;0)
298.15 +4*GFCCMO; 6000.00 N REF:25 !
PARAMETER G(AL3M_D022,TI:MO;0)
298.15 GFCCMO+3.0*GFCCTI; 6000.00 N REF:25 !
PARAMETER G(AL3M_D022,MO:TI;0)
298.15 3*GFCCMO+GFCCTI; 6000.00 N REF:25 !
PARAMETER G(AL3M_D022,TA:TA;0)
298.15 +3*GFCCTI+GFCCTA; 6000.00 N REF:25 !

TYPE_DEFINITION & GES A_P_D ALM_D019 MAGNETIC -3.0 2.80000E-01 !

PHASE ALM_D019 %& 2 3 1 !

CONSTITUENT ALM_D019 :MO,TA,TI% : MO,TA,TI : !

PARAMETER G(ALM_D019, TI:TI;0)
298.15 +4.0+4.0*GHSERTI; 6000.00 N REF:25 !
PARAMETER G(ALM_D019, TA:MO;0) 298.15 0; 6000 N!
PARAMETER G(ALM_D019, MO:TA;0) 298.15 0; 6000 N!
PARAMETER G(ALM_D019, MO:MO;0)
298.15 +4.0*GHCPMO; 6000.00 N REF:25 !
PARAMETER G(ALM_D019, TA:TA;0)
298.15 +4.0*GHCPTA; 6000.00 N REF:25 !
PARAMETER G(ALM_D019, TI:MO;0)
298.15 +17072.0-4.5*T+GHCPMO+3.0*GHSERTI; 6000.00 N REF:25 !
PARAMETER G(ALM_D019, MO:TI;0)
298.15 +17072.0-4.5*T+3.0*GHCPMO+GHSERTI; 6000.00 N REF:25 !
PARAMETER G(ALM_D019, TI:TA;0)
298.15 +6376+3.0*GHSERTI+GHCPTA; 6000.00 N REF:25 !
PARAMETER G(ALM_D019, TA:TI;0)
298.15 +6376+3.0*GHCPTA+GHSERTI; 6000.00 N REF:25 !
PARAMETER G(ALM_D019, MO, TI:MO;0)
298.15 +51212-13.5*T; 6000.00 N REF:25 !
PARAMETER G(ALM_D019, MO, TI:TI;0)
298.15 +51212-13.5*T; 6000.00 N REF:25 !
PARAMETER G(ALM_D019, MO:MO, TI;0)
298.15 +5692-1.5*T; 6000.00 N REF:25 !
PARAMETER G(ALM_D019, TI:MO, TI;0)
298.15 +5692-1.5*T; 6000.00 N REF:25 !
PARAMETER G(ALM_D019, TA, TI:TA;0)
298.15 +19128; 6000.00 N REF:25 !
PARAMETER G(ALM_D019, TA, TI:TI;0)
298.15 +19128; 6000.00 N REF:25 !
PARAMETER G(ALM_D019, TA:TA, TI;0)
298.15 2128; 6000.00 N REF:25 !

```
PARAMETER G(ALM_D019, TI:TA, TI;0)
298.15 +2128; 6000.00 N REF:25 !
$-----
TYPE_DEFINITION ' GES A_P_D ALTI MAGNETIC -1.0 4.00000E-01 !
PHASE ALTI %' 2 1 1 !
CONSTITUENT ALTI :MO,TA,TI : MO,TA,TI% : !
```

```
PARAMETER G(ALTI, TI:TI;0)
298.15 +2*GFCCTI; 6000.00 N REF:25 !
PARAMETER G(ALTI, MO:MO;0)
298.15 +2*GFCCMO; 6000.00 N REF:25 !
PARAMETER G(ALTI, TA:TA;0)
298.15 +2*GFCCTA; 6000.00 N REF:25 !
PARAMETER G(ALTI, TI:MO;0)
298.15 8250+GFCCMO+GFCCTI; 6000.00 N REF:25 !
PARAMETER G(ALTI, MO:TI;0)
298.15 8250+GFCCMO+GFCCTI; 6000.00 N REF:25 !
PARAMETER G(ALTI, TI:TA;0)
298.15 +4250+GFCCTI+GFCCTA; 6000.00 N REF:25 !
PARAMETER G(ALTI, TA:TI;0)
298.15 +4250+GFCCTA+GFCCTI; 6000.00 N REF:25 !
PARAMETER G(ALTI, MO, TI:MO;0)
298.15 8250; 6000.00 N REF:25 !
PARAMETER G(ALTI, MO, TI:TI;0)
298.15 8250; 6000.00 N REF:25 !
PARAMETER G(ALTI, MO:MO, TI;0)
298.15 8250; 6000.00 N REF:25 !
PARAMETER G(ALTI, TI:MO, TI;0)
298.15 8250; 6000.00 N REF:25 !
PARAMETER G(ALTI, TA, TI:TA;0)
298.15 4250; 6000.00 N REF:25 !
PARAMETER G(ALTI, TA, TI:TI;0)
298.15 4250; 6000.00 N REF:25 !
```

PARAMETER G(ALTI,TA:TA,TI;0)
298.15 4250; 6000.00 N REF:25 !
PARAMETER G(ALTI,TI:TA,TI;0)
298.15 4250; 6000.00 N REF:25 !
\$_____

TYPE_DEFINITION) GES AMEND_PHASE_DESCRIPTION
BCC_B2 DIS_PART BCC_A2,,,!
PHASE BCC_B2 %) 3 .5 .5 3 !
CONSTITUENT BCC_B2 :MO,NB,TA,TI,ZR : MO,NB,TA,TI%,ZR : VA : !

PARAMETER G(BCC_B2,MO:MO:VA;0) 298.15 0; 6000 N REF:25!
PARAMETER G(BCC_B2,TA:TA:VA;0) 298.15 0; 6000 N REF:25 !
PARAMETER G(BCC_B2,TI:TI:VA;0) 298.15 0; 6000 N REF:25 !
PARAMETER G(BCC_B2,TI:MO:VA;0)
298.15 10000.0; 6000.00 N REF:25 !
PARAMETER G(BCC_B2,MO:TI:VA;0)
298.15 10000.0; 6000.00 N REF:25 !
PARAMETER G(BCC_B2,TI:TA:VA;0)
298.15 +5000.0; 6000.00 N REF:25 !
PARAMETER G(BCC_B2,TA:TI:VA;0)
298.15 +5000.0; 6000.00 N REF:25 !
\$_____

PHASE BCT_A5 % 1 1.0 !
CONSTITUENT BCT_A5 :TI : !

PARAMETER G(BCT_A5,TI;0)
298.15 +4602.2+GHserti; 3000.00 N REF:20 !
\$_____

PHASE CBCC_A12 % 2 1 1 !
CONSTITUENT CBCC_A12 :TI : VA : !

PARAMETER G(CBCC_A12,TI:VA;0)
298.15 +4602.2+GHserti; 6000.00 N REF:20 !

\$

PHASE CUB_A13 % 2 1 1 !
CONSTITUENT CUB_A13 :TI : VA : !

PARAMETER G(CUB_A13, TI:VA;0)
298.15 +7531.2+GHserti; 6000.00 N REF:20 !

\$

PHASE DIAMOND_A4 % 1 1.0 !
CONSTITUENT DIAMOND_A4 :TI : !

PARAMETER G(DIAMOND_A4, TI;0)
298.15 +25000+GHserti; 6000.00 N REF:20 !

\$

PHASE LAVES_C14 % 2 2 1 !
CONSTITUENT LAVES_C14 :TI : TI% : !

PARAMETER G(LAVES_C14, TI:TI;0)
298.15 +15000+3*GHserti; 6000.00 N REF:20 !

\$

PHASE LAVES_C15 % 2 2 1 !
CONSTITUENT LAVES_C15 :TI,MO,ZR : TI,MO,ZR : !

PARAMETER G(LAVES_C15, TI:TI;0)

298.15 +15000+3*GHserti; 6.00000E+03 N REF:24!

PARAMETER G(LAVES_C15, MO:MO;0)

298.15 +3*GHSERMO+15000; 6000 N REF:26 !

PARAMETER G(LAVES_C15, ZR:ZR;0)

298.15 +3*GHSERZR+15000; 6000 N REF:26 !

PARAMETER G(LAVES_C15, TI:MO;0)

298.15 +GHSERMO+2*GHserti+15000; 6000 N REF:24 !

PARAMETER G(LAVES_C15, MO:TI;0)

298.15 +2*GHSERMO+GHserti+15000; 6000 N REF:24 !

PARAMETER G(LAVES_C15, TI:ZR;0)

298.15 +2*GHSERTI+GHSERZR+9000; 6000 N REF:24 !
PARAMETER G(LAVES_C15,ZR:TI;0)
298.15 +GHSERTI+2*GHSERZR+15000; 6000 N REF:24 !
PARAMETER G(LAVES_C15,MO:ZR;0)
298.15 +2*GHSERMO+GHSERZR-21734.78+0.1441789*T; 6000 N REF:26 !
PARAMETER G(LAVES_C15,ZR:MO;0)
298.15 +GHSERMO+2*GHSERZR+21734.78-0.1441789*T; 6000 N REF:26 !
PARAMETER G(LAVES_C15,MO:MO,ZR;0) 298.15 +60000; 6000 N REF:26 !
PARAMETER G(LAVES_C15,ZR:MO,ZR;0) 298.15 +60000; 6000 N REF:26 !
PARAMETER G(LAVES_C15,MO,ZR:MO;0) 298.15 +100000; 6000 N REF:26 !
PARAMETER G(LAVES_C15,MO,ZR:ZR;0) 298.15 +100000; 6000 N REF:26 !
PARAMETER G(LAVES_C15,TI:MO,ZR;0) 298.15 +60000; 6000 N REF:27 !
PARAMETER G(LAVES_C15,MO,ZR:TI;0) 298.15 +100000; 6000 N REF:27 !
\$

PHASE OMEGA % 2 1 .5 !
CONSTITUENT OMEGA :NB,TI% : VA% : !

PARAMETER G(OMEGA,ZR;0)
298.15 -8878.082+144.432234*T
-26.8556*T*LN(T)-.002799446*T**2+38376*T**(-1); 2128 Y
-29500.524+265.290858*T-42.144*T*LN(T)
+7.17445E+31*T**(-9); 6000 N REF:20 !
PARAMETER G(OMEGA,TI:VA;0)
298.15 1886.7-0.15161*T+GHSERTI; 4.00000E+03 N REF:23 !
PARAMETER G(OMEGA,NB:VA;0)
2.98150E+02 15000+2.4*T++GHSERNB; 6.00000E+03 N REF:23 !
PARAMETER G(OMEGA,NB,TI:VA;0)
298.15 -3775.9; 6000.00 N REF:23 !
\$

PHASE SI3TI5 % 3 2 3 3 !
CONSTITUENT SI3TI5 :TI : TI : TI : !

PARAMETER G(SI3TI5,TI:TI:TI;0)

298.15 +40000+20*T+8*GHSERTI; 6000.00 N REF:20 !

\$-----

PHASE SNTI3 % 2 1 3 !

CONSTITUENT SNTI3 :TI : TI% : !

PARAMETER G(SNTI3,TI:TI;0)

298.15 +4*GHSERTI+4; 6000.00 N REF:20 !

\$-----

PHASE ORTHORHOMBIC_A20 % 1 1.0 !

CONSTITUENT ORTHORHOMBIC_A20 :ZR : !

PARAMETER G(ORTHORHOMBIC_A20,ZR;0)

298.15 +4474.461+124.9457*T

-25.607406*T*LN(T)-3.40084E-04*T**2-9.729E-09*T**3

+25233*T**(-1)-7.6143E-11*T**4; 2128 Y

-25705.955+264.284163*T-42.144*T*LN(T)

+1.276058E+32*T**(-9); 6000 N REF:20 !

\$-----

PHASE TETRAGONAL_U % 1 1.0 !

CONSTITUENT TETRAGONAL_U :ZR : !

PARAMETER G(TETRAGONAL_U,ZR;0)

298.15 +4474.461+124.9457*T

-25.607406*T*LN(T)-3.40084E-04*T**2-9.729E-09*T**3

+25233*T**(-1)-7.6143E-11*T**4; 2128 Y

-25705.955+264.284163*T-42.144*T*LN(T)

+1.276058E+32*T**(-9); 6000 N REF:20 !

\$-----

DATABASE_INFO 'FOR THE TI_MO_NB_TA_ZR SYSTEM' !

LIST_OF_REFERENCES

NUMBER SOURCE

20 'A.T. Dinsdale, SGTE Data for Pure Elements, CALPHAD.

-
- 15 (1991) 317-425.'
- 21 'W. Xiong, Y. Du, Y. Liu, B.Y. Huang, H.H. Xu, H.L. Chen, et al., Thermodynamic assessment of the Mo-Nb-Ta system, Calphad-Computer Coupling Phase Diagrams Thermochem. 28 (2004) 133-140.'
- 22 'K.C.H. Kumar, P. Wollants, L. Delaey, Thermodynamic assessment of the Ti-Zr system and calculation of the Nb-Ti-Zr phase-diagram, J. Alloys Compd. 206 (1994) 121-127.'
- 23 'Y.L. Zhang, H.S. Liu, Z.P. Jin, Thermodynamic assessment of the Nb-Ti system, Calphad-Computer Coupling Phase Diagrams Thermochem. 25 (2001) 305-317.'
- 24 'S. Kar, D.M. Lipkin, A CALPHAD-based phase equilibrium model of Mo-Ti-Zr-C, in: TMS 2008 Annu. Meet. Suppl. Proceedings, Vol 2 Mater. Charact. Comput. Model., Minerals, Metals & Materials Soc, Warrendale, 2008: pp. 237-243.'
- 25 'I. Ansara, A.T. Dinsdale, M.H. Rand, COST 507: thermochemical database for light metal alloys, European Communities, Brussels and Luxembourg, 1998.'
- 26 'R.J. Perez, B. Sundman, Thermodynamic assessment of the Mo-Zr binary phase diagram, Calphad-Computer Coupling Phase Diagrams Thermochem. 27 (2003) 253-262.'
- 27 'A.F. Guillermet, Phase-diagram and thermochemical properties of the Zr-Ta system - an assessment based on Gibbs energy modeling, J. Alloys Compd. 226 (1995) 174-184.'
- 28 'A.F. Guillermet, Thermodynamic analysis of the stable phases in the Zr-Nb system and calculation of the phase-diagram, Zeitschrift Fur Met. 82 (1991) 478-487.'
- !
-

Appendix B |

Sn-Ta Database

```
$*****  
$ The definition of the pure elements, vacancy and species  
$-----  
ELEMENT /- ELECTRON_GAS 0.0000E+00 0.0000E+00 0.0000E+00!  
ELEMENT VA VACUUM 0.0000E+00 0.0000E+00 0.0000E+00!  
ELEMENT SN BCT_A5 1.1871E+02 6.3220E+03 5.1195E+01!  
ELEMENT TA BCC_A2 1.8095E+02 5.6819E+03 4.1472E+01!
```

```
$*****
```

```
$ The Gibbs energies of the elements  
$ in the stable and metastable forms from SGTE  
$-----  
$-----
```

* TA *

```
$-----  
$-----
```

FUNCTION GHSERTA

```
298.15 -7285.889+119.139857*T-23.7592624*T*LN(T)  
.002623033*T**2+1.70109E-07*T**3-3293*T**(-1); 1300 Y  
-22389.955+243.88676*T-41.137088*T*LN(T)+.006167572*T**2  
-6.55136E-07*T**3+2429586*T**(-1); 2500 Y  
+229382.886-722.59722*T+78.5244752*T*LN(T)-.017983376*T**2
```

+1.95033E-07*T**3-93813648*T**(-1); 3290 Y
-1042384.01+2985.49125*T-362.159132*T*LN(T)+.043117795*T**2
-1.055148E-06*T**3+5.54714342E+08*T**(-1); 6000 N REF20 !

FUNCTION GFCCTA

298.15 +8714.111+120.839857*T-23.7592624*T*LN(T)
.002623033*T**2+1.70109E-07*T**3-3293*T**(-1); 1300 Y
-6389.955+245.58676*T-41.137088*T*LN(T)+.006167572*T**2
-6.55136E-07*T**3+2429586*T**(-1); 2500 Y
+245382.886-720.89722*T+78.5244752*T*LN(T)-.017983376*T**2
+1.95033E-07*T**3-93813648*T**(-1); 3290 Y
-1026384.01+2987.19125*T-362.159132*T*LN(T)+.043117795*T**2
-1.055148E-06*T**3+5.54714342E+08*T**(-1); 6000 N REF20 !

FUNCTION GHCPTA

298.15 +4714.111+121.539857*T-23.7592624*T*LN(T)
.002623033*T**2+1.70109E-07*T**3-3293*T**(-1); 1300 Y
-10389.955+246.28676*T-41.137088*T*LN(T)+.006167572*T**2
-6.55136E-07*T**3+2429586*T**(-1); 2500 Y
+241382.886-720.19722*T+78.5244752*T*LN(T)-.017983376*T**2
+1.95033E-07*T**3-93813648*T**(-1); 3290 Y
-1030384.01+2987.89125*T-362.159132*T*LN(T)+.043117795*T**2
-1.055148E-06*T**3+5.54714342E+08*T**(-1); 6000 N REF20 !

FUNCTION GLIQTA

298.15 +21875.086+111.561128*T-23.7592624*T*LN(T)
.002623033*T**2+1.70109E-07*T**3-3293*T**(-1); 1000 Y
+43884.339-61.981795*T+.0279523*T*LN(T)-.012330066*T**2
+6.14599E-07*T**3-3523338*T**(-1); 3290 Y
-6314.543+258.110873*T-41.84*T*LN(T); 6000 N REF20 !

\$_____

\$_____

* SN *

\$_____

\$_____

FUNCTION GHSERSN

100 -7958.517+122.765451*T-25.858*T*LN(T)
+5.1185E-04*T**2-3.192767E-06*T**3+18440*T**(-1); 250 Y
-5855.135+65.443315*T-15.961*T*LN(T)-.0188702*T**2+3.121167E-06*T**3
-61960*T**(-1); 505.08 Y
+2524.724+4.005269*T-8.2590486*T*LN(T)-.016814429*T**2
+2.623131E-06*T**3-1081244*T**(-1)-1.2307E+25*T**(-9); 800 Y
-8256.959+138.99688*T-28.4512*T*LN(T)-1.2307E+25*T**(-9); 3000 N REF20 !

FUNCTION GBCCSN

100 -3558.517+116.765451*T-25.858*T*LN(T)
+5.1185E-04*T**2-3.192767E-06*T**3+18440*T**(-1); 250 Y
-1455.135+59.443315*T-15.961*T*LN(T)-.0188702*T**2+3.121167E-06*T**3
-61960*T**(-1); 505.08 Y
+6924.724-1.994731*T-8.2590486*T*LN(T)-.016814429*T**2
+2.623131E-06*T**3-1081244*T**(-1)-1.2307E+25*T**(-9); 800 Y
-3856.959+132.99688*T-28.4512*T*LN(T)-1.2307E+25*T**(-9); 3000 N REF20 !

FUNCTION GA12SN

100 -5958.517+122.765451*T-25.858*T*LN(T)
+5.1185E-04*T**2-3.192767E-06*T**3+18440*T**(-1); 250 Y
-3855.135+65.443315*T-15.961*T*LN(T)-.0188702*T**2+3.121167E-06*T**3
-61960*T**(-1); 505.08 Y+4524.724+4.005269*T-8.2590486*T*LN(T)
-.016814429*T**2+2.623131E-06*T**3-1081244*T**(-1)-1.2307E+25*T**(-9); 800 Y
-6256.959+138.99688*T-28.4512*T*LN(T)-1.2307E+25*T**(-9); 3000 N REF20 !

FUNCTION GA13SN

100 -5958.517+122.765451*T-25.858*T*LN(T)
+5.1185E-04*T**2-3.192767E-06*T**3+18440*T**(-1); 250 Y
-3855.135+65.443315*T-15.961*T*LN(T)-.0188702*T**2+3.121167E-06*T**3
-61960*T**(-1); 505.08 Y
+4524.724+4.005269*T-8.2590486*T*LN(T)-.016814429*T**2
+2.623131E-06*T**3-1081244*T**(-1)-1.2307E+25*T**(-9); 800 Y
-6256.959+138.99688*T-28.4512*T*LN(T)-1.2307E+25*T**(-9); 3000 N REF20 !

FUNCTION GDIAMOND

100 -9579.608+114.007785*T-22.972*T*LN(T)-.00813975*T**2
+2.7288E-06*T**3+25615*T**(-1); 298.15 Y

-9063.001+104.84654*T-21.5750771*T*LN(T)-.008575282*T**2
+1.784447E-06*T**3-2544*T**(-1); 800 Y
-10909.351+147.396535*T-28.4512*T*LN(T); 3000 N REF20 !

FUNCTION GFCCSN
298.15 -345.135+56.983315*T-15.961*T*LN(T)-.0188702*T**2
+3.121167E-06*T**3-61960*T**(-1); 505.08 Y
+8034.724-4.454731*T-8.2590486*T*LN(T)-.016814429*T**2
+2.623131E-06*T**3-1081244*T**(-1)-1.2307E+25*T**(-9); 800 Y
-2746.959+130.53688*T-28.4512*T*LN(T)-1.2307E+25*T**(-9); 3000 N REF20 !

FUNCTION GHCPSN
298.15 -1955.135+57.797315*T-15.961*T*LN(T)
-.0188702*T**2+3.121167E-06*T**3-61960*T**(-1); 505.08 Y
+6424.724-3.640731*T-8.2590486*T*LN(T)-.016814429*T**2
+2.623131E-06*T**3-1081244*T**(-1)-1.2307E+25*T**(-9); 800 Y
-4356.959+131.35088*T-28.4512*T*LN(T)-1.2307E+25*T**(-9); 3000 N REF20 !

FUNCTION GHCPZN_S
298.15 -1950.135+57.797315*T-15.961*T*LN(T)
-.0188702*T**2+3.121167E-06*T**3-61960*T**(-1); 505.08 Y
+6429.724-3.640731*T-8.2590486*T*LN(T)-.016814429*T**2
+2.623131E-06*T**3-1081244*T**(-1)-1.2307E+25*T**(-9); 800 Y
-4351.959+131.35088*T-28.4512*T*LN(T)-1.2307E+25*T**(-9); 3000 N REF20 !

FUNCTION GLIQSN
100 -855.425+108.677684*T-25.858*T*LN(T)+5.1185E-04*T**2
-3.192767E-06*T**3+18440*T**(-1)+1.47031E-18*T**7; 250 Y
+1247.957+51.355548*T-15.961*T*LN(T)-.0188702*T**2+3.121167E-06*T**3
-61960*T**(-1)+1.47031E-18*T**7; 505.08 Y
+9496.31-9.809114*T-8.2590486*T*LN(T)-.016814429*T**2
+2.623131E-06*T**3-1081244*T**(-1); 800 Y
-1285.372+125.182498*T-28.4512*T*LN(T); 3000 N REF20 !

FUNCTION GA7SN
100 -5923.517+122.765451*T-25.858*T*LN(T)
+5.1185E-04*T**2-3.192767E-06*T**3+18440*T**(-1); 250 Y
-3820.135+65.443315*T-15.961*T*LN(T)-.0188702*T**2+3.121167E-06*T**3

-61960*T**(-1); 505.08 Y
+4559.724+4.005269*T-8.2590486*T*LN(T)-.016814429*T**2
+2.623131E-06*T**3-1081244*T**(-1)-1.2307E+25*T**(-9); 800 Y
-6221.959+138.99688*T-28.4512*T*LN(T)-1.2307E+25*T**(-9); 3000 N REF20 !
FUNCTION GA6SN
298.15 -468.135+57.181195*T-15.961*T*LN(T)-.0188702*T**2
+3.121167E-06*T**3-61960*T**(-1); 505.08 Y
+7911.724-4.256851*T-8.2590486*T*LN(T)-.016814429*T**2
+2.623131E-06*T**3-1081244*T**(-1)-1.2307E+25*T**(-9); 800 Y
-2869.959+130.73476*T-28.4512*T*LN(T)-1.2307E+25*T**(-9); 3000 N REF20 !
\$

FUNCTION UN_ASS 298.15 +0.0; 300 N !

\$

TYPE_DEFINITION % SEQ *!

DEFINE_SYSTEM_DEFAULT ELEMENT 2 !

DEFAULT_COMMAND DEF_SYS_ELEMENT VA /- !

\$

\$

TYPE_DEFINITION & GES A_P_D BCC_A2 MAGNETIC -1.0 4.00000E-01 !

PHASE BCC_A2 %& 2 1 3 !

CONSTITUENT BCC_A2 :SN,TA : VA : !

PARAMETER G(BCC_A2,SN:VA;0)

100 +GBCCSN; 3000 N REF20 !

PARAMETER G(BCC_A2,TA:VA;0)

298.15 +GHSERTA; 6000 N REF20 !

PARAMETER G(BCC_A2,SN,TA:VA;0)

298.15 7.0451375E+04; 6000 N !

PARAMETER G(BCC_A2,SN,TA:VA;1)

298.15 1.1223739E+05; 6000 N !

\$

PHASE BCT_A5 % 1 1.0 !

CONSTITUENT BCT_A5 :SN : !

PARAMETER G(BCT_A5,SN;0)

100 +GHSERSN; 3000 N REF20 !

\$

TYPE_DEFINITION ' GES A_P_D CBCC_A12 MAGNETIC -3.0 2.80000E-01 !
 PHASE CBCC_A12 %' 2 1 1 !
 CONSTITUENT CBCC_A12 :SN : VA : !

PARAMETER G(CBCC_A12,SN:VA;0) 100 +GA12SN; 3000 N REF20 !

\$

PHASE CUB_A13 % 2 1 1 !
 CONSTITUENT CUB_A13 :SN : VA : !

PARAMETER G(CUB_A13,SN:VA;0) 100 +GA13SN; 3000 N REF20 !

\$

PHASE DIAMOND_A4 % 1 1.0 !
 CONSTITUENT DIAMOND_A4 :SN : !

PARAMETER G(DIAMOND_A4,SN;0) 100 +GDIAMOND; 3000 N REF20 !

\$

TYPE_DEFINITION (GES A_P_D FCC_A1 MAGNETIC -3.0 2.80000E-01 !
 PHASE FCC_A1 %(2 1 1 !
 CONSTITUENT FCC_A1 :SN,TA : VA : !

PARAMETER G(FCC_A1,SN:VA;0) 298.15 +GFCCSN; 3000 N REF20 !
 PARAMETER G(FCC_A1,TA:VA;0) 298.15 +GFCCTA; 6000 N REF20 !

\$

TYPE_DEFINITION) GES A_P_D HCP_A3 MAGNETIC -3.0 2.80000E-01 !
 PHASE HCP_A3 %) 2 1 .5 !
 CONSTITUENT HCP_A3 :SN,TA : VA : !

PARAMETER G(HCP_A3,SN:VA;0) 298.15 +GHCPSEN; 3000 N REF20 !
 PARAMETER G(HCP_A3,TA:VA;0) 298.15 +GHCPATA; 6000 N REF20 !

\$

PHASE HCP_ZN % 2 1 .5 !
 CONSTITUENT HCP_ZN :SN : VA : !

PARAMETER G(HCP_ZN,SN:VA;0) 298.15 +GHCPZN_S; 3000 N REF20 !
\$-----

PHASE LIQUID % 1 1.0 !
CONSTITUENT LIQUID :SN,TA : !

PARAMETER G(LIQUID,SN;0) 100 +GLIQSN; 3000 N REF20 !
PARAMETER G(LIQUID,TA;0) 298.15 +GLIQT; 6000 N REF20 !
PARAMETER G(LIQUID,SN,TA;0) 298.15 -1.7117919E+04; 6000 N !
\$-----

PHASE RHOMBOHEDRAL_A7 % 1 1.0 !
CONSTITUENT RHOMBOHEDRAL_A7 :SN : !

PARAMETER G(RHOMBOHEDRAL_A7,SN;0) 100 +GA7SN; 3000 N REF20 !
\$-----

PHASE TA3SN % 2 3 1 !
CONSTITUENT TA3SN :TA : SN : !

PARAMETER G(TA3SN,TA:SN;0)
298.15 -68843.951-6.00E+00*T+3*GHSERTA+GHSERSN; 3000 N !
\$-----

PHASE TASN2 % 2 1 2 !
CONSTITUENT TASN2 :TA : SN : !

PARAMETER G(TASN2,TA:SN;0)
298.15 -29678.180-4.202*T+GHSERTA+2*GHSERSN; 3000 N !
\$-----

PHASE TETRAGONAL_A6 % 1 1.0 !
CONSTITUENT TETRAGONAL_A6 :SN : !

PARAMETER G(TETRAGONAL_A6,SN;0) 298.15 +GA6SN; 3000 N REF20 !
\$-----

\$*****

LIST_OF_REFERENCES

NUMBER SOURCE

20 'A.T. Dinsdale, SGTE Data for Pure Elements,
CALPHAD.15 (1991) 317-425. '

!

Appendix C | Calculation and Fitting Details

C.1 Calculation Details for Chapter 3, 5, and 6

As discussed in each chapter the Monkhorst-Pack scheme is used for Brillouin zone sampling [61, 91]. The k-points grid used for each calculation done in chapter 3, 5 and 6 are listed in the table. The k-points grids are listed as AxAxA. In some cases the automated k-point mesh generator in VASP was used and the length of the subdivisions specified are specified as number such as 50.

Table C.1: The k-points grids used for each calculation done in chapter 3, 5 and 6.

Structure	Type of Calc	relaxation k-points
hcp-Ti	Elemental	30
bcc-Ti	Elemental	50
bcc-Mo	Elemental	50
bcc-Nb	Elemental	50
bcc-Ta	Elemental	50
hcp-Zr	Elemental	30
bcc-Zr	Elemental	4x4x4
bcc-Ti ₁₅ Mo	Dilute	5x5x5
bcc-Ti ₇ Mo	Dilute	4x4x4
bcc-Ti ₇₅ Mo ₂₅	SQS	4x4x4
bcc-Ti ₅₀ Mo ₅₀	SQS	4x4x4
bcc-Ti ₂₅ Mo ₇₅	SQS	4x4x4
bcc-TiMo ₁₅	Dilute	80

Table C.1: The k-points grids used for each calculation done in chapter 3, 5 and 6.

Structure	Type of Calc	relaxation k-points
bcc-TiMo ₅₃	Dilute	50
bcc-Ti ₅₃ Nb	Dilute	4x4x4
bcc-Ti ₇ Nb	Dilute	4x4x4
bcc-Ti ₇₅ Nb ₂₅	SQS	4x4x4
bcc-Ti ₅₀ Nb ₅₀	SQS	4x4x4
bcc-Ti ₂₅ Nb ₇₅	SQS	4x4x4
bcc-TiNb ₁₅	Dilute	80
bcc-TiNb ₅₃	Dilute	80
bcc-Ti ₁₅ Sn	Dilute	80
bcc-Ti ₇₅ Sn ₂₅	SQS	4x4x4
bcc-Ti ₅₀ Sn ₅₀	SQS	80
bcc-Ti ₂₅ Sn ₇₅	SQS	4x4x4
bcc-Ti ₅₃ Ta	Dilute	50
bcc-Ti ₁₅ Ta	Dilute	80
bcc-Ti ₇ Ta	Dilute	80
bcc-Ti ₇₅ Ta ₂₅	SQS	80
bcc-Ti ₅₀ Ta ₅₀	SQS	80
bcc-Ti ₂₅ Ta ₇₅	SQS	4x4x4
bcc-TiTa ₁₅	Dilute	80
bcc-TiTa ₅₃	Dilute	80
bcc-Ti ₅₃ Zr	Dilute	3x3x3
bcc-Ti ₇₅ Zr ₂₅	SQS	4x4x4
bcc-Ti ₅₀ Zr ₅₀	SQS	4x4x4
bcc-Ti ₂₅ Zr ₇₅	SQS	4x4x4
bcc-TiZr ₁₅	Dilute	80
bcc-Mo ₅₀ Nb ₅₀	SQS	3x3x3
bcc-Mo ₅₀ Sn ₅₀	SQS	80
bcc-Mo ₅₀ Ta ₅₀	SQS	80
bcc-Mo ₅₀ Zr ₅₀	SQS	80
bcc-Nb ₅₀ Sn ₅₀	SQS	80
bcc-Nb ₅₀ Ta ₅₀	SQS	80

Table C.1: The k-points grids used for each calculation done in chapter 3, 5 and 6.

Structure	Type of Calc	relaxation k-points
bcc-Nb ₅₀ Zr ₅₀	SQS	80
bcc-Sn ₅₀ Ta ₅₀	SQS	80
bcc-Sn ₅₀ Zr ₅₀	SQS	80
bcc-Ta ₅₀ Zr ₅₀	SQS	80
bcc-TiMoNb	SQS	4x4x4
bcc-Ti ₂ MoNb	SQS	4x4x4
bcc-Ti ₆ MoNb	SQS	4x4x4
bcc-TiMoSn	SQS	4x4x4
bcc-Ti ₂ MoSn	SQS	4x4x4
bcc-Ti ₆ MoSn	SQS	4x4x4
bcc-TiMoTa	SQS	4x4x4
bcc-Ti ₂ MoTa	SQS	4x4x4
bcc-Ti ₆ MoTa	SQS	4x4x4
bcc-TiMoZr	SQS	4x4x4
bcc-Ti ₂ MoZr	SQS	4x4x4
bcc-Ti ₆ MoZr	SQS	4x4x4
bcc-TiNbSn	SQS	4x4x4
bcc-Ti ₂ NbSn	SQS	4x4x4
bcc-Ti ₆ NbSn	SQS	4x4x4
bcc-TiNbSn	SQS	4x4x4
bcc-Ti ₂ NbSn	SQS	4x4x4
bcc-Ti ₆ NbSn	SQS	4x4x4
bcc-TiNbTa	SQS	4x4x4
bcc-Ti ₂ NbTa	SQS	4x4x4
bcc-Ti ₆ NbTa	SQS	4x4x4
bcc-TiNbZr	SQS	4x4x4
bcc-Ti ₂ NbZr	SQS	4x4x4
bcc-Ti ₆ NbZr	SQS	4x4x4
bcc-TiNbZr	SQS	4x4x4
bcc-Ti ₂ NbZr	SQS	4x4x4
bcc-Ti ₆ NbZr	SQS	4x4x4

Table C.1: The k-points grids used for each calculation done in chapter 3, 5 and 6.

Structure	Type of Calc	relaxation k-points
bcc-TiSnTa	SQS	4x4x4
bcc-Ti ₂ SnTa	SQS	4x4x4
bcc-Ti ₆ SnTa	SQS	4x4x4
bcc-TiSnZr	SQS	4x4x4
bcc-Ti ₂ SnZr	SQS	4x4x4
bcc-Ti ₆ SnZr	SQS	4x4x4
bcc-TiTaZr	SQS	4x4x4
bcc-Ti ₂ TaZr	SQS	4x4x4
bcc-Ti ₆ TaZr	SQS	4x4x4

C.2 Fitting Code for Chapter 5 and 6

The code used in Mathematica to fit the binary and ternary interaction parameters is listed below.

```
input: n = 0, 0, 0.019, -2.81, 0.019, -2.81, 0.019, -2.81, 0.019, -2.81, 0.019, -2.81, 0.125, 4.00, 0.125, 4.00, 0.125, 4.00, 0.125, 4.00, 0.125, 4.00, 0.125, 4.00, 0.25, 8.67, 0.25, 8.67, 0.25, 8.67, 0.25, 8.67, 0.25, 8.67, 0.50, 12.00, 0.75, 1.00, 0.938, 6.42, 0.981, -0.11, 1, 0
```

```
output: 0, 0, 0.019, -2.81, 0.019, -2.81, 0.019, -2.81, 0.019, -2.81, 0.019, -2.81, 0.125, 4., 0.125, 4., 0.125, 4., 0.125, 4., 0.125, 4., 0.25, 8.67, 0.25, 8.67, 0.25, 8.67, 0.25, 8.67, 0.5, 12., 0.75, 1., 0.938, 6.42, 0.981, -0.11, 1, 0
```

```
input: gp = ListPlot[n, PlotMarkers -> □, 10, PlotStyle -> Blue] input: Fit[n, (x*(1 - x)), ((x*(1 - x))^(x - (1 - x))), x] (For a two parameter fit) input: Fit[n, (x*(1 - x)), x] (For a one parameter fit) input: Plot[%, x, 0, 1, PlotRange -> -100, 100] input: Show[%, gp]
```

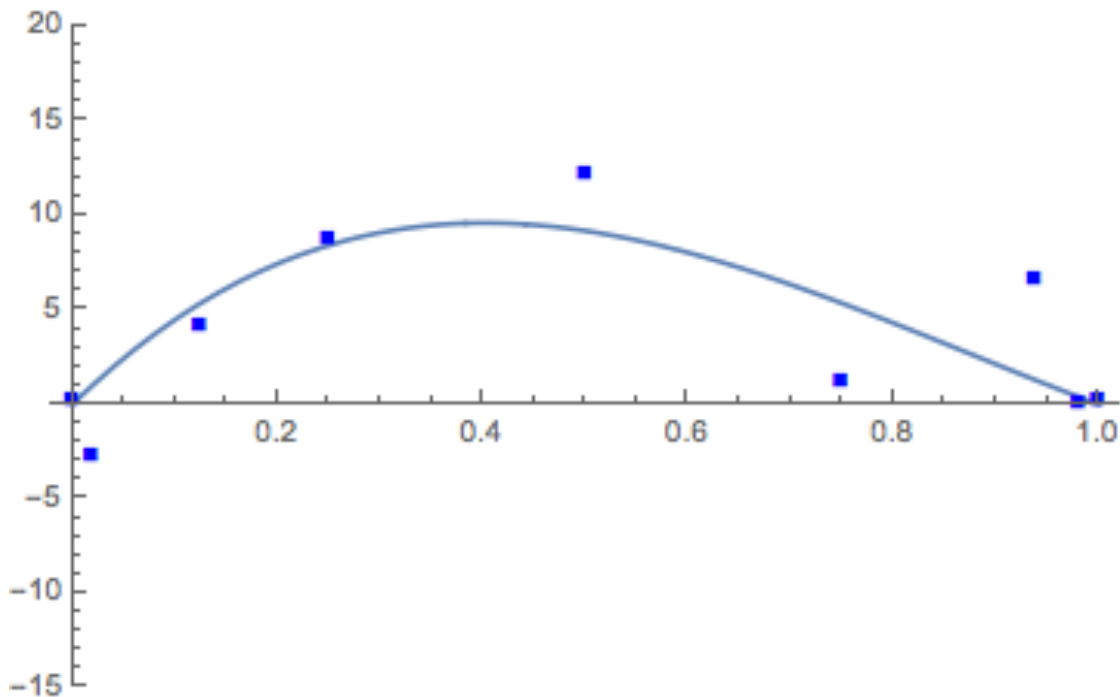


Figure C.1.

Appendix D | Ti Elastic Database

```
$*****  
$ The definition of the pure elements, vacancy and species  
$-----  
TEMPERATURE_LIMIT 0 6000.00 !  
ELEMENT /- ELECTRON_GAS 0.0000E+00 0.0000E+00 0.0000E+00!  
ELEMENT VA VACUUM 0.0 0.0 0.0 !  
ELEMENT TI BCC_A2 !  
ELEMENT MO BCT_A5 !  
ELEMENT NB BCC_A2 !  
ELEMENT SN BCT_A5 !  
ELEMENT TA BCC_A2 !  
ELEMENT ZR BCT_A5 !
```

```
$*****  
$-----  
FUNCTION C11BCCTI 298.15 +93; 6000 N !  
FUNCTION C12BCCTI 298.15 +115; 6000 N !  
FUNCTION C44BCCTI 298.15 +41; 6000 N !  
FUNCTION C11BCCMO 298.15 +475; 6000 N !  
FUNCTION C12BCCMO 298.15 +164; 6000 N !  
FUNCTION C44BCCMO 298.15 +108; 6000 N !
```

FUNCTION C11BCCNB	298.15 +245;	6000 N !
FUNCTION C12BCCNB	298.15 +144;	6000 N !
FUNCTION C44BCCNB	298.15 +27;	6000 N !
FUNCTION C11BCCSN	298.15 +50;	6000 N !
FUNCTION C12BCCSN	298.15 +52;	6000 N !
FUNCTION C44BCCSN	298.15 +29;	6000 N !
FUNCTION C11BCCTA	298.15 +278;	6000 N !
FUNCTION C12BCCTA	298.15 +164;	6000 N !
FUNCTION C44BCCTA	298.15 +81;	6000 N !
FUNCTION C11BCCZR	298.15 +86;	6000 N !
FUNCTION C12BCCZR	298.15 +91;	6000 N !
FUNCTION C44BCCZR	298.15 +32;	6000 N !
FUNCTION UN_ASS	298.15 +0;	300 N !
\$		
FUNCTION UN_ASS	298.15 0;	300 N !
\$		
\$*****		
TYPE_DEFINITION % SEQ *		!
TYPE_DEFINITION G SEQ *		!
DEFINE_SYSTEM_DEFAULT SPECIE	5	!
DEFAULT_COMMAND DEF_SYS_ELEMENT VA		!
\$		
\$*****		
\$*****		
\$		
TYPE_DEFINITION & GES A_P_D BCC_A2 MAGNETIC	-1.0	4.00000E-01 !
PHASE BCC_A2 %& 2 1 3 !		
CONSTITUENT BCC_A2 :TI,MO,NB,SN,TA,ZR	:	VA :
PARAMETER C11(BCC_A2, TI:VA;0)		
298.15 +C11BCCTI;	6000 N !	
PARAMETER C11(BCC_A2, MO:VA;0)		
298.15 +C11BCCMO;	6000 N !	

PARAMETER C11(BCC_A2,NB:VA;0)
298.15 +C11BCCNB; 6000 N !
PARAMETER C11(BCC_A2,SN:VA;0)
298.15 +C11BCCSN; 6000 N !
PARAMETER C11(BCC_A2,TA:VA;0)
298.15 +C11BCCTA; 6000 N !
PARAMETER C11(BCC_A2,ZR:VA;0)
298.15 +C11BCCZR; 6000 N !
PARAMETER C11(BCC_A2,TI,MO:VA;0)
298.15 -22.16; 6000 N !
PARAMETER C11(BCC_A2,TI,NB:VA;0)
298.15 +40.46; 6000 N !
PARAMETER C11(BCC_A2,TI,SN:VA;0)
298.15 +119.46; 6000 N !
PARAMETER C11(BCC_A2,TI,TA:VA;0)
298.15 +83.65; 6000 N !
PARAMETER C11(BCC_A2,TI,TA:VA;1)
298.15 -67.76; 6000 N !
PARAMETER C11(BCC_A2,TI,ZR:VA;0)
298.15 +246.97; 6000 N !
PARAMETER C11(BCC_A2,TI,ZR:VA;1)
298.15 -135.95; 6000 N !
PARAMETER C11(BCC_A2,TI,MO,NB:VA;0)
298.15 -29.97; 6000 N !
PARAMETER C11(BCC_A2,TI,MO,SN:VA;0)
298.15 -83.85; 6000 N !
PARAMETER C11(BCC_A2,TI,MO,TA:VA;0)
298.15 -106.53; 6000 N !
PARAMETER C11(BCC_A2,TI,MO,ZR:VA;0)
298.15 -245.27; 6000 N !
PARAMETER C11(BCC_A2,TI,NB,SN:VA;0)
298.15 -41.52; 6000 N !
PARAMETER C11(BCC_A2,TI,NB,TA:VA;0)

298.15 -93.77; 6000 N !
PARAMETER C11(BCC_A2, TI, NB, ZR:VA;0)
298.15 -220.35; 6000 N !
PARAMETER C11(BCC_A2, TI, SN, TA:VA;0)
298.15 -95.39; 6000 N !
PARAMETER C11(BCC_A2, TI, SN, ZR:VA;0)
298.15 -155.34; 6000 N !
PARAMETER C11(BCC_A2, TI, TA, ZR:VA;0)
298.15 -149.67; 6000 N !
\$—————
PARAMETER C12(BCC_A2, TI:VA;0)
298.15 +C12BCCTI; 6000 N !
PARAMETER C12(BCC_A2, MO:VA;0)
298.15 +C12BCCMO; 6000 N !
PARAMETER C12(BCC_A2, NB:VA;0)
298.15 +C12BCCNB; 6000 N !
PARAMETER C12(BCC_A2, SN:VA;0)
298.15 +C12BCCSN; 6000 N !
PARAMETER C12(BCC_A2, TA:VA;0)
298.15 +C12BCCTA; 6000 N !
PARAMETER C12(BCC_A2, ZR:VA;0)
298.15 +C12BCCZR; 6000 N !
PARAMETER C12(BCC_A2, TI, MO:VA;0)
298.15 -36.40; 6000 N !
PARAMETER C12(BCC_A2, TI, NB:VA;0)
298.15 -32.39; 6000 N !
PARAMETER C12(BCC_A2, TI, SN:VA;0)
298.15 +15.90; 6000 N !
PARAMETER C12(BCC_A2, TI, SN:VA;1)
298.15 -146.80; 6000 N !
PARAMETER C12(BCC_A2, TI, TA:VA;0)
298.15 +38.05; 6000 N !
PARAMETER C12(BCC_A2, TI, ZR:VA;0)

298.15 -110.53; 6000 N !
PARAMETER C12(BCC_A2, TI, ZR:VA;1)
298.15 +78.00; 6000 N !
PARAMETER C12(BCC_A2, TI, MO, NB:VA;0)
298.15 +13.97; 6000 N !
PARAMETER C12(BCC_A2, TI, MO, SN:VA;0)
298.15 +31.80; 6000 N !
PARAMETER C12(BCC_A2, TI, MO, TA:VA;0)
298.15 -12.35; 6000 N !
PARAMETER C12(BCC_A2, TI, MO, ZR:VA;0)
298.15 +50.43; 6000 N !
PARAMETER C12(BCC_A2, TI, NB, SN:VA;0)
298.15 +25.52; 6000 N !
PARAMETER C12(BCC_A2, TI, NB, TA:VA;0)
298.15 -15.80; 6000 N !
PARAMETER C12(BCC_A2, TI, NB, ZR:VA;0)
298.15 +72.10; 6000 N !
PARAMETER C12(BCC_A2, TI, SN, TA:VA;0)
298.15 -10.94; 6000 N !
PARAMETER C12(BCC_A2, TI, SN, ZR:VA;0)
298.15 +68.86; 6000 N !
PARAMETER C12(BCC_A2, TI, TA, ZR:VA;0)
298.15 -8.91; 6000 N !
\$

PARAMETER C44(BCC_A2, TI:VA;0)
298.15 +C44BCCTI; 6000 N !
PARAMETER C44(BCC_A2, MO:VA;0)
298.15 +C44BCCMO; 6000 N !
PARAMETER C44(BCC_A2, NB:VA;0)
298.15 +C44BCCNB; 6000 N !
PARAMETER C44(BCC_A2, SN:VA;0)
298.15 +C44BCCSN; 6000 N !
PARAMETER C44(BCC_A2, TA:VA;0)

298.15 +C44BCCTA; 6000 N !
PARAMETER C44(BCC_A2,ZR:VA;0)
298.15 +C44BCCZR; 6000 N !
PARAMETER C44(BCC_A2,TI,MO:VA;0)
298.15 -142.90; 6000 N !
PARAMETER C44(BCC_A2,TI,NB:VA;0)
298.15 -41.54; 6000 N !
PARAMETER C44(BCC_A2,TI,NB:VA;1)
298.15 -41.95; 6000 N !
PARAMETER C44(BCC_A2,TI,SN:VA;0)
298.15 +59.75; 6000 N !
PARAMETER C44(BCC_A2,TI,SN:VA;1)
298.15 -94.38; 6000 N !
PARAMETER C44(BCC_A2,TI,TA:VA;0)
298.15 -51.96; 6000 N !
PARAMETER C44(BCC_A2,TI,ZR:VA;0)
298.15 +70.06; 6000 N !
PARAMETER C44(BCC_A2,TI,MO,NB:VA;0)
298.15 +9.72; 6000 N !
PARAMETER C44(BCC_A2,TI,MO,SN:VA;0)
298.15 +74.73; 6000 N !
PARAMETER C44(BCC_A2,TI,MO,TA:VA;0)
298.15 +5.27; 6000 N !
PARAMETER C44(BCC_A2,TI,MO,ZR:VA;0)
298.15 -44.96; 6000 N !
PARAMETER C44(BCC_A2,TI,NB,SN:VA;0)
298.15 +67.85; 6000 N !
PARAMETER C44(BCC_A2,TI,NB,TA:VA;0)
298.15 +4.25; 6000 N !
PARAMETER C44(BCC_A2,TI,NB,ZR:VA;0)
298.15 -55.29; 6000 N !
PARAMETER C44(BCC_A2,TI,SN,TA:VA;0)
298.15 +67.85; 6000 N !

```
PARAMETER C44(BCC_A2, TI, SN, ZR:VA;0)
298.15 +3.85; 6000 N !
PARAMETER C44(BCC_A2, TI, TA, ZR:VA;0)
298.15 -23.70; 6000 N !
$*****
*****LIST_OF_REFERENCES
NUMBER SOURCE
!
```

Appendix E | Pycalphad script

This code is used in pycalphad to plot the elastic moduli and elastic properites as a function of composition. A tdb file must be loaded into the script. In the present work the tdb file in Appendix D is used.

```
import matplotlib
from matplotlib.axes import Axes
from matplotlib.patches import Polygon
from matplotlib.path import Path
from matplotlib.ticker import NullLocator, Formatter, FixedLocator
from matplotlib.transforms import Affine2D, BboxTransformTo, IdentityTransform
from matplotlib.projections import register_projection
import matplotlib.spines as mspines
import matplotlib.axis as maxis
import matplotlib.pyplot as plt

import numpy as np

class TriangularAxes(Axes):
    """
    A custom class for triangular projections.
    """

    name = 'triangular'

    def __init__(self, *args, **kwargs):
        Axes.__init__(self, *args, **kwargs)
        self.set_aspect(1, adjustable='box', anchor='SW')
        self.cla()
```

```

def __init__(self):
    self.xaxis = maxis.XAxis(self)
    self.yaxis = maxis.YAxis(self)
    self._update_transScale()

def cla(self):
    """
    Override to set up some reasonable defaults.
    """
    # Don't forget to call the base class
    Axes.cla(self)

    x_min = 0
    y_min = 0
    x_max = 1
    y_max = 1
    x_spacing = 0.1
    y_spacing = 0.1
    self.xaxis.set_minor_locator(NullLocator())
    self.yaxis.set_minor_locator(NullLocator())
    self.xaxis.set_ticks_position('bottom')
    self.yaxis.set_ticks_position('left')
    Axes.set_xlim(self, x_min, x_max)
    Axes.set_ylim(self, y_min, y_max)
    self.xaxis.set_ticks(np.arange(x_min, x_max+x_spacing, x_spacing))
    self.yaxis.set_ticks(np.arange(y_min, y_max+y_spacing, y_spacing))

def __set__lim_and__transforms(self):
    """
    This is called once when the plot is created to set up all the
    transforms for the data, text and grids.
    """
    # There are three important coordinate spaces going on here:
    #
    # 1. Data space: The space of the data itself
    #
    # 2. Axes space: The unit rectangle (0, 0) to (1, 1)
    # covering the entire plot area.
    #
    # 3. Display space: The coordinates of the resulting image,
    # often in pixels or dpi/inch.

```

```

# This function makes heavy use of the Transform classes in
# ``lib/matplotlib/transforms.py``. For more information, see
# the inline documentation there.

# The goal of the first two transformations is to get from the
# data space (in this case longitude and latitude) to axes
# space. It is separated into a non-affine and affine part so
# that the non-affine part does not have to be recomputed when
# a simple affine change to the figure has been made (such as
# resizing the window or changing the dpi).

# 1) The core transformation from data space into
# rectilinear space defined in the HammerTransform class.
self.transProjection = IdentityTransform()
# 2) The above has an output range that is not in the unit
# rectangle, so scale and translate it so it fits correctly
# within the axes. The peculiar calculations of xscale and
#yscale are specific to a Aitoff-Hammer projection, so don't
# worry about them too much.
self.transAffine = Affine2D.from_values(
    1., 0, 0.5, np.sqrt(3)/2., 0, 0)
self.transAffinedep = Affine2D.from_values(
    1., 0, -0.5, np.sqrt(3)/2., 0, 0)
#self.transAffine = IdentityTransform()

# 3) This is the transformation from axes space to display
# space.
self.transAxes = BboxTransformTo(self.bbox)

# Now put these 3 transforms together -- from data all the way
# to display coordinates. Using the '+' operator, these
# transforms will be applied "in order". The transforms are
# automatically simplified, if possible, by the underlying
# transformation framework.
self.transData = \
    self.transProjection + \
    self.transAffine + \
    self.transAxes

# The main data transformation is set up. Now deal with

```

```

# gridlines and tick labels.

# Longitude gridlines and ticklabels. The input to these
# transforms are in display space in x and axes space in y.
# Therefore, the input values will be in range (-xmin, 0),
# (xmax, 1). The goal of these transforms is to go from that
# space to display space. The tick labels will be offset 4
# pixels from the equator.

self._xaxis._pretransform = IdentityTransform()
self._xaxis._transform = \
    self._xaxis._pretransform + \
    self.transData
self._xaxis._text1._transform = \
    Affine2D().scale(1.0, 0.0) + \
    self.transData + \
    Affine2D().translate(0.0, -20.0)
self._xaxis._text2._transform = \
    Affine2D().scale(1.0, 0.0) + \
    self.transData + \
    Affine2D().translate(0.0, -4.0)

# Now set up the transforms for the latitude ticks. The input to
# these transforms are in axes space in x and display space in
# y. Therefore, the input values will be in range (0, -ymin),
# (1, ymax). The goal of these transforms is to go from that
# space to display space. The tick labels will be offset 4
# pixels from the edge of the axes ellipse.

self._yaxis._transform = self.transData
yaxis_text_base = \
    self.transProjection + \
    (self.transAffine + \
    self.transAxes)
self._yaxis._text1._transform = \
    yaxis_text_base + \
    Affine2D().translate(-8.0, 0.0)
self._yaxis._text2._transform = \
    yaxis_text_base + \
    Affine2D().translate(8.0, 0.0)

```

```

def get_xaxis_transform(self, which='grid'):
    assert which in ['tick1', 'tick2', 'grid']
    return self._xaxis_transform

def get_xaxis_text1_transform(self, pad):
    return self._xaxis_text1_transform, 'bottom', 'center'

def get_xaxis_text2_transform(self, pad):
    return self._xaxis_text2_transform, 'top', 'center'

def get_yaxis_transform(self, which='grid'):
    assert which in ['tick1', 'tick2', 'grid']
    return self._yaxis_transform

def get_yaxis_text1_transform(self, pad):
    return self._yaxis_text1_transform, 'center', 'right'

def get_yaxis_text2_transform(self, pad):
    return self._yaxis_text2_transform, 'center', 'left'

def _gen_axes_spines(self):
    dep_spine = mspines.Spine.linear_spine(self,
                                             'right')
    # Fix dependent axis to be transformed the correct way
    dep_spine.set_transform(self.transAffinedep + self.transAxes)
    return {'left': mspines.Spine.linear_spine(self,
                                                'left'),
            'bottom': mspines.Spine.linear_spine(self,
                                                 'bottom'),
            'right': dep_spine}

def _gen_axes_patch(self):
    """
    Override this method to define the shape that is used for the
    background of the plot. It should be a subclass of Patch.
    Any data and gridlines will be clipped to this shape.
    """
    return Polygon([[0, 0], [0.5, np.sqrt(3)/2], [1, 0]], closed=True)

# Interactive panning and zooming is not supported with this projection,

```

```

# so we override all of the following methods to disable it.
def can_zoom(self):
    """
    Return True if this axes support the zoom box
    """
    return False

def start_pan(self, x, y, button):
    pass

def end_pan(self):
    pass

def drag_pan(self, button, key, x, y):
    pass

# Now register the projection with matplotlib so the user can select
# it.
register_projection(TriangularAxes)

import pycalphad.io.tdb_keywords
pycalphad.io.tdb_keywords.TDB_PARAM_TYPES.extend\
([ 'EM', 'BULK', 'SHEAR', 'C11', 'C12', 'C44' ])
from pycalphad import Database, Model, equilibrium, calculate
import numpy as np
import pycalphad.variables as v
import sympy
from tinydb import where

class ElasticModel(Model):
    def build_phase(self, dbe):
        phase = dbe.phases[self.phase_name]
        param_search = dbe.search
        # EM, BULK, SHEAR, C11, C12, C44
        for prop in [ 'EM', 'BULK', 'SHEAR', 'C11', 'C12', 'C44' ]:
            prop_param_query = (
                (where('phase_name') == phase.name) & \
                (where('parameter_type') == prop) & \
                (where('constituent_array').test(self._array_validity)))

```

```

)
prop_val = self.redlich_kister_sum \
(phase, param_search, prop_param_query).subs(dbe.symbols)
setattr(self, prop, prop_val)

dbf = Database('ElasticTi.tdb')
mod = ElasticModel(dbf, ['TI', 'SN', 'ZR', 'VA'], 'BCC_A2')
symbols = dict([(sympy.Symbol(s), val) for s, val in dbf.symbols.items()])
mod.C11 = mod.C11.xreplace(symbols)
mod.C12 = mod.C12.xreplace(symbols)
mod.C44 = mod.C44.xreplace(symbols)
x1 = np.linspace(0, 1, num=100)
x2 = np.linspace(0, 1, num=100)
mesh = np.meshgrid(x1, x2)
X = mesh[0]
Y = mesh[1]
mesh_arr = np.array(mesh)
mesh_arr = np.moveaxis(mesh_arr, 0, 2)
dep_col = 1 - np.sum(mesh_arr, axis=-1, keepdims=True)
mesh_arr = np.concatenate((mesh_arr, dep_col), axis=-1)
mesh_arr = np.concatenate((mesh_arr, np.ones(mesh_arr.shape[:-1] + (1,))), axis=-1)
orig_shape = tuple(mesh_arr.shape[:-1])
mesh_arr = mesh_arr.reshape(-1, mesh_arr.shape[-1])
mesh_arr[np.any(mesh_arr < 0, axis=-1), :] = np.nan
res_c11 = calculate(dbf, ['TI', 'SN', 'TA', 'VA'], 'BCC_A2', T=300, P=101325,
    model=mod, output='C11', points=mesh_arr)
res_c11 = res_c11.C11.values.reshape(orig_shape)
res_c12 = calculate(dbf, ['TI', 'SN', 'TA', 'VA'], 'BCC_A2', T=300, P=101325,
    model=mod, output='C12', points=mesh_arr)
res_c12 = res_c12.C12.values.reshape(orig_shape)
res_c44 = calculate(dbf, ['TI', 'SN', 'TA', 'VA'], 'BCC_A2', T=300, P=101325,
    model=mod, output='C44', points=mesh_arr)
res_c44 = res_c44.C44.values.reshape(orig_shape)

```

```

import numpy as np
def compute_moduli(c11, c12, c44):
    """Consume elastic stiffness constants and, under symmetry assumptions, compute
    bulk modulus, shear modulus, and Young's modulus.

```

Parameters

c11: float64 array-like
c12: float64 array-like
c44: float64 array-like

Returns

```

B, G, Y : tuple of float64 array-likes """
# Ported from a matlab code
c11 = np.array(c11)
c12 = np.array(c12)
c44 = np.array(c44)
cij = np.zeros(c11.shape + (6,6))
cij [..., 0, 0] = cij [..., 1, 1] = cij [..., 2, 2] = c11
cij [..., 0, 1] = cij [..., 1, 0] = cij [..., 0, 2] = \
cij [..., 2, 0] = cij [..., 1, 2] = cij [..., 2, 1] = c12
cij [..., 3, 3] = cij [..., 4, 4] = cij [..., 5, 5] = c44
sij = np.linalg.inv(cij)
A_c = (cij [..., 0, 0] + cij [..., 1, 1] + cij [..., 2, 2]) / 3.
B_c = (cij [..., 0, 1] + cij [..., 0, 2] + cij [..., 1, 2]) / 3.
C_c = (cij [..., 3, 3] + cij [..., 4, 4] + cij [..., 5, 5]) / 3.
A_s = (sij [..., 0, 0] + sij [..., 1, 1] + sij [..., 2, 2]) / 3.
B_s = (sij [..., 0, 1] + sij [..., 0, 2] + sij [..., 1, 2]) / 3.
C_s = (sij [..., 3, 3] + sij [..., 4, 4] + sij [..., 5, 5]) / 3.
Bv = (A_c + 2*B_c) / 3.
Gv = (A_c - B_c + 3*C_c) / 5.
Br = 1. / (3*A_s + 6*B_s)
Gr = 5. / (4*A_s - 4*B_s + 3*C_s)
Bvrh = (Br + Bv) / 2.
Gvrh = (Gr + Gv) / 2.
Yvrh = (9*Bvrh*Gvrh) / (Gvrh + 3*Bvrh)
return Bvrh, Gvrh, Yvrh

```

bulk_modulus, shear_modulus, young_modulus = \

```

compute_moduli(res_c11, res_c12, res_c44)

%matplotlib inline
import matplotlib.pyplot as plt

fig = plt.figure(figsize=(12,12))
ax = fig.gca(projection='triangular')
CS = ax.contour(X, Y, bulk_modulus, linewidths=4, \
levels=list(range(100, 300, 10)), cmap='cool')
ax.clabel(CS, inline=1, fontsize=13, fmt='%1.0f')
#PCM=ax.get_children()[0] #get the mappable,
#the 1st and the 2nd are the x and y axes
#plt.colorbar(PCM, ax=ax)
ax.set_xlabel('x(Mo)', fontsize=18)
ax.set_ylabel('x(Nb)', fontsize=18, rotation=60, labelpad=-180)
ax.tick_params(axis='both', which='major', labelsize=18)
ax.tick_params(axis='both', which='minor', labelsize=18)
ax.set_title('Bulk modulus')
#fig.savefig('TiMoNb-Bulk.pdf')

%matplotlib inline
import matplotlib.pyplot as plt

fig = plt.figure(figsize=(12,12))
ax = fig.gca(projection='triangular')
CS = ax.contour(X, Y, shear_modulus, linewidths=4, \
levels=list(range(0, 150, 5)), cmap='cool')
ax.clabel(CS, inline=1, fontsize=13, fmt='%1.0f')
#PCM=ax.get_children()[0] #get the mappable,
#the 1st and the 2nd are the x and y axes
#plt.colorbar(PCM, ax=ax)
ax.set_xlabel('x(Mo)', fontsize=18)
ax.set_ylabel('x(Nb)', fontsize=18, rotation=60, labelpad=-180)

```

```

ax.tick_params(axis='both', which='major', labelsize=18)
ax.tick_params(axis='both', which='minor', labelsize=18)
ax.set_title('Shear_modulus')
#fig.savefig('TiMoNb-Shear.pdf')

%matplotlib inline
import matplotlib.pyplot as plt

fig = plt.figure(figsize=(12,12))
ax = fig.gca(projection='triangular')
CS = ax.contour(X, Y, young_modulus, linewidths=4, \
levels=list(range(0, 350, 10)), cmap='cool')
ax.clabel(CS, inline=1, fontsize=13, fmt='%1.0f')
#PCM=ax.get_children()[0] #get the mappable,
#the 1st and the 2nd are the x and y axes
#plt.colorbar(PCM, ax=ax)
ax.set_xlabel('x(Mo)', fontsize=18)
ax.set_ylabel('x(Nb)', fontsize=18, rotation=60, labelpad=-180)
ax.tick_params(axis='both', which='major', labelsize=18)
ax.tick_params(axis='both', which='minor', labelsize=18)
ax.set_title('Young\''s_modulus')
#fig.savefig('TiMoNb-Young.pdf')

```

Appendix F |

Ti-Nb Experimental Elastic Data

Table F.1: The experimentally determined E values for the Ti-Nb system reviewed and averaged for chapter 7 are listed here [6–9].

x(Nb)	x(Ti)	E (GPa)	Reference
0.00	1.00	117.16	[6]
0	1.00	132	[8]
0.00	1.00	115.77	[7]
0.00	1.00	108.30	[9]
0.01	0.99	112.30	[6]
0.01	0.99	112.74	[7]
0.02	0.98	109.05	[6]
0.02	0.98	107.61	[7]
0.05	0.95	79.46	[6]
0.05	0.95	78.69	[7]
0.05	0.95	80.27	[6]
0.08	0.92	66.49	[6]
0.08	0.92	66.33	[7]
0.09	0.91	66.89	[6]
0.09	0.91	70.58	[9]
0.10	0.90	66.49	[6]
0.10	0.90	115	[8]
0.10	0.90	91	[8]
0.10	0.90	66.09	[7]

Table F.1: The experimentally determined E values for the Ti-Nb system reviewed and averaged for chapter 7 are listed here [6–9].

x(Nb)	x(Ti)	E (GPa)	Reference
0.11	0.89	77.99	[7]
0.11	0.89	79.46	[6]
0.18	0.82	92.43	[6]
0.18	0.82	93.62	[7]
0.19	0.81	65.27	[6]
0.19	0.81	63.24	[6]
0.20	0.80	75	[8]
0.20	0.80	89	[8]
0.20	0.80	68.85	[9]
0.22	0.78	71.46	[7]
0.22	0.78	72.63	[9]
0.22	0.78	68.62	[9]
0.23	0.77	72.16	[6]
0.23	0.77	103.64	[7]
0.23	0.77	60.34	[9]
0.23	0.77	67.24	[9]
0.24	0.76	65.16	[9]
0.24	0.76	57.07	[9]
0.25	0.75	71.76	[6]
0.25	0.75	74	[8]
0.25	0.75	78	[8]
0.25	0.75	66.33	[7]
0.26	0.74	61.85	[9]
0.26	0.74	73.09	[9]
0.26	0.74	82.19	[7]
0.26	0.74	60.50	[7]
0.26	0.74	67.70	[6]
0.26	0.74	54.31	[9]
0.27	0.73	56.46	[9]
0.27	0.73	52.76	[9]

Table F.1: The experimentally determined E values for the Ti-Nb system reviewed and averaged for chapter 7 are listed here [6–9].

x(Nb)	x(Ti)	E (GPa)	Reference
0.29	0.71	62.83	[7]
0.29	0.71	61.43	[7]
0.30	0.70	67.70	[6]
0.30	0.70	62.69	[9]
0.30	0.70	72	[8]
0.30	0.70	69	[8]
0.30	0.70	69.31	[9]
0.30	0.70	67.96	[7]
0.34	0.66	76.21	[9]
0.34	0.66	86.02	[9]
0.34	0.66	74.26	[7]
0.34	0.66	75.84	[9]
0.34	0.66	75.00	[6]
0.36	0.64	73.78	[6]
0.39	0.61	76.62	[6]
0.43	0.57	84.0	[7]

Bibliography

- [1] WU, C., Y. XIN, X. WANG, and J. LIN (2010) “Effects of Ta content on the phase stability and elastic properties of β Ti \AA Sta alloys from first-principles calculations,” *Solid State Sciences*, **12**(12), pp. 2120–2124.
- [2] IKEHATA, H., N. NAGASAKO, T. FURUTA, A. FUKUMOTO, K. MIWA, and T. SAITO (2004) “First-principles calculations for development of low elastic modulus Ti alloys,” *Physical Review B*, **70**(17), p. 174113.
- [3] ZHOU, Y. L., M. NIINOMI, and T. AKAHORI (2004) “Effects of Ta content on Young’s modulus and tensile properties of binary Ti \AA Sta alloys for biomedical applications,” *Materials Science and Engineering: A*, **371**(1-2), pp. 283–290.
- [4] ZHOU, Y.-L. and M. NIINOMI (2009) “Ti \AA 25Ta alloy with the best mechanical compatibility in Ti \AA Sta alloys for biomedical applications,” *Materials Science and Engineering: C*, **29**(3), pp. 1061–1065.
- [5] FEDOTOV, S., T. CHELIDZE, Y. KOVNERISTYY, and V. SANADZE (1985) “Phase structure, critical points MS and AS of martensitic transformations and elastic properties of metastable alloys of the Ti-Ta system,” *Phys. Met. Metall.*, **60**(3), pp. 139–143.
- [6] TIMOSHEVSKII, A., S. YABLONOVSKII, and O. IVASHISHIN (2011) “First-principles calculations atomic structure and elastic properties of Ti-Nb alloys,” *arXiv preprint arXiv:1111.7182*.
- [7] OZAKI, T., H. MATSUMOTO, S. WATANABE, and S. HANADA (2004) “Beta Ti Alloys with Low Young’s Modulus,” *MATERIALS TRANSACTIONS*, **45**(8), pp. 2776–2779.
- [8] FRIÁK, M., W. COUNTS, D. MA, B. SANDER, D. HOLEC, D. RAABE, and J. NEUGEBAUER (2012) “Theory-guided materials design of multi-phase Ti-Nb alloys with bone-matching elastic properties,” *Materials*, **5**(10), pp. 1853–1872.

- [9] KARRE, R., M. NIRANJAN, and S. DEY (2015) “First principles theoretical investigations of low Young’s modulus beta Ti_xNb and Ti_xNb_{1-x}Zr alloys compositions for biomedical applications,” *Materials Science and Engineering: C*, **50**, pp. 52–58.
URL <http://www.sciencedirect.com/science/article/pii/S0928493115000715>
- [10] MATSUMOTO, H., S. WATANABE, N. MASAHASHI, and S. HANADA (2006) “Composition dependence of Young’s modulus in Ti-V, Ti-Nb, and Ti-V-Sn alloys,” *Metallurgical and Materials Transactions A*, **37**(11), pp. 3239–3249.
- [11] XIONG, W., Y. DU, Y. LIU, B. HUANG, H. XU, H. CHEN, and Z. PAN (2004) “Thermodynamic assessment of the Mo-Nb-Ta system,” *Calphad-Computer Coupling of Phase Diagrams and Thermochemistry*, **28**(2), pp. 133–140.
- [12] PEREZ, R. and B. SUNDMAN (2003) “Thermodynamic assessment of the Mo-Zr binary phase diagram,” *Calphad-Computer Coupling of Phase Diagrams and Thermochemistry*, **27**(3), pp. 253–262.
- [13] GUILLERMET, A. (1991) “Thermodynamic analysis of the stable phases in the Zr-Nb system and calculation of the phase-diagram,” *Zeitschrift Fur Metallkunde*, **82**(6), pp. 478–487.
- [14] ABRIATA, J. P. and J. C. BOLCICH (1982) “The Nb-Zr (Niobium-Zirconium) system,” *Bulletin of alloy phase diagrams*, **3**(1), pp. 34–44.
- [15] GUILLERMET, A. (1995) “Phase-diagram and thermochemical properties of the Zr-Ta system - an assessment based on Gibbs energy modeling,” *Journal of Alloys and Compounds*, **226**(1-2), pp. 174–184.
- [16] ANSARA, I., A. DINSDALE, and M. RAND (1998) *COST 507: thermochemical database for light metal alloys*, vol. 2, European Communities, Brussels and Luxembourg.
- [17] MURRAY, J. (1981) “The Mo-Ti (Molybdenum-Titanium) system,” *Bulletin of Alloy Phase Diagrams*, **2**(2), pp. 185–192.
- [18] UESUGI, T., S. MIYAMAE, and K. HIGASHI (2013) “Enthalpies of Solution in Ti_xX (X= Mo, Nb, V and W) Alloys from First-Principles Calculations,” *Materials Transactions*, **54**(4), pp. 484–492.
- [19] ZHANG, Y., H. LIU, and Z. JIN (2001) “Thermodynamic assessment of the Nb-Ti system,” *Calphad-Computer Coupling of Phase Diagrams and Thermochemistry*, **25**(2), pp. 305–317.

- [20] KUMAR, K., P. WOLLANTS, and L. DELAEY (1994) “Thermodynamic calculation of Nb-Ti-V phase diagram,” *CALPHAD*, **18**(1), pp. 71–79.
- [21] ——— (1994) “Thermodynamic assessment of the Ti-Zr system and calculation of the Nb-Ti-Zr phase-diagram,” *Journal of Alloys and Compounds*, **206**(1), pp. 121–127.
- [22] MURRAY, J. L. (1987) “Phase diagrams of binary titanium alloys,” *ASM International, 1987*, p. 354.
- [23] NIKITIN, P. and V. MIKHEYEV (1971) “Examination of titanium corner of Ti-Ta-Mo equilibrium diagram,” *Russian Metallurgy-Metally-USSR*, (1), pp. 144–147.
- [24] KAR, S. and D. LIPKIN (2008) “A CALPHAD-based phase equilibrium model of Mo-Ti-Zr-C,” in *TMS 2008 Annual Meeting Supplemental Proceedings, Vol 2: Materials Characterization, Computation and Modeling*, Minerals, Metals & Materials Soc, Warrendale, pp. 237–243.
- [25] PROKOSHKIN, D. A. and M. I. ZAKHAROVA (1967) “Phase equilibrium in the molybdenum-titanium-zirconium system(Ternary phase diagram of Mo-Ti-Zr system from eleven isothermal cross sections),” in *AKADEMIIA NAUK SSSR, DOKLADY*, vol. 172, pp. 1382–1384.
- [26] NA, L. and W. WARNE (2001) “Estimation of the Nb-Ti-Ta phase diagram,” *Ieee Transactions on Applied Superconductivity*, **11**(1), pp. 3800–3803.
- [27] TOKUNAGA, T., S. MATSUMOTO, H. OHTANI, and M. HASEBE (2007) “Thermodynamic calculation of phase equilibria in the Nb-Ni-Ti-Zr quaternary system,” *Materials transactions*, **48**(2), pp. 89–96.
- [28] LIN, L., L. DELAEY, O. VANDERBIEST, and P. WOLLANTS (1996) “Calculation of isothermal sections of three ternary Ti-Zr-X systems,” *Scripta Materialia*, **34**(9), pp. 1411–1416.
- [29] HOCH, M. and D. BUTRYMOW (1964) “System tantalum-titanium-zirconium-oxygen at 1500 degrees C,” *Transactions of the Metallurgical Society of AIME*, **230**(1), pp. 186–192.
- [30] TAIOLI, S., C. CAZORLA, M. J. GILLAN, and D. ALFÈ (2007) “Melting curve of tantalum from first principles,” *Physical Review B*, **75**(21), p. 214103.
- [31] OLIJNYK, H. (1992) “Pressure dependence of Raman phonons of metallic β -Sn,” *Physical Review B*, **46**(10).
- [32] DINSDALE, A. (1991) “SGTE Data for Pure Elements,” *CALPHAD*, **15**(4), pp. 317–425.

- [33] TOFFOLON, C., C. SERVANT, and B. SUNDMAN (1998) “Thermodynamic assessment of the Nb-Sn system,” *Journal of Phase Equilibria*, **19**(5), pp. 479–485.
- [34] ZHANG, W.-D., Y. LIU, H. WU, M. SONG, T.-Y. ZHANG, X.-D. LAN, and T.-H. YAO (2015) “Elastic modulus of phases in Ti_xMo alloys,” *Materials Characterization*, **106**, pp. 302–307.
- [35] BOYER, R., G. WELSCH, and E. COLLINGS (1994) “Materials Properties Handbook: Titanium Alloys,” *ASM International, Materials Park, OH*.
- [36] SUNG, B.-S., T.-E. PARK, and Y.-H. YUN (2015) “Microstructures and electrochemical behavior of Ti-Mo alloys for biomaterials,” *Advances in Materials Science and Engineering*, **2015**(Article ID 872730), pp. 1–7.
- [37] TANE, M., S. AKITA, T. NAKANO, K. HAGIHARA, Y. UMAKOSHI, M. NIINOMI, H. MORI, and H. NAKAJIMA (2010) “Low Young’s modulus of Ti_xNb_yTa_zZr alloys caused by softening in shear moduli c₄₄ and c₁₁ near lower limit of body-centered cubic phase stability,” *Acta Materialia*, **58**(20), pp. 6790–6798.
- [38] GEETHA, M., A. SINGH, R. ASOKAMANI, and A. GOGIA (2009) “Ti based biomaterials, the ultimate choice for orthopaedic implants – A review,” *Progress in Materials Science*, **54**(3), pp. 397–425.
- [39] MOHAMMED, M., Z. KHAN, and A. SIDDIQUEE (2014) “Beta titanium alloys: the lowest elastic modulus for biomedical applications: a review,” *International Journal of Chemical, Molecular, Nuclear, Materials and Metallurgical Engineering*, **8**(8), pp. 788–793.
- [40] NIINOMI, M., M. NAKAI, and J. HIEDA (2012) “Development of new metallic alloys for biomedical applications,” *Acta Biomaterialia*, **8**(11), pp. 3888–3903.
- [41] NOZOE, F., H. MATSUMOTO, T. K. JUNG, S. WATANABE, T. SABURI, and S. HANADA (2007) “Effect of low temperature aging on superelastic behavior in biocompatible beta TiNbSn Alloy,” *Materials transactions*, **48**(11), pp. 3007–3013.
- [42] OTIS, R. and Z.-K. LIU (2017) “pycalphad: CALPHAD-based computational thermodynamics in Python,” *Journal of Open Research Software*, **5**(1), pp. 1–11.
- [43] LONG, M. and H. RACK (1998) “Titanium alloys in total joint replacement materials science perspective,” *Biomaterials*, **19**(18), pp. 1621–1639.

- [44] KURTZ, S. (2007) “Projections of primary and revision hip and knee arthroplasty in the United States from 2005 to 2030,” *The Journal of Bone and Joint Surgery (American)*, **89**(4), pp. 780–785.
- [45] KRISHNA, B., S. BOSE, and A. BANDYOPADHYAY (2007) “Low stiffness porous Ti structures for load-bearing implants,” *Acta biomaterialia*, **3**(6), pp. 997–1006.
- [46] NIINOMI, M. (2003) “Recent research and development in titanium alloys for biomedical applications and healthcare goods,” *Science and Technology of Advanced Materials*, **4**(5), pp. 445–454.
- [47] ITO, A., Y. OKAZAKI, T. TATEISHI, and Y. ITO (1995) “In vitro biocompatibility, mechanical properties, and corrosion resistance of Ti-Zr-Nb-Ta-Pd and Ti-Sn-Nb-Ta-Pd alloys,” *Journal of Biomedical Materials Research*, **29**(7), pp. 893–899.
- [48] JAIN, A., S. ONG, G. HAUTIER, W. CHEN, W. RICHARDS, S. DACEK, S. CHOLIA, D. GUNTER, D. SKINNER, and G. CEDER (2013) “The Materials Project: A materials genome approach to accelerating materials innovation,” *Apl Materials*, **1**(1), p. 11002.
- [49] ANTOLIN, N., O. RESTREPO, and W. WINDL (2012) “Fast free-energy calculations for unstable high-temperature phases,” *Physical Review B*, **86**(5), p. 54119.
- [50] MEI, Z. Z. G. (2011) *First-principles Thermodynamics of Phase Transition: from Metal to Oxide*, Ph.D. thesis.
- [51] BRAILOVSKI, V., S. PROKOSHIN, M. GAUTHIER, K. INAEKYAN, S. DUBINSKIY, M. PETRZHIK, and M. FILONOV (2011) “Bulk and porous metastable beta Ti_xNb_yZr (Ta) alloys for biomedical applications,” *Materials Science and Engineering: C*, **31**(3), pp. 643–657.
- [52] TANE, M., S. AKITA, T. NAKANO, K. HAGIHARA, Y. UMAKOSHI, M. NIINOMI, and H. NAKAJIMA (2008) “Peculiar elastic behavior of Ti_xNb_yZr single crystals,” *Acta Materialia*, **56**(12), pp. 2856–2863.
- [53] KHACHATURYAN, A. (1985) “Theory of structural transformations in solids. 1983,” *Wiley, New York, Jacobs AE, Phys. Rev. B*, **31**, p. 5984.
- [54] SALJE, E. (1990) “Phase transitions in ferroelastic and co-elastic crystals,” *Ferroelectrics*, **104**(1), pp. 111–120.
- [55] HOHENBERG, P. and W. KOHN (1964) “Inhomogeneous Electron Gas,” *Physical Review*, **136**(3B), pp. B864–B871.
URL <http://link.aps.org/doi/10.1103/PhysRev.136.B864>

- [56] KOHN, W. and L. SHAM (1965) “Self-Consistent Equations Including Exchange and Correlation Effects,” *Phys. Rev.*, **140**, pp. 1133–1138.
- [57] PERDEW, J. and Y. WANG (1992) “Accurate and simple analytic representation of the electron-gas correlation energy,” *Physical Review B*, **45**(23), p. 13244.
- [58] PERDEW, J., K. BURKE, and M. ERNZERHOF (1996) “Generalized gradient approximation made simple,” *Physical Review Letters*, **77**(18), pp. 3865–3868.
- [59] CUPERLEY, D. M. and B. J. ALDER (1980) “Ground state of the electron gas by a stochastic method,” *Physical Review Letters*, **45**(7), p. 566.
- [60] SHANG, S., Y. WANG, D. KIM, and Z.-K. LIU (2010) “First-principles thermodynamics from phonon and Debye model: Application to Ni and Ni₃Al,” *Computational Materials Science*, **47**(4), pp. 1040–1048.
- [61] KRESSE, G. and J. FURTHMÜLLER (1996) “Efficiency of ab-initio total energy calculations for metals and semiconductors using a plane-wave basis set,” *Computational Materials Science*, **6**(1), pp. 15–50.
- [62] KRESSE, G. and D. JOUBERT (1999) “From ultrasoft pseudopotentials to the projector augmented-wave method,” *Physical Review B*, **59**(3), pp. 1758–1775.
- [63] WANG, A., S. SHANG, D. ZHAO, J. WANG, L. CHEN, Y. DU, Z.-K. LIU, T. XU, and S. WANG (2012) “Structural, phonon and thermodynamic properties of fcc-based metal nitrides from first-principles calculations,” *Calphad*, **37**, pp. 126–131.
- [64] MORUZZI, V. L., J. F. JANAK, and K. SCHWARZ (1988) “Calculated thermal properties of metals,” *Physical Review B*, **37**(2), pp. 790–799.
- [65] LIU, X. L., B. K. VANLEEUWEN, S. SHANG, Y. DU, and Z.-K. LIU (2015) “On the scaling factor in Debye–Grüneisen model: A case study of the Mg–Zn binary system,” *Computational Materials Science*, **98**, pp. 34–41.
- [66] WANG, Y., Z.-K. LIU, and L.-Q. CHEN (2004) “Thermodynamic properties of Al, Ni, NiAl, and Ni₃Al from first-principles calculations,” *Acta Materialia*, **52**(9), pp. 2665–2671.
- [67] SHANG, S., Y. WANG, and Z.-K. LIU (2007) “First-principles elastic constants of alpha- and theta-Al₂O₃,” *Applied Physics Letters*, **90**(10), pp. 101909–1–101909–3.
- [68] SIMMONS, G. and H. WANG (1971) *Single Crystal Elastic Constants and Calculated Aggregate Properties: A Handbook*, M.I.T. Press, Cambridge.

- [69] ZUO, Y. and Y. CHANG (1993) “Thermodynamic calculation of the Mg-Cu phase diagram,” *Zeit. Metall.*, **84**(10), pp. 662–667.
- [70] CHUNG, D. H. and W. R. BUSSSEM (1967) “The Voigt–Reuss–Hill approximation and elastic moduli of Polycrystalline MgO, CaF₂, β -ZnS, ZnSe, and CdTe,” *Journal of Applied Physics*, **38**(6), pp. 2535–2540.
- [71] BORN, M. and K. HUANG (1998) *Dynamical Theory of Crystal Lattices*, Oxford University Press.
- [72] NYE, J. (1985) *Physical Properties of Crystals: Their Representation by Tensors and Matrices*, Oxford University Press.
- [73] JIANG, C., C. WOLVERTON, J. SOFO, L.-Q. CHEN, and Z.-K. LIU (2004) “First-principles study of binary bcc alloys using special quasirandom structures,” *Physical Review B*, **69**(21), pp. 214202–1–214202–10.
- [74] JIANG, C. (2009) “First-principles study of ternary bcc alloys using special quasi-random structures,” *Acta Materialia*, **57**(16), pp. 4716–4726.
- [75] TOGO, A., F. OBA, and I. TANAKA (2008) “First-principles calculations of the ferroelastic transition between rutile-type and CaCl₂-type SiO₂ at high pressures,” *Physical Review B*, **78**(13), p. 134106.
- [76] LIU, Z. K. and Y. WANG (2016) *Computational Thermodynamics of Materials*, Cambridge University Press.
- [77] ANDERSSON, J.-O., T. HELANDER, L. HÖGLUND, P. SHI, and B. SUNDMAN (2002) “Thermo-Calc & DICTRA, computational tools for materials science,” *Calphad*, **26**(2), pp. 273–312.
- [78] REDLICH, O. and A. T. KISTER (1948) “Algebraic representation of thermodynamic properties and the classification of solutions,” *Industrial & Engineering Chemistry*, **40**(2), pp. 345–348.
- [79] ZACHERL, C., S. SHANG, A. SAENGDEEJING, and Z.-K. LIU (2012) “Phase stability and thermodynamic modeling of the Re–Ti system supplemented by first-principles calculations,” *Calphad*, **38**, pp. 71–80.
- [80] LIU, Z.-K. (2009) “First-principles calculations and CALPHAD modeling of thermodynamics,” *Journal of Phase Equilibria and Diffusion*, **30**(5), pp. 517–534.
- [81] LUKAS, H., S. FRIES, and B. SUNDMAN (2007) *Computational Thermodynamics: the CALPHAD Method*, vol. 131, Cambridge University Press, Cambridge.

- [82] LIU, Z.-K., H. ZHANG, S. GANESHAN, Y. WANG, and S. MATHAUDHU (2010) “Computational modeling of effects of alloying elements on elastic coefficients,” *Scripta Materialia*, **63**(7), pp. 686–691.
- [83] SAUNDERS, N. and A. MIODOWNIK (1998) *CALPHAD (Calculation of Phase Diagrams): A Comprehensive Guide: A Comprehensive Guide*, vol. 1, Elsevier.
- [84] YOUNG, R. and A. LARSON (1998) “Rietveld analysis of X-ray and neutron powder diffraction patterns,” *Atlanta (GA): School of*.
URL <http://debian.ccp14.ac.uk/ccp/web-mirrors/dbws/downloads/young/guide99.pdf>
- [85] TORAYA, H. (1986) “Whole-Powder-Pattern Fitting Without Reference to a Structural Model: Application to X-ray Powder Diffractometer Data,” *J. Appl. Cryst.*, **19**, pp. 440–447.
- [86] FULTZ, B., T. KELLEY, M. MCKERNIS, J. LIN, J. LEE, O. DELAIRE, M. KRESCH, and M. AIVAZIS (2009), “Experimental inelastic neutron scattering,” .
- [87] SQUIRES, G. L. (2012) *Introduction to the theory of thermal neutron scattering*, Cambridge university press.
- [88] MANLEY, M. E. (2001) *From elementary excitations to microstructures: The thermodynamics of metals and alloys across length scales*.
- [89] MANLEY, M. E., R. J. MCQUEENEY, B. FULTZ, R. OSBORN, G. H. KWEI, and P. D. BOGDANOFF (2002) “Vibrational and electronic entropy of β -cerium and γ -cerium measured by inelastic neutron scattering,” *Physical Review B*, **65**(14), p. 144111.
URL <http://link.aps.org/doi/10.1103/PhysRevB.65.144111>
- [90] BLÖCHL, P. (1994) “Projector augmented-wave method,” *Physical Review B*, **50**(24), p. 17953.
- [91] MONKHORST, H. and J. PACK (1976) “Special points for Brillouin-zone integrations,” *Physical Review B*, **13**(12), pp. 5188–5192.
- [92] PREDEL, B. (1997) “Mo-Ti (Molybdenum-Titanium) BT - Li-Mg ÅS Nd-Zr,” Springer Berlin Heidelberg, Berlin, Heidelberg, pp. 1–3.
- [93] HOFFMAN, J. R., E. RUDY, S. T. WINDISCH, and A. J. STOSICK (1967) “The constitution of binary molybdenum-carbon alloys(Binary molybdenum-carbon system investigated using X-ray, metallographic, thermoanalytical and melting-point techniques),” *AIME, TRANSACTIONS*, **239**, pp. 1247–1267.

- [94] ENGLISH, J. (1961) *Binary and Ternary Phase Diagrams of Columbium, Molybdenum, Tantalum, and Tungsten*, Tech. rep.
- [95] SCHMITZ-PRANGHE, N. and P. DUENNER (1968) “Gitterstruktur und thermische Ausdehnung der Uebergangsmetalle Scandium, Titan, Vanadin und Mangan,” *Zeitschrift fuer Metallkunde*, **59**, pp. 377–382.
- [96] “Materials Project,” .
URL <http://www.materialsproject.org>
- [97] WOLFRAM RESEARCH, I., “Matematica,” .
- [98] YI, C., S. JIANG, and C. NANXIAN (2009) “The effect of Mo atoms in ternary nitrides with eta-type structure,” *Solid State Communications*, **149**, pp. 121–125.
- [99] BOLEF, D. (1961) “Elastic constants of single crystals of the bcc transition elements V, Nb, and Ta,” *Journal of Applied Physics*, **32**(1), pp. 100–105.
- [100] NEUBURGER, M. C. (1936) “Praezisionsmessung der Gitterkonstante von sehr reinem Niob,” *Zeitschrift fuer Kristallographie, Kristallgeometrie, Kristallphysik, Kristallchemie (-144,1977)*, **93**, pp. 158–159.
- [101] ——— (1936) “Praezisionsmessung der Gitterkonstante von sehr reinem Tantal,” *Zeitschrift fuer Kristallographie, Kristallgeometrie, Kristallphysik, Kristallchemie (-144,1977)*, **93**, pp. 312–313.
- [102] TRECO, R. M. (1953) “Effect of small additions of oxygen on lattice constants and hardness of zirconium,” *Transactions of the American Institute of Mining, Metallurgical and Petroleum Engineers*, **197**, pp. 344–348.
- [103] BERGERHOFF, G., R. HUNDT, R. SIEVERS, and I. D. BROWN (1983) “The inorganic crystal structure data base,” *Journal of Chemical Information and Computer Sciences*, **23**(2), pp. 66–69.
- [104] KARLSRUHE, F. I. Z., “Inorganic Crystal Structure Database,” .
- [105] KURODA, D., M. NIINOMI, M. MORINAGA, Y. KATO, and T. YASHIRO (1998) “Design and mechanical properties of new β type titanium alloys for implant materials,” *Materials Science and Engineering: A*, **243**(1), pp. 244–249.
- [106] HE, G. and M. HAGIWARA (2004) “Ti-Cu-Ni (Fe, Cr, Co)-Sn-Ta (Nb) alloys with potential for biomedical applications,” *Materials Transactions*, **45**(4), pp. 1120–1123.

- [107] ——— (2006) “Ti alloy design strategy for biomedical applications,” *Materials Science and Engineering: C*, **26**(1), pp. 14–19.
- [108] OKAMOTO, H. (2003) “Sn-Ta (Tin-Tantalum),” *Journal of Phase Equilibria*, **24**(5), p. 484.
- [109] STUDNITZKY, T. and R. SCHMID-FETZER (2002) “Phase Formation and reaction Kinetics in M-Sn systems (M=Zr, Hf, Nb, Ta, Mo),” *Zeitschrift Fur Metallkunde*, **93**(9), pp. 894–903.
- [110] BASILE, F. (1971) “Cristallographic study and supraconductive properties of compounds V₃Sn and Ta₂Sn₃,” in *Annales de chimie*, vol. 6, pp. 241–244.
- [111] YUE, Q., Y. LIU, M. CHU, and J. SHEN (2009) “Thermodynamic modeling of the Sn–V binary system,” *Calphad*, **33**(3), pp. 539–544.
- [112] TOFFOLON, C., C. SERVANT, J. GACHON, and B. SUNDMAN (2002) “Re-assessment of the Nb-Sn system,” *Journal of Phase Equilibria*, **23**(2), pp. 134–139.
- [113] COURTNEY, T., G. PEARSALL, and J. WULFF (1965) “Effect of Processing History on the Superconducting Properties and Long-Range Order of Ta₃Sn,” *Journal of Applied Physics*, **36**(10), pp. 3256–3260.
- [114] PREDMORE, R. and R. ARSENAULT (1970) “Short range order of Ta-Mo B.C.C. alloys,” *Scripta Metallurgica*, **4**(3), pp. 213–217.
- [115] SHANG, S., A. SAENGDEEJING, Z. MEI, D. KIM, H. ZHANG, S. GANESHAN, Y. WANG, and Z.-K. LIU (2010) “First-principles calculations of pure elements: Equations of state and elastic stiffness constants,” *Computational Materials Science*, **48**(4), pp. 813–826.
- [116] ALLEN, W. and J. PEREPEZKO (1991) “Solidification of undercooled Sn-Sb peritectic alloys: Part I. Microstructural evolution,” *Metallurgical Transactions A*, **22**(3), pp. 753–764.
- [117] ARROYAVE, R. and Z.-K. LIU (2006) “Intermetallics in the Mg-Ca-Sn ternary system: Structural, vibrational, and thermodynamic properties from first principles,” *Physical Review B*, **74**(17), p. 174118.
- [118] CALVERT, L. and P. VILLARS (1991) “Pearson’s Handbook of Crystallographic Data for Intermetallic Phases,” *ASM, Materials Park, OH*.
- [119] PELTZER Y BLANCÁ, E. L., A. SVANE, N. E. CHRISTENSEN, C. O. RODRÍGUEZ, O. M. CAPPANNINI, and M. S. MORENO (1993) “Calculated static and dynamic properties of β -Sn and Sn-O compounds,” *Physical Review B*, **48**(21), pp. 15712–15718.

- [120] JOUAULT, F. and P. LECOCQ (1967) “Etude comparee des trois diagrammes V-Sn, Nb-Sn, Ta-Sn,” *Colloques Internationaux du Centre National de la Recherche Scientifique*, **157**, pp. 229–235.
- [121] GELLER, S., B. T. MATTHIAS, and R. GOLDSTEIN (1955) “Some new intermetallic compounds with the beta.-wolfram structure,” *Journal of the American Chemical Society*, **77**, pp. 1502–1504.
- [122] WANG, Y., S. CURTAROLO, C. JIANG, R. ARROYAVE, T. WANG, G. CEDER, L.-Q. CHEN, and Z.-K. LIU (2004) “Ab initio lattice stability in comparison with CALPHAD lattice stability,” *Calphad*, **28**(1), pp. 79–90.
- [123] ARROYAVE, R. and Z.-K. LIU (2006) “Thermodynamic modelling of the Zn–Zr system,” *Calphad*, **30**(1), pp. 1–13.
- [124] DICKINSON, J. and P. ARMSTRONG (1967) “Temperature dependence of the elastic constants of molybdenum,” *Journal of Applied Physics*, **38**(2), pp. 602–606.
- [125] KIM, H., Y. IKEHARA, J. KIM, H. HOSODA, and S. MIYAZAKI (2006) “Martensitic transformation, shape memory effect and superelasticity of Ti–Nb binary alloys,” *Acta Materialia*, **54**(9), pp. 2419–2429.
- [126] BUDAI, J. D., J. HONG, M. E. MANLEY, E. D. SPECHT, C. W. LI, J. Z. TISCHLER, D. L. ABERNATHY, A. H. SAID, B. M. LEU, L. A. BOATNER, R. J. MCQUEENEY, and O. DELAIRE (2014) “Metallization of vanadium dioxide driven by large phonon entropy,” *Nature*, **515**(7528), pp. 535–539.
URL <http://dx.doi.org/10.1038/nature13865> <http://www.nature.com/nature/journal/v515/n7528/abs/nature13865.html>{#}supplementary-information